

---

**Pacific Northwest  
National Laboratory**

Operated by Battelle for the  
U.S. Department of Energy

## **Development of a Microchannel *In Situ* Propellant Production System**

KP Brooks  
SD Rassat  
WE TeGrotenhuis

September 2005

Prepared for the National Aeronautics and Space Administration  
Lyndon B. Johnson Space Center

Prepared for the U.S. Department of Energy  
under Contract DE-AC05-76RL01830



**DISCLAIMER**

This report was prepared as an account of work sponsored by an agency of the United States Government. Neither the United States Government nor any agency thereof, nor Battelle Memorial Institute, nor any of their employees, makes **any warranty, express or implied, or assumes any legal liability or responsibility for the accuracy, completeness, or usefulness of any information, apparatus, product, or process disclosed, or represents that its use would not infringe privately owned rights.** Reference herein to any specific commercial product, process, or service by trade name, trademark, manufacturer, or otherwise does not necessarily constitute or imply its endorsement, recommendation, or favoring by the United States Government or any agency thereof, or Battelle Memorial Institute. The views and opinions of authors expressed herein do not necessarily state or reflect those of the United States Government or any agency thereof.

PACIFIC NORTHWEST NATIONAL LABORATORY  
*operated by*  
BATTELLE  
*for the*  
UNITED STATES DEPARTMENT OF ENERGY  
*under Contract DE-AC05-76RL01830*

**Printed in the United States of America**  
**Available to DOE and DOE contractors from the**  
**Office of Scientific and Technical Information,**  
**P.O. Box 62, Oak Ridge, TN 37831-0062;**  
**ph: (865) 576-8401**  
**fax: (865) 576-5728**  
**email: reports@adonis.osti.gov**

**Available to the public from the National Technical Information Service,**  
**U.S. Department of Commerce, 5285 Port Royal Rd., Springfield, VA 22161**  
**ph: (800) 553-6847**  
**fax: (703) 605-6900**  
**email: orders@ntis.fedworld.gov**  
**online ordering: <http://www.ntis.gov/ordering.htm>**



This document was printed on recycled paper.

**Development of a Microchannel  
*In Situ* Propellant Production System**

KP Brooks  
SD Rassat  
WE TeGrotenhuis

September 2005

Prepared for  
the National Aeronautics and Space Administration  
Lyndon B. Johnson Space Center

Sponsored by the U.S. Department of Energy  
under Contract DE-AC05-76RL01830

Pacific Northwest National Laboratory  
Richland, Washington 99352

## Executive Summary

An *in situ* propellant production plant (ISPP) on future Mars robotic missions can produce oxygen (O<sub>2</sub>) and methane (CH<sub>4</sub>) that can be used for propellant for the return voyage. By producing propellants from Mars' atmospheric carbon dioxide (CO<sub>2</sub>) and hydrogen (H<sub>2</sub>) brought from Earth, the initial mass launched in low Earth orbit can be reduced by 20 to 45%, as compared to carrying all of the propellant for a round-trip mission to Mars' surface from Earth. Furthermore, by utilizing ISPP, both robotic and manned missions to Mars can be enhanced, enabled, and extended. The propellant generated can provide fuel for hoppers and rovers for increased mobility on the surface, allow additional propellant to be created to increase the return trip payload, and provide oxygen for longer mission stays. With a durable heat source, this ISPP could also use *in situ* sources of hydrogen to provide a sustainable propellant supply.

Pacific Northwest National Laboratory used microchannel architecture to develop a Mars-based *In Situ* Propellant Production (ISPP) system. This three-year research and development effort focused on process intensification and system miniaturization of two primary subsystems: a thermochemical compressor and catalytic reactors. Both of these systems were designed based on a robotic direct return mission scenario, but can be scaled up to human flight missions by simply numbering up the microchannel devices. A microchannel condenser/phase separator was developed under another NASA project. The results of this device are provided here to offer insight on performance of another necessary system component.

The thermochemical collection and compression of CO<sub>2</sub> was developed using absorption and adsorption. Both membrane and microwicking absorbers were evaluated using 100- and 240- $\mu$ m microchannels. CO<sub>2</sub> was absorbed from a 20%-CO<sub>2</sub>:80%-N<sub>2</sub> mixture into either a diethanolamine/water (DEA) or a DEA/PEG solution. Improved mass transfer was observed for the thinner films. Overall mass transfer coefficients were as much as 2.6 times greater than a conventional packed column for the thinnest microwick and about 7.1 times greater for the membrane system.

A multichannel adsorption system was designed to meet the full-scale CO<sub>2</sub> collection requirements using temperature swing adsorption. Each stage is designed to achieve a 10x compression of CO<sub>2</sub>. A compression ratio to collect Martian atmospheric CO<sub>2</sub> at ~0.8 kPa and compress it to at least 100 kPa can be achieved with two adsorption stages in series. A compressor stage incorporates eight thermally coupled adsorption cells at various stages in the adsorption/desorption cycle to maximize the recuperation of thermal energy and provide a nearly continuous flow of CO<sub>2</sub> to the downstream reactors. Experimental work was performed in a single channel adsorber to validate this process. A temperature cycle between 12 and 77°C could be achieved in less than two minutes with greater than 90% of theoretical working capacity. A diurnal cycle thermal-swing adsorption system requires more than 100-times more adsorbent than a microchannel sorption pump operating on 2-minute cycles. This difference results in a significant reduction in system mass.

In an ISPP, the thermochemically compressed CO<sub>2</sub> is then mixed with hydrogen gas and fed to two reactors: a Sabatier Reaction (SR) unit and a Reverse Water/Gas Shift (RWGS) unit. By using both of these reactors in parallel, the required 3.8 mass ratio of oxygen to methane can be

achieved. The microchannel architecture allows better heat control than is possible in an adiabatic system, resulting in significantly higher conversion. By combining the heat exchangers and reactors into a single unit, the reactor systems can also have reduced mass over conventional hardware. Testing with the RWGS and SR units was encouraging. Over 60% conversion was achieved using a two-stage RWGS reactor in which water was removed between stages. Even higher conversions can be achieved by using higher than stoichiometric quantities of hydrogen. SR conversions of greater than 85% were achieved in a single-stage system. Since the RWGS is endothermic and the SR is exothermic, by combining the two reactions, heat generated from the SR can be used to fuel the RWGS reaction. A combined SR/RWGS reactor was successfully tested. Such a system can further reduce system mass and volume.

Both the Sabatier and RWGS reactions generate water. The water will be collected and electrolyzed to produce oxygen and recycle the hydrogen. A microchannel phase separator was developed to separate liquid water from vapor and other gases in these product streams. This separator relies on surface forces, not gravitational effects, to separate the water and is, therefore, suited to space applications. Testing of the condenser/phase separator was demonstrated in zero gravity. The specific energy of this device reached values of 1200 to 8000 W/K for water mole fractions of 20 to 70%. The phase separator technology was scaled up in a system to removed water from a cathode effluent of a 5-kW PEM fuel cell. In this case, a three-channel device can remove 43 mL/min of water in 95 SCFM of air. This exceeded the design requirements of the device.

A system model of the microchannel ISPP plant was generated to predict the size, weight, and performance for the individual components and use it to optimize the overall system. System mass was compared as a function of operating pressure. The study showed that the overall system size is minimized at 3 to 4 bar pressure. An absorption system was used in the model for CO<sub>2</sub> compression. While the CO<sub>2</sub> compressor dominates the mass of the system for a human-scale mission, it is smaller than the JSC baseline. In terms of volume, it was considerably smaller.

The microchannel technologies developed for CO<sub>2</sub> collection, reaction, and phase separation can be used not only for an ISPP system, but also life support, EVA, and lunar applications. The use of microchannel technologies reduces both mass and volume of the system as well as improving the system efficiency.

## Contents

1.0	Introduction .....	1.1
2.0	System Design Overview .....	2.1
3.0	CO <sub>2</sub> Compression Subsystem.....	3.1
3.1	CO <sub>2</sub> Absorption System Development .....	3.2
3.2	CO <sub>2</sub> Adsorption System Development .....	3.10
3.2.1	Development and Testing of a Single-Channel Adsorber .....	3.11
3.2.2	Multi-Channel, Multi-Cell Adsorber .....	3.13
4.0	Reactor Subsystem .....	4.1
4.1	Experimental Approach .....	4.1
4.2	RWGS Reactor Study .....	4.4
4.3	Sabatier Reactor Study.....	4.8
4.4	Combined RWGS/SR System.....	4.13
4.5	Data Evaluation.....	4.17
5.0	Phase Separation and Partial Condensation .....	5.1
6.0	System Modeling.....	6.1
6.1	System Modeling Approach .....	6.1
6.2	System Parametric Studies.....	6.3
6.3	Comparison of the “microISPP” Plant to Mission Baselines .....	6.6
7.0	Conclusions .....	7.1
8.0	References .....	1

## Tables

Table 3.1.	Langmuir-Freundlich Isotherm Fit Parameters for CO <sub>2</sub> Adsorption on Zeolite 13X for CO <sub>2</sub> Partial Pressures in kPa .....	3.18
Table 3.2.	Summary of calculated titanium mesochannel CO <sub>2</sub> adsorber characteristics to produce compressed CO <sub>2</sub> for a Mars direct sample-return mission.....	3.21
Table 4.1.	Catalyst Target Performance Criteria Provided to the BMI Catalyst Development Team .....	4.1
Table 4.2.	Variables Investigated in Catalyst Testing.....	4.2
Table 4.3.	Effect of Reactant Partial Pressure on the RWGS Reaction .....	4.14
Table 4.4.	Effect of Reactant Gas Partial Pressure on the Sabatier Reaction <sup>a</sup> .....	4.15
Table 4.5.	Combined RWGS/SR Reactor Results Summary.....	4.17

## Figures

Figure 2.1.	Process flow diagram of an In Situ Propellant Production System using CO <sub>2</sub> from the Martian atmosphere and hydrogen from Earth or subsurface water on Mars to generate methane and oxygen. ....	2.1
Figure 3.1.	A Semi-transparent Rendering of One Section of the Three-parallel Microchannel Membrane Contactor Absorber.....	3.3
Figure 3.2.	A Photograph of One Section of the 3-parallel Microchannel Membrane Contactor Absorber.....	3.4
Figure 3.3.	Schematic of a Single-channel Microwick Absorber.....	3.5
Figure 3.4.	Photograph of an Assembled Aingle-channel Microwick Absorber .....	3.5
Figure 3.5.	CO <sub>2</sub> loading in 2-M DEA/water as a function of the inverse Peclet number for varying liquid film thickness obtained in three microwick contactors and one membrane contactor.....	3.7
Figure 3.6.	Flux of CO <sub>2</sub> to a 2-M DEA/PEG solution in a microchannel membrane contactor absorber peaks at ~50°C and increases at higher liquid flow rates. (A 62-s absorbent liquid residence time corresponds to a flow rate of 0.05 mL/min.).....	3.8
Figure 3.7.	As the liquid flow rate increases, the fraction of CO <sub>2</sub> removed from the feed stream increases, and the fraction of the DEA CO <sub>2</sub> capacity utilized decreases correspondingly.....	3.9
Figure 3.10.	Schematic of an Eight-cell CO <sub>2</sub> Sorption Pump, with Heat Recuperation via a Heat Exchange Flow Loop .....	3.14
Figure 3.11.	An Arrangement of Four Unique Shim Types Defines Heat-exchange Fluid, Gas Flow, and Adsorbent Channels within a Single Repeat Unit of a Flow-by Adsorber (sample dimensions are in millimeters). ....	3.15
Figure 3.12.	Plan View of Shims in a Repeat Unit Demonstrating the Octagonal Symmetry of an Eight-cell Adsorber .....	3.16
Figure 3.13.	An exploded view of multiple repeat units, capping heat-exchange shims, and endplates arranged for bonding.....	3.17
Figure 3.14.	A completed adsorber with tube stubs for external adsorbate gas and heat-exchange fluid connections.....	3.17
Figure 3.15.	The specific productivity of titanium and stainless steel adsorbents as a function of compression ratio ( $P_{CO_2 \text{ Des}} / P_{CO_2 \text{ Ads}}$ ) for two adsorption/desorption operating temperature ranges. ....	3.19
Figure 3.16.	Operational characteristics of a two-stage rapidly cycled mesochannel adsorption system operating between -50 °C and 100 °C and designed to produce 0.81-kg CO <sub>2</sub> /hr for ISPP during a Mars robotic sample-return mission. ....	3.20
Figure 4.2.	Single channel testing of the RWGS engineered catalyst at 35 ms residence time and stoichiometric conditions. ....	4.4
Figure 4.3.	One of the three shims used to fabricate the RWGS reactor.....	4.5
Figure 4.4.	Photograph of the completed RWGS reactor. This unit was designed to be half scale for the direct robotic return mission.....	4.5

Figure 4.5.	RWGS reaction CO <sub>2</sub> conversion and CO selectivity at H <sub>2</sub> /CO <sub>2</sub> ratio= 1 and contact times of 18.3 ms and 36.5 ms. ....	4.6
Figure 4.6.	RWGS reaction CO <sub>2</sub> conversion varying H <sub>2</sub> /CO <sub>2</sub> ratio and contact times at a reactor outlet temperature of 700°C. ....	4.7
Figure 4.7.	Conversion and selectivity for two RWGS reactors in series removing the water between to increase conversion. ....	4.8
Figure 4.9.	Flow Distributor Shim from the Sabatier Reactor. ....	4.10
Figure 4.10.	Photograph of the completed Sabatier reactor. ....	4.11
Figure 4.11.	Conversion and selectivity of the SR as compared to thermodynamic calculations. ....	4.12
Figure 4.12.	Deactivation of the SR catalyst over time. ....	4.12
Figure 4.13.	The combined RWGS/SR reactor with its associated recuperative heat exchangers. Both the reactor and the heat exchangers operate in the U-configuration (gases exit on the same side as they enter). ....	4.14
Figure 4.14.	RWGS experimental data compared to the model for the 8 channel reactor data. ....	4.15
Figure 4.16.	Heat generated by the SR and heat required by the RWGS are compared as a function of specific methane productivity at the required methane to water ratio. ....	4.18
Figure 4.17.	CO <sub>2</sub> conversion for both the RWGS and the SR reactions as a function temperature for the isothermal and differential temperature approaches. ....	4.19
Figure 4.18.	Concentration of product in the reactor outlet as a function of reactor mass. By increasing the reactor throughput rate, the mass of the RWGS and SR reactors can be decreased. ....	4.20
Figure 5.2.	Single channel proof-of-concept phase separator. ....	5.2
Figure 5.3.	Percent of feed liquid recovered from the liquid outlet for water as a function of gas-to-liquid Reynolds number ratio (Re <sub>GS</sub> /Re <sub>LS</sub> ) for varying pressure differences across the pore throat. ....	5.2
Figure 5.4.	Single channel device running with flow from left to right at flow rates of 40 mL/min of water and 1 SLPM of air. ....	5.3
Figure 5.5.	Close-up of one end of the air-cooled partial condenser-phase separator that was demonstrated in zero gravity on NASA's KC-135. ....	5.4
Figure 5.6.	Thermal energy density and specific power versus percent water in the feed at condensing stream air flows of 11 SLPM (+), 10 SLPM (◇), 9 SLPM (Δ), 8 SLPM (x), 7 SLPM (○) and 5 SLPM (■). ....	5.4
Figure 5.7.	Multichannel phase separator device built to remove water from the cathode effluent of a 5 kW PEM fuel cell. ....	5.5
Figure 6.1.	Example section of the flow sheet page of the microchannel ISPP system modeling tool. ....	6.1
Figure 6.2.	Schematic of a potential Mars ISPP plant for producing oxygen and methane from a high temperature heat source. ....	6.4
Figure 6.3.	Effect of operating pressure on the mass of the ISPP plant (■), the ISPP plant plus power and cooling cycles (▲), and the condenser operating temperature to achieve 98% water recovery from the reverse water gas shift reactor effluent (◆). ....	6.5

Figure 6.4.	Effect of CO <sub>2</sub> diffusivity in the solvent on the mass of the ISPP plant (◆), the mass of the overall absorption cycle CO <sub>2</sub> compressor (■), and the mass of absorber component only (▲). .....	6.6
Figure 6.5.	Comparison of component masses for the CO <sub>2</sub> compression and chemical conversion processes including associated heat exchangers between the “microISPP” plant and the baseline human scale mission to Mars.....	6.8
Figure 6.6.	Comparison of component volumes for the CO <sub>2</sub> compression and chemical conversion processes including associated heat exchangers between the “microISPP” plant and the baseline human scale mission to Mars.....	6.8
Figure 6.7.	Comparison of electrical and thermal demands for the CO <sub>2</sub> compression and chemical conversion processes including associated heat exchangers between the “microISPP” plant and the baseline human scale mission to Mars.....	6.9

## 1.0 Introduction

Numerous studies have supported the use of *in situ* resources to reduce mission mass, cost, and risk for both robotic and human exploration, as well as to enhance, extend, or enable science and exploration objectives (Kaplan, 1996; Connolly and Zubrin, 1996; Zubrin et al. 1997; Reddig and MacKnight, 1997; Green et al. 1999; Sridhar et al. 2000, 2004). Previous studies have shown that producing propellants from Mars' atmospheric CO<sub>2</sub> and hydrogen brought from Earth can reduce initial mass launched by 20 to 45%, as compared to carrying all of the propellant for a round-trip mission to Mars (Sanders et al. 2001). These reductions could be further improved if *in situ* hydrogen were used.

This approach can also reduce risk because propellant for the return trip and oxygen for life support can be produced by an earlier mission before a manned mission leaves earth (Zubrin 1996). Furthermore, propellant production on Mars' surface may eliminate the need for in-orbit rendezvous, another significant reduction in risk.

Using *in situ* propellant production (ISPP), the mission can be enhanced, enabled, and extended by providing fuel for hoppers and rovers for increased mobility on the surface, allowing additional propellant to be created to increase the return-trip payload. By producing oxygen from the CO<sub>2</sub> on Mars, this approach will provide for longer mission stays.

The primary resource initially under consideration for future Mars missions is its low-pressure (0.8 kPa), low-temperature (184 to 242 K) atmosphere, which consists of mostly carbon dioxide (95.5%), nitrogen (2.7%), and argon (1.6%), with traces of other gases (0.15% oxygen; <0.03% water) (Kaplan 1988). The proposed system consists of a CO<sub>2</sub> sorption pump, Sabatier reactor, reverse water/gas whiff (RWGS) reactor, Phase Separators, Electrolysis Unit, and Downstream Gas Separation system (i.e., CO removal and CH<sub>4</sub> recovery). This system is designed to collect CO<sub>2</sub> from the Martian atmosphere and react it with hydrogen that has either been electrolyzed from the available subsurface water or brought from Earth to produce methane and water. The water is then separated and electrolyzed to produce oxygen and hydrogen. Hydrogen from the electrolysis unit and unreacted hydrogen and CO<sub>2</sub> from the reactors is recycled to the reactor feed. The oxygen and methane products are cryogenically stored for use as propellant for the return trip to Earth.

For more than 10 years, Pacific Northwest National Laboratory has been developing techniques and concepts for process intensification through rapid heat and mass transfer within microchannels. Engineered microstructures that feature at least one dimension that is 10 to 1000 micrometers facilitate extremely high heat and mass transfer rates and allow significant reductions in hardware volume and mass over conventional hardware. The microchannel architecture consists of cells containing arrays of parallel microchannels. Scale-up is accomplished by "numbering up" several cells in parallel. Consequently, a higher output microchannel system simply requires an increased number of parallel cells either as more small units or more cells in a single unit without compromising the salient features of the individual microchannel. The degree of parallelism associated with this modular approach offers redundancy and system reliability that are highly desirable in space applications.

An additional advantage with microchannel systems is that hydrodynamic, surface, and interfacial forces dominate gravity forces at these small length-scales. Because gravity is not the dominant force, microchannel systems should operate similarly in a reduced gravity environment as they do on Earth. A final feature of microchannels is that their small internal volume results in reduced inventory of flammable or hazardous materials, and their inherent temperature and mass control prevent run-away reactions. This results in increased safety during operations.

Pacific Northwest National Laboratory (PNNL) and the National Aeronautics Space Administration's (NASA's) Johnson Space Center investigated the use of microchannel technology to reduce the size and weight and improve the efficiency of such an ISPP system. This is the final report documenting the results of this study over a 35 month period from December 1999 to November 2002.

## 2.0 System Design Overview

There are four steps to an ISPP operation, 1) resource collection and conditioning, 2) chemical conversions, 3) separations, recycle, and product purification, and 4) storage. One version of this process for use on Mars is shown in Figure 1.1.

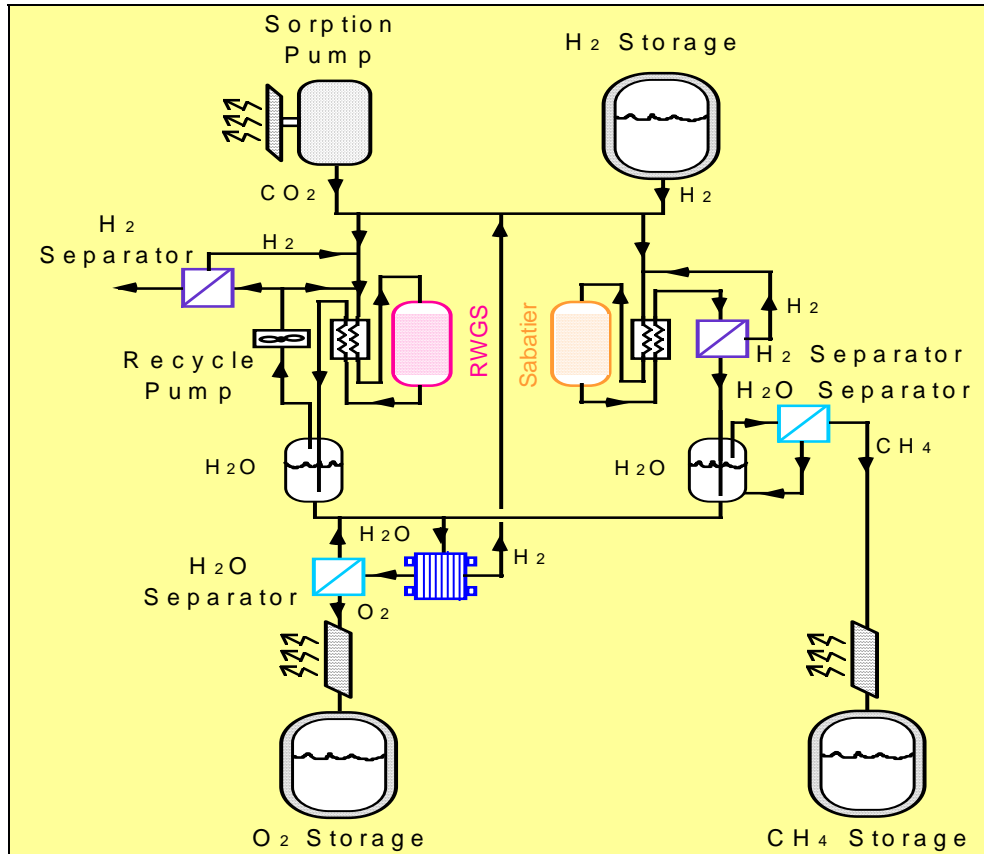
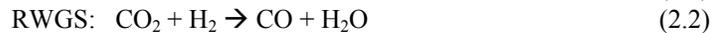
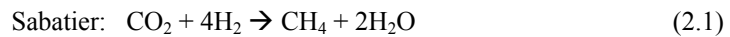


**Figure 2.1:** Process flow diagram of an In Situ Propellant Production System using CO<sub>2</sub> from the Martian atmosphere and hydrogen from Earth or subsurface water on Mars to generate methane and oxygen.

In this process, carbon dioxide is collected from the Martian atmosphere at approximately 6 Torr total pressure and conditioned by compressing to the working pressure of the ISPP plant. Optionally, the CO<sub>2</sub> can be purified from percentage levels of N<sub>2</sub> and Ar. Several options have been suggested for collecting and compressing CO<sub>2</sub> on Mars, including an adsorption compressor (Karlmann et al. 1999), an absorption compressor (TeGrotenhuis et al. 2000), solidification (Simon et al. 2002), and mechanical compression. Here, the development work is focused on microchannel technologies for an absorption cycle and rapid temperature swing adsorption to purify the CO<sub>2</sub> while increasing the pressure of the CO<sub>2</sub> reasonable operating pressures.

The three most commonly used approaches for chemically converting the pressurized CO<sub>2</sub> are 1) zirconia cell electrolysis to produce CO and O<sub>2</sub>, 2) Sabatier reaction with H<sub>2</sub> to produce methane and water, and 3) RWGS reaction with H<sub>2</sub> to produce CO and water (Sanders 2000). Possible scenarios for supplying hydrogen include transporting cryogenically stored H<sub>2</sub> or liquid water from Earth or collecting water from the environment. Most scenarios, including the one represented in Figure 1.1, utilize water electrolysis to produce oxygen as a product and enable recycle of hydrogen to maximize the yield to propellant. Efforts at developing a microchannel-based Martian ISPP plant have focused on the Sabatier and RWGS reactions. Because these are operated at high temperatures, microchannel recuperative heat exchangers have also been developed to minimize reactor heating requirements while minimizing the added size and weight. The Sabatier reaction produces methane and water and the RWGS reaction produces carbon monoxide and water based on the following stoichiometry.



A Sabatier reactor with water electrolysis will provide methane and oxygen at an oxygen:methane ratio of 2:1 (by mass). A RWGS reactor with water electrolysis will provide oxygen only. The combination of Sabatier and RWGS reactions will allow the system to provide propellants at the project-specified ratio of 3.8:1 without wasting any hydrogen as would a Sabatier reactor alone. However, the stoichiometry does require expelling unused CO.

Separation and purification steps have the dual objective of preparing products for storage and the recovery and recycle of material to the process. Many potential options are worth considering, including a hydrogen electrochemical pump, membrane or cryogenic separations, and adsorbent materials. The water from these two reactors is condensed in the microchannel phase separators and sent to the electrolyzer. The water is electrolyzed to produce oxygen to be cryogenically stored for use as propellant. The CO and CH<sub>4</sub> are separated from any remaining H<sub>2</sub> and CO<sub>2</sub>. The CO is exhausted into the environment and the CH<sub>4</sub> is cryogenically stored. The unreacted CO<sub>2</sub> and H<sub>2</sub> are combined with recycled H<sub>2</sub> from the electrolyzer and returned to the reactors.

Research has been performed to develop microchemical processes for some of the major components of this system. Among those studied are the CO<sub>2</sub> compression subsystem using sorption techniques, the reactor subsystem using Sabatier and RWGS reactions, and a vapor/liquid separation subsystem using wicking in microchannels. This work is discussed further in subsequent sections. System sizing is based on NASA's robotic sample-return mission that requires production rates of 0.0977 kg/hr of methane and 0.371 kg/hr of oxygen. System modeling was performed to provide a preliminary assessment and comparison of system sizes and weight, to understand the weight breakdown by subsystem and components, and to provide a framework for future system optimization. The results of this modeling also are presented in a subsequent section.

### 3.0 CO<sub>2</sub> Compression Subsystem

The fact that sorbent materials have a varying affinity for sorbed species that varies as a function of environmental conditions (e.g., temperature and pressure) is the basis of a CO<sub>2</sub> thermochemical compression device. For example, selective adsorbents tend to have a higher capacity for the target adsorbate species (e.g., CO<sub>2</sub>) at lower temperatures. Therefore, thermal cycles in which the sorbent is cooled during adsorption and heated during desorption are a means to capture CO<sub>2</sub> from Mars at a low partial pressure (~0.8 kPa) and subsequently release it at a higher pressure (100 kPa) and concentration for downstream processing in ISPP reactors. This is a thermal-swing adsorption (TSA) thermochemical compression process.

Two approaches to CO<sub>2</sub> compression using microchannel devices were developed as part of this work, CO<sub>2</sub> absorption and CO<sub>2</sub> adsorption:

1. Absorption uses a liquid absorbent, such as 2-M diethanolamine (DEA), confined in microchannels by semi-permeable membranes or by wicking materials. The unsaturated, relatively low-temperature absorbent liquid is contacted with a low-partial-pressure (low concentration) CO<sub>2</sub> gas stream, and CO<sub>2</sub> is transported to and absorbed in the liquid. The liquid containing absorbed CO<sub>2</sub> is then pumped from the absorbing microchannels to a higher pressure and into a desorption chamber where it is heated; the CO<sub>2</sub> desorbs from the absorbent and is collected at elevated pressure.
2. The second thermochemical compression approach is CO<sub>2</sub> adsorption. In this case a CO<sub>2</sub>-selective solid adsorbent, such as zeolite 13X, is contacted with the low-partial-pressure CO<sub>2</sub> gas stream by either flowing the gas stream through the adsorbent bed in flow-through mode or flowing the gas in a microchannel adjacent to the adsorbent bed, and the gas species diffuse a short distance to the sorption sites (flow-by mode). Using integrated microchannel heat exchangers, the adsorbent is cooled during adsorption and subsequently heated during desorption to create a higher-pressure CO<sub>2</sub> stream.

The CO<sub>2</sub> sorption system development effort for NASA leveraged other microchannel device development projects completed at PNNL. In particular, PNNL Laboratory Directed Research and Development (LDRD) funds were used to develop single-channel adsorbents in FY 2000 (Rassat et al. 2001) and single-channel microwick absorbers in FY 2001 (Rassat et al. 2002). Experimental work to develop the CO<sub>2</sub> absorption and adsorption compression approaches for NASA, including results from the parallel PNNL-funded activities, are described in the subsequent sections.

Initially, both CO<sub>2</sub> absorption and adsorption compression concepts were carried forward in the NASA project. A mid-project decision was made to exclusively pursue the adsorption approach, which is discussed at the conclusion of Section 3.1. The greater advancement of the adsorption system is evidenced in that section. As shown there, a multichannel, multi-cell adsorption system was designed for the Mars direct sample-return mission, and the expected performance of the device was determined using a design-basis calculation tool. The application of the microchannel CO<sub>2</sub> sorption hardware to other NASA needs, such as spacesuits for Extra-Vehicular Activity (EVA), is also discussed.

### 3.1 CO<sub>2</sub> Absorption System Development

The potential applications of sorption techniques, both absorption and adsorption, for targeted gas separations and purification are essentially unlimited, provided sorption media with required specificity and capacity are available. Microchannel absorbers, for example, may have a role in the recovery and recycle of CO<sub>2</sub> and the stripping of CO from RWGS and Sabatier reactor effluent gases in addition to compression of CO<sub>2</sub> as a feedstock to the reactors. Two types of microchannel absorbers—microwick contactor absorbers and membrane contactor absorbers—have been developed by PNNL. In absorption, the rate of mass transfer is usually limited by the diffusion time of the gas species into the liquid. The characteristic diffusion time is proportional to the square of the film thickness, so the time to reach a target gas saturation in the liquid is quartered every time the liquid film thickness is halved. Therefore, thin liquid channels defined by microwicks or membrane contactors provide improved mass transport leading to process intensification as compared to other absorption techniques relying on thicker liquid layers.

Figures 3.1 and 3.2 show a model and a photograph of the three-parallel microchannel membrane contactor absorber designed and fabricated for this project. Four units like those shown in the figures were fabricated in stainless steel, two with 100- $\mu\text{m}$  deep microchannels and two with 200- $\mu\text{m}$  deep channels. A pair of these units placed with microchannel surfaces face-to-face, separated by a porous contactor, and bolted together, create a microchannel absorber. During absorption, liquid absorbent flows through the microchannels on one side of the contactor surface while the CO<sub>2</sub>-containing feed gas flows in the microchannels on the opposite side of the membrane. Note that these laboratory test devices were not optimized for structure mass or efficient heat transfer. They were designed for ease of fabrication using conventional machine tools (e.g., CNC machining). These drawing specification are proprietary, but can be provide to NASA upon request. While the liquid absorbent and gas mass transport regions are microchannels (100- $\mu\text{m}$  or 200- $\mu\text{m}$  deep), the serpentine heat-exchange channels cut in the back of the structures are bulky. They are intended to provide isothermal conditions in a steady-state experiment.

The length of the microchannels in the unit shown in Figures 3.1 and 3.2 (~3 cm) is about one-third the length of a microchannel membrane absorber used in initial screening experiments for this project. The relatively short micro-machined channels accommodate more viscous absorbent liquids at lower pressure drop for a given liquid flow rate. Lower pressure drops minimize breakthrough of the adsorbent liquid through the contactor membrane into the gas channels. By having three fluid channels in parallel, the mass transfer area of the shorter absorber becomes comparable to that of the single, long microchannel found in the interim test device. A set of CO<sub>2</sub> absorption experiments using a water/DEA (~2 molar) absorbent solution was conducted to compare the performance of the shorter and longer channel absorbers (both nominally 100- $\mu\text{m}$  deep). When scaled to account for differences in channel length and contact area, mass transfer results for the newer device were nearly identical to those obtained in the older, longer channel unit. This consistency gives us confidence in our ability to scale the test results for system development.

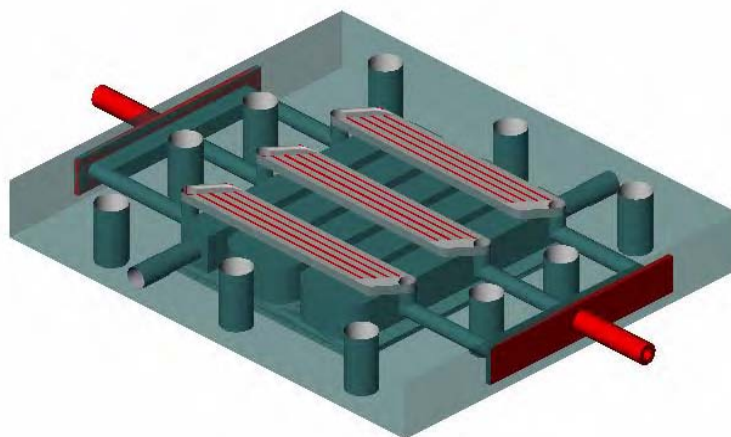


**Figure 3.1.** A semi-transparent rendering of one section of the three-parallel microchannel membrane contactor absorber. The red-lines are membrane support ribs, the red tubes on the ends of the unit are headers feeding the 3-parallel channels, and the gray tubes on the sides of the structure are fluid ports for the serpentine heat-exchange channel.

The porous contactor is also a key component of the microchannel absorber. It is required to be sufficiently porous to allow transport of gas phase species into the liquid absorbent while preventing the liquid from breaking through to the gas channel. A number of contactor materials were evaluated including various commercial polypropylene and Teflon<sup>®</sup> membranes and an engineered contactor created from a plastic film with laser-machined pores. Most of these failed due to low breakthrough pressure (e.g., resulting from large pore sizes or wetting), material incompatibility, or membrane deformation in operation. The greatest success was obtained with Teflon membranes (e.g., Norton<sup>®</sup> Zitex<sup>®</sup> PTFE 1-2  $\mu\text{m}$  pore-size membrane), which were used in the membrane contactor experiments described below.

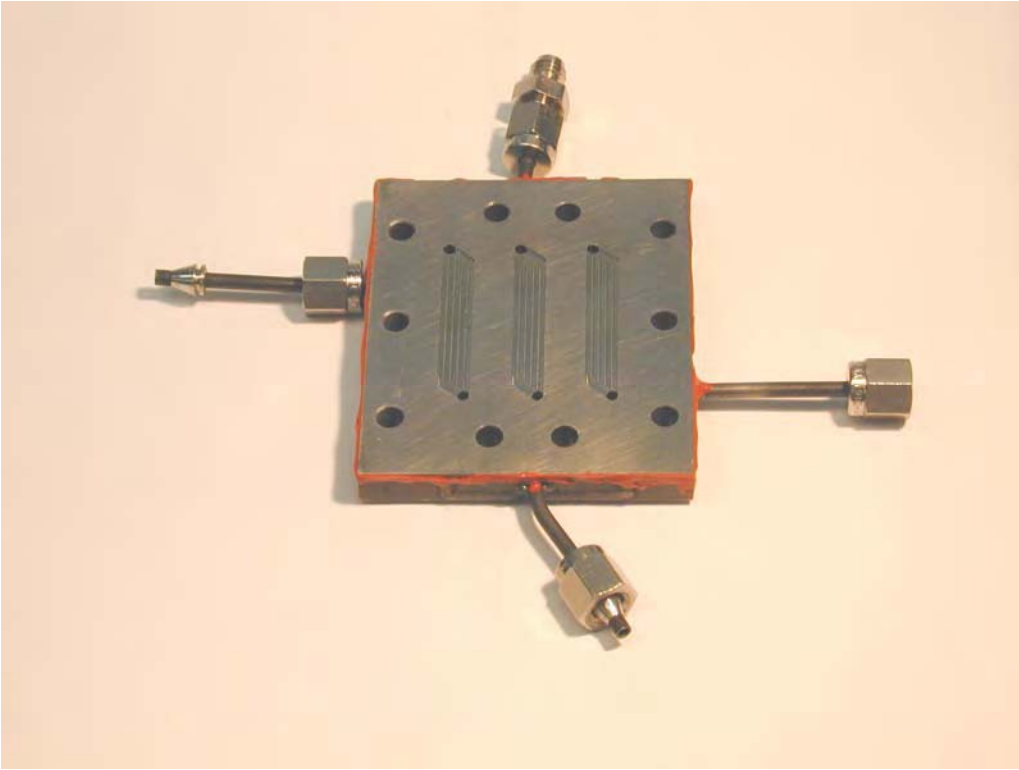


**Figure 3.2.** A photograph of one section of the 3-parallel microchannel membrane contactor absorber. Two similar structures are placed with microchannels face-to-face separated by a porous contactor to create an absorption unit.

A schematic of a single-channel microwick absorber developed and tested on a PNNL LDRD project is shown in Figure 3.3 (Rassat et al. 2002), and a photograph of the assembled test device is shown in Figure 3.4. In the microwick gas absorber, a gas stream flows through a plenum counter-current to (or optionally co-current), and in direct contact with, a liquid stream flowing through a microwick, which is driven by capillary action through the wicking material. Gas intrusion into the liquid outlet is prevented through the application of surface tension forces over a narrow pore throat. Because the processing rate is normally limited by liquid phase mass transfer, a key is to identify and develop wicks that are as thin as possible and have good capillary pumping capacity. Several wicking materials were tested including a ceramic weave, a Kevlar<sup>®</sup> woven material, and a metal screen material. The simple single-channel microwick absorber test unit shown in Figures 3.3 and 3.4 does not incorporate cooling and heating channels, although these can be included in future devices to promote more efficient absorption and desorption via temperature control.

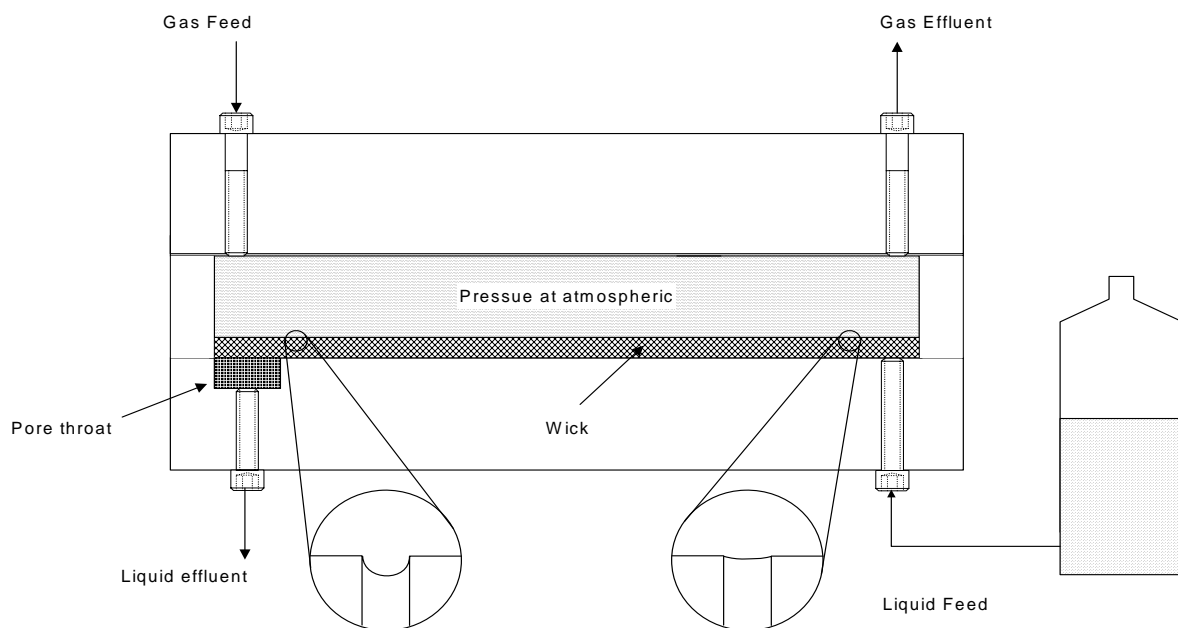


**Figure 3.3.** Schematic of a single-channel microwick absorber.



**Figure 3.4.** Photograph of an assembled single-channel microwick absorber.

In wicks wetted by the absorbent solution, the liquid is preferably confined to the wick volume, and therefore the liquid film thickness is related to the thickness of the wick. As noted above, in a membrane contactor absorber, a machined liquid microchannel of defined thickness is separated from a gas microchannel by a porous membrane, and it is preferred that the sorbent liquid does not wet the contactor material so it does not weep or break through the fine pores of the membrane into the gas channel. If the pressure drop across the membrane is relatively high, as occurs when the liquid flow rate is increased sufficiently, breakthrough is observed. It is difficult

to recover from a membrane contactor breakthrough, because wettability and the pressure driving force do not favor return of the liquid from the gas channel to the liquid channel. The analogous process upset in a microwick absorber is flooding, in which the feed flow rate of liquid exceeds the throughput of the wick. Since the microwick material is wetted, flooding will readily subside into the liquid flow structure when the feed rate is reduced. A challenge for the microwick absorber technology is to create very thin liquid films (e.g.,  $<100\ \mu\text{m}$ ) with high throughput.

The effectiveness of both types of microchannel absorbers for  $\text{CO}_2$  removal was demonstrated experimentally using the same test stand. The test system incorporated a small four-piston positive displacement pump from Encynova, rated to deliver as low as  $0.001\ \text{mL/min}$  absorbent liquid. Low flow rates were necessary to increase residence time for enhanced sorbent capacity utilization and to minimize pressure drop with more viscous sorbent solutions. The flow rate and composition of  $\text{CO}_2$ -containing gas ( $80\% \text{N}_2 / 20\% \text{CO}_2$  unless otherwise noted) in the absorber feed was adjusted using mass-flow controllers, which were plumbed to pressurized gas tanks. Since the gas effluent line from the absorbers was open in a fume hood and not restricted, gas pressure in the absorbers was nominally atmospheric. A slip stream of the gas exiting the absorber was sampled to an Ametek® residual gas analyzer (RGA) to determine the decrease in  $\text{CO}_2$  composition resulting from absorption. In a typical experiment, gas and absorbent liquid were flowed counter-currently at specified rates through the absorber until a steady-state effluent gas concentration was observed. The temperature of absorption (or desorption) in the membrane contactor absorber was controlled by insulating the device and flowing water through it from a thermostatically controlled water bath. The absorbent liquid could also be heated prior to feeding into the absorber by passing it through a coil of tubing placed in the water bath.

The performance of membrane contactor and wicking microchannel absorbers was compared directly in one set of experiments.  $\text{CO}_2$  was absorbed from a  $20\% \text{-CO}_2:80\% \text{-N}_2$  mixture into a 2-M DEA/water solution. Gas-flow was maintained at a sufficient level to preclude gas-phase mass-transfer limitations. As noted above, the composition of the effluent gas stream was determined with an RGA; the change in gas composition (feed to effluent) was used to evaluate  $\text{CO}_2$  mass transfer into the flowing DEA solution.

Results for three microwick contactor experiments using wicks of various materials and thicknesses ( $150\ \mu\text{m}$ ,  $190\ \mu\text{m}$ , and  $280\ \mu\text{m}$ ) and a membrane contactor test using a  $100\text{-}\mu\text{m}$  liquid microchannel are presented in Figure 3.5. The results of all the experiments are correlated in terms of the inverse mass-transfer Peclet number ( $\text{Pe}_m^{-1}$ ), which is defined as the solute diffusivity (DEA diffusion, in this case) multiplied by the liquid residence time divided by the wick thickness squared. Equilibrium uptake of  $\text{CO}_2$  is sensitive to temperature and  $\text{CO}_2$  partial pressure and is  $0.5\text{-}0.65$  moles  $\text{CO}_2$  per mole of DEA at the conditions tested (room temperature,  $20$  to  $25^\circ\text{C}$ ). The objective was to achieve high solvent loading with a minimum residence time, as this would lead to reduced sorbent mass in a separation/purification system. Near equilibrium loading of  $\text{CO}_2$  is achieved at  $\text{Pe}_m^{-1}$  above  $10$ , where performance is limited by solvent capacity for the solute. The data suggest, as expected, that the liquid residence time needed to achieve a high  $\text{CO}_2$  loading is reduced when the liquid film is thin. Overall mass-transfer coefficients were also determined from the data shown in Figure 3.5 and were compared to those typical of conventional packed towers using 2-M monoethanolamine/water solutions (Kohl and Nielsen 1985). The overall mass-transfer coefficients were as much as  $2.6$  times greater for the thinnest

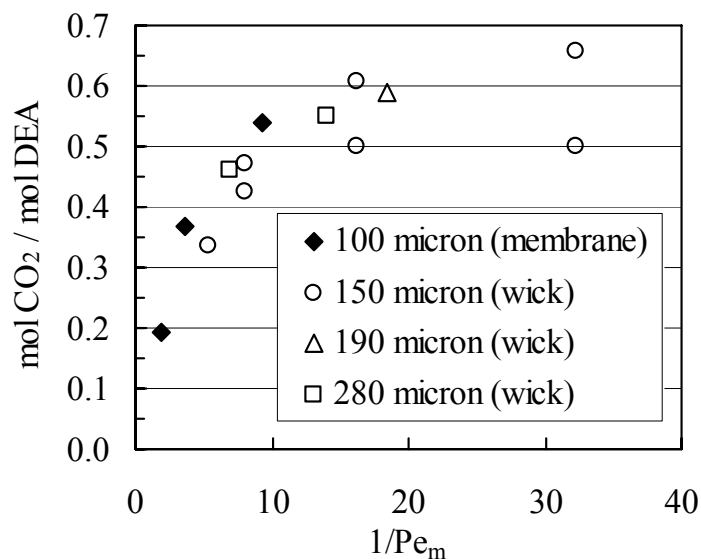


**Figure 3.5.** CO<sub>2</sub> loading in 2-M DEA/water as a function of the inverse Peclet number for varying liquid film thickness obtained in three microwick contactors and one membrane contactor.

microwick and about 7.1 times greater for the membrane system. Again, this is an indicator of the process intensification possible with thin absorbent liquid films.

For space applications, water is not likely the preferred solvent for absorption systems because of its relatively high vapor pressure. Using the membrane contactor absorber described above, a series of experiments was completed in which the solvent water was replaced with a much less volatile polyethylene glycol (PEG; PEG-400). The microchannel absorber incorporated heat exchangers on both the liquid and gas sides, and this feature was used in several experiments to evaluate mass transfer rates as a function of temperature in the range ~25 to ~80 C. Results are shown in Figure 3.6. Reduced liquid viscosity with increasing temperature had a two-fold benefit: first, the mass transfer rate increased, most likely due to increased mass diffusivity in the liquid; second, the liquid pressure drop across the device was reduced. This allowed higher liquid flow rates to be evaluated without liquid breakthrough across the contactor membrane. At a given sorbent flow rate (residence time), increasing the temperature of absorption above ambient also resulted in an increased conversion of DEA to amine-CO<sub>2</sub> product (Figure 3.6). Optimum CO<sub>2</sub> scrubbing efficiency was observed at an intermediate temperature near 50°C. The decrease in CO<sub>2</sub> sorption at higher temperatures is expected, as the reverse reaction leading to desorption (or less absorption) of CO<sub>2</sub> from the amine is favored. This is the basis of a continuously regenerated thermal swing absorption process.

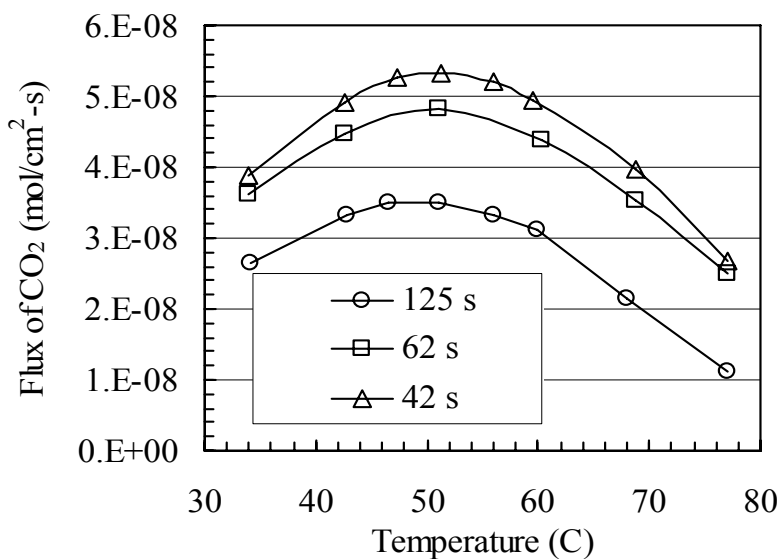


**Figure 3.6.** Flux of CO<sub>2</sub> to a 2-M DEA/PEG solution in a microchannel membrane contactor absorber peaks at ~50°C and increases at higher liquid flow rates. (A 62-s absorbent liquid residence time corresponds to a flow rate of 0.05 mL/min.)

Also note in Figure 3.6 that the CO<sub>2</sub> flux increases as the absorbent residence time decreases. The flux is higher when the CO<sub>2</sub> loading of the sorbent is low and  $Pe_m^{-1}$  is small (Figure 3.5). The inverse relationship between CO<sub>2</sub> flux and degree of sorbent saturation is further demonstrated in Figure 3.7. These data were obtained at 51°C, near the optimum temperature (see Figure 3.6). At the lowest liquid flow rate tested (0.01 mL/min), the estimated fraction of sorbent amine reacted was ~0.54. The fraction reacted fell to ~0.1 when the liquid flow rate was increased to 0.20 mL/min. Over the same flow rate range, the amount of CO<sub>2</sub> scrubbed from the gas feed stream increased from ~30% to almost 95%.

Additional experiments were conducted to evaluate the effect of absorption temperature on CO<sub>2</sub> uptake into a more concentrated 3-M DEA in PEG solution at a fixed liquid flow rate. As with previous tests using 2-M DEA (Figure 3.6), the CO<sub>2</sub> flux peaked at a somewhat elevated temperature. In the case of the 3-M solution, the optimum absorption temperature appeared to be approximately 5°C higher than the ~51°C peak noted for the 2-M solution. It is not surprising that the peak temperature would vary with solution composition, as key properties such as viscosity and diffusion coefficient are temperature and concentration dependent. Other tests were completed for the 3-M solution at its “optimum” absorption temperature, varying the liquid flow rate and holding other parameters constant. Flow rate dependence was similar to that observed with the ~2-M DEA/PEG solution, as shown in Figure 3.7. However, at each flow rate, the estimated CO<sub>2</sub> uptake rate (flux) was greater for the more concentrated amine solution, likely due to the increase in reactive DEA species at the gas-liquid interface. At a low flow rate (0.01 mL/min), the flux was ~30% higher in the 3-M solution ( $2.5 \times 10^{-8}$  compared to  $1.9 \times 10^{-8}$  mol CO<sub>2</sub>/cm<sup>2</sup>-s). The fractional difference fell with increasing flow rate; at 0.10 mL/min, the flux

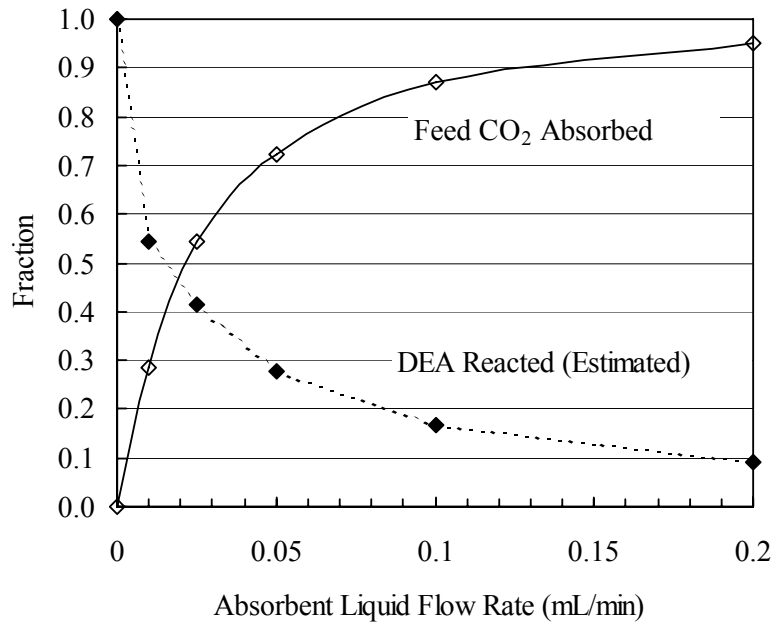


**Figure 3.7.** As the liquid flow rate increases, the fraction of CO<sub>2</sub> removed from the feed stream increases, and the fraction of the DEA CO<sub>2</sub> capacity utilized decreases correspondingly. Data were obtained at ~51 C, near the optimum absorption temperature.

increase was <10% ( $6.2 \times 10^{-8}$  compared to  $5.8 \times 10^{-8}$  mol CO<sub>2</sub>/cm<sup>2</sup>-s). Although there is a modest increase in CO<sub>2</sub> flux (absolute CO<sub>2</sub> concentration in solution) in the 3-M case, the fraction of the feed DEA reacted with CO<sub>2</sub> (fractional conversion) was lower.

Gas-side mass transfer will be considerably different with Martian atmosphere at 95% CO<sub>2</sub> and 6 torr than with the 20% CO<sub>2</sub> in nitrogen at 1 bar pressure that was used in these experiments. Nevertheless, two types of experiments were run to evaluate effects of gas-side mass transport. In one, the flow rate of feed gas was doubled from 2.5 mL/min to 5 mL/min. The depth of the gas channel was also varied, replacing the baseline 200- $\mu$ m-deep gas channel with a 100- $\mu$ m equivalent. The combination of gas flow rates and channel depths resulted in gas residence times varying from ~0.6 to 2.5 s. Increasing the gas flow rate at a fixed channel depth resulted in an increased flux of CO<sub>2</sub> to the DEA/PEG. When the liquid flow rate was low (e.g., 0.01 mL/min), the effect of gas flow rate on estimated flux was relatively low (~10% difference), while the difference increased to ~30% when the liquid flow rate was increased to 0.2 mL/min. The increase in flux with gas flow rate was likely the due to the increase in gas-phase CO<sub>2</sub> concentration. The shorter gas residence time at a high flow rate resulted in higher measured effluent CO<sub>2</sub> concentration, higher bulk average CO<sub>2</sub> concentration in the reactor, and thus a greater concentration driving force.

For scale-up purposes, the CO<sub>2</sub> flux or absorption rate is significant. Data suggest that increasing the gas flow rate and the DEA concentration could result in increased flux. Greater flux could also be expected by increasing the liquid flow rate, but this would lead to larger pressure drops

and increased risk of liquid breakthrough in the contactor membrane. Finally, thinner gas and liquid channels, where practical, should lead to higher flux, as was observed in initial screening experiments which showed increased performance of 100- $\mu\text{m}$ -deep, single, long liquid microchannels compared to 240- $\mu\text{m}$ -deep channels. Improved mass-transfer rates with thinner absorbent liquid films were also observed in microwick absorption experiments (Figure 3.5).

In addition to these factors, the absorbent liquid solvent properties are important. Because of the relatively high viscosity of PEG and a corresponding reduction in DEA diffusivity compared to that in water, mass-transfer rates were lower for DEA/PEG. At room temperature, the  $\text{CO}_2$  mass flux to a 2-M DEA/water solution was 5 to 10 times greater than that for comparably configured devices using a 2-M DEA/PEG sorbent. Qualitatively, this difference was expected because of the relatively high viscosity and low mass diffusivity of the PEG sorbent. Since water may not be an acceptable solvent for space applications, this is further indication of the need for microchannel liquid absorbers (microwick or membrane contactor) integrated with heat exchange. Advancements in wicking microtechnology will result from thinner, higher permeability, and smaller pore size wicks. Membrane contactor absorbers will benefit from robust membranes that are less susceptible to breakthrough. Both microwick and membrane contactor absorption approaches are amenable to scale up in multi-channel systems, and this is another future challenge.

During the course of this NASA project, a decision was made to pursue adsorption rather than absorption for an eighth-scale laboratory prototype of a unit for the Mars robotic sample-return mission. This decision was based in part on the higher degree of advancement of the adsorption technology as well as ease of fabrication, process robustness, durability and maintenance requirements, sorbent lifetime and recovery, device mass, and energy efficiency. Furthermore, there are possible robustness issues due to absorbent liquid breakthrough of the porous membranes. These robustness issues may be overcome with advancements in microwick absorbers. In contrast, energy efficiency, in theory, was favored by an absorption process because of the relative ease of transferring heat from the hot spent sorbent liquid exiting the desorber to the cold  $\text{CO}_2$ -loaded liquid from the absorber in a countercurrent microchannel heat exchanger. To overcome this potential energy efficiency limitation in micro-scale adsorbers, less-obvious methods of thermal recuperation are proposed in the adsorption system as described in detail in the following section.

## **3.2 $\text{CO}_2$ Adsorption System Development**

As noted previously, thermal cycles in which an adsorbent material is cooled during adsorption and heated during desorption, are a means to capture  $\text{CO}_2$  from the Martian atmosphere at a low partial pressure ( $\sim 0.8$  kPa) and subsequently release it in a much more concentrated form (e.g., 100 kPa) to feed Sabatier and RWGS reactors. The throughput or production rate of compressed  $\text{CO}_2$  (e.g.,  $\sim 0.81$  kg/hr required for the Mars robotic sample return) is a function of the amount of sorbent in the system, the difference in sorption capacity at the adsorbing temperature and pressure and at the desorbing temperature and pressure, and the frequency of cycling between these two end states. By cycling rapidly to achieve semi-continual  $\text{CO}_2$  delivery and sorbent regeneration, the specific productivity of the sorbent [(kg- $\text{CO}_2$ /s)/kg-sorbent] is increased over a more-conventional long-cycle TSA process (e.g., a Mars diurnal cycle). The required adsorbent

mass scales linearly with the cycle time. Micro-scale adsorbers are ideally suited to rapid thermal cycles, and, as a result, the mass of sorbent and the device hardware are reduced.

As with the microchannel absorbers discussed in the previous section, the development of an adsorption-based CO<sub>2</sub> thermochemical compressor started with single-channel devices, which were readily fabricated and tested in the laboratory (Rassat et al. 2001). Much of this foundational work was completed on PNNL-funded LDRD projects. Subsequently, concepts for much more complex multi-channel and multi-cell adsorbers were developed and patented (Wegeng et al. 2003, 2004). The fabrication-ready design of a multichannel, multi-cell adsorber and its basis in single-channel test units is discussed below. Further, the expected properties of a CO<sub>2</sub> adsorber of this design scaled for a Mars direct sample-return mission are described.

### 3.2.1 Development and Testing of a Single-Channel Adsorber

Several compact single-channel adsorbers, such as that shown in Figure 3.8, were fabricated and tested to demonstrate proof-of-concept for CO<sub>2</sub> capture and subsequent delivery in rapid adsorption/desorption cycles (Rassat et al. 2001; Brooks et al. 2002; Wegeng et al. 2003, 2004). Integrating heat-exchange microchannels on both sides of a single adsorbent-filled mesochannel results in devices that are well suited to thermal swing adsorption processes. (Here, “microchannels” are defined as those having a depth < 1 mm, whereas “mesochannels” may be up to 1-cm deep.) Heat-exchange fluid was delivered to and received from the heat-exchange microchannels using a common header/footer system, while an independent header/footer system was used to deliver and collect adsorbate gas species to and from the sorbent. A thin solid heat-transfer wall isolated the heat-exchange fluid from the adsorbent bed and through which heat was transferred to or from the adjacent layer of adsorbent. These single-adsorbent channel test units were flow through adsorbers, in which the adsorbate and carrier gas flowed through the interstices of the adsorbent bed.

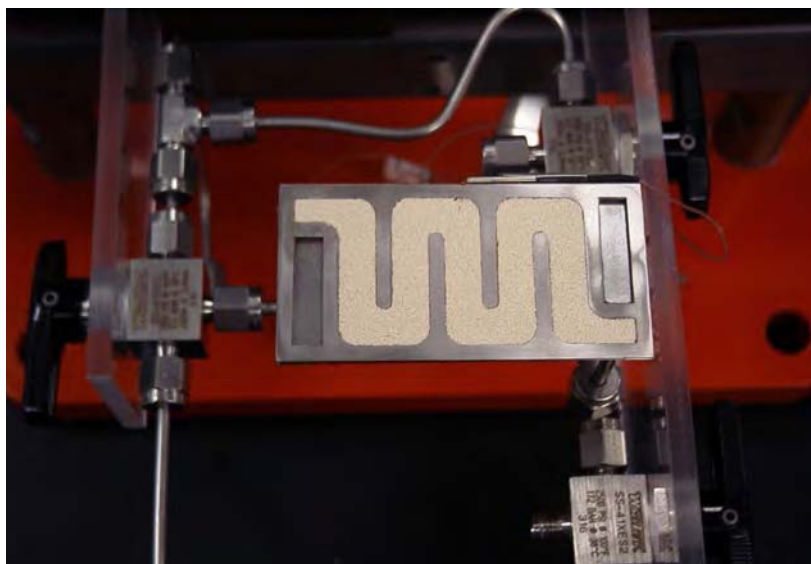


**Figure 3.8.** A stainless steel single-channel, microchannel adsorber filled with zeolite adsorbent. Another heat exchanger (not shown) covers the exposed adsorbent bed.

Single-channel adsorbers were fabricated from a variety of materials including all metal (Figure 3.8), all plastic, and metal-plastic composites (Rassat et al. 2001). Figure 3.9 demonstrates the simultaneous heat- and mass-transfer effectiveness for the three types of single-channel micro-scale adsorbers during desorption cycles, starting with CO<sub>2</sub>-loaded zeolite at 7°C. In all cases, heat was delivered to the adsorber heat exchangers via a constant water flow rate from a 90°C reservoir. Figure 3.9a indicates a somewhat lower rate of temperature change in the all-plastic device than in the all-metal and metal-plastic composite devices. However, after ~70 s, the temperatures in the all-plastic device match those in the all-metal device, and at longer times the temperatures in the all-plastic device exceed those in the all-metal device by a few degrees. This may be due to the lower thermal mass and lower heat loss associated with the plastic unit. The temperature profile for the metal-plastic composite adsorber demonstrates the superior qualities of each of the other units. It shows rapid heat transfer to the adsorber bed, the rate of temperature change exceeding the all-metal device after ~15 s. The metal-plastic composite also attained a slightly higher maximum temperature than the all-metal device, suggesting relatively low heat loss as in the all-plastic device. The profiles of gas evolution from these three devices (Figure 3.9b) show similar trends. Gas desorption was fastest in the metal-plastic device and slowest in the all-plastic unit. The results suggest that heat transfer rather than mass transfer is the primary limitation in the regeneration process of these flow-through single-channel adsorbers. Note also in Figure 3.9b that >90% of the total volume of desorbed CO<sub>2</sub> was released in <60 s.

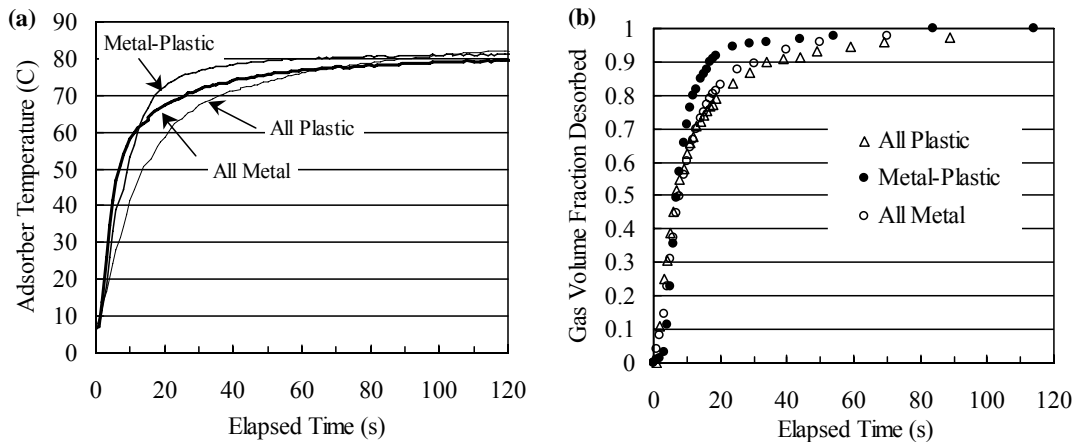


**Figure 3.9.** (a) Thermal and (b) Mass Transfer Performance of Three Micro-scale Adsorber Assemblies during Desorption

The following is an example typical of experiments completed to assess the performance of single-channel adsorbers. The tests were isobaric (atmospheric pressure, ~100 kPa) and operated in a two-phase TSA cycle. A stainless steel unit (Figure 3.8) containing 1.2-g zeolite 13X was cycled with a minimum measured adsorption temperature,  $T_l$ , of 12°C and a maximum desorption temperature,  $T_h$ , of 77°C using water as a heat-exchange fluid. Pure CO<sub>2</sub> was fed through the zeolite at the rate of ~50 mL/min during a ~60-s adsorption phase in which the adsorbent was cooled from  $T_h$  to  $T_l$ . The desorption phase, including the time to heat from  $T_l$  to  $T_h$ , was also ~60 s, resulting in an overall cycle time of 2 min. During the heating portion of the cycle, about 46 mL of CO<sub>2</sub> (measured at room temperature, ~22 °C) corresponding to 0.084-g CO<sub>2</sub> was desorbed. The theoretical working capacity for these conditions, as determined from vendor-

supplied adsorption isotherms and isobars, is 0.090 g of CO<sub>2</sub>. Therefore, 93% of the theoretical working capacity was measured experimentally. The less-than-maximum working capacity for the device is thought to be due to partial water “poisoning” of the adsorbent. Water is strongly adsorbed on zeolite 13X, and the adsorption device was not heated sufficiently to remove all water before the CO<sub>2</sub> experiment. Nonetheless, this type of experiment demonstrated the ability to cycle rapidly and to effectively utilize the sorbent capacity. It also gave confidence in the use of standard adsorption isotherms as a baseline reference for experimental data and for modeling activities supporting follow-on designs.

### **3.2.2 Multi-Channel, Multi-Cell Adsorber**

The isobaric adsorption process noted above is akin to a purification scheme where the adsorbate gas is stripped from the feed stream to purify it, and subsequently the adsorbed species are exhausted at the same pressure to some reservoir (e.g., Earth atmosphere). For the Mars mission, the need is to increase the CO<sub>2</sub> partial pressure about 125 times above its Mars atmospheric level and provide this stream at an appropriate rate for producing propellants. These goals can be met with multichannel and multi-cell adsorption thermochemical compressors described here.

An advantage of a rapidly cycled multi-cell adsorber is the capability to semi-continuously deliver compressed CO<sub>2</sub> by adsorbing in some cells at the same time previously loaded cells are desorbed. The energy penalty associated with thermal cycling of the cells from cold to hot to cold, etc., is minimized if the mass of structure is reduced and if thermal energy is effectively recuperated from cycle to cycle. Both of these are considerations in the design of the multi-cell adsorber.

One of several proposed modes of operation to attain efficient thermal recuperation in a multi-cell adsorber is depicted in Figure 3.10 (Wegeng et al. 2003). Conceptually, the eight adsorption cells move clockwise through the cycle, while a heat transfer fluid circulates counter-clockwise through heat transfer channels in each cell. (In actuality, the cells may not be physically rotated; rather, virtual rotation can be accomplished with a valve system by transitioning the gas/vapor inlet and outlet points as well as the points where heat is provided to and removed from the system.) The highest temperature occurs in the cell at the top of the diagram where desorption is occurring. As the heat transfer fluid leaves this stage at its hottest temperature, it consecutively gives up heat to the cells on the left that are cycling toward the desorption step. At the bottom, the coldest cell is adsorbing gas or vapor. As the heat transfer fluid moves up through the cells on the right, it cools the cells moving down toward the adsorption step. In this manner, the majority of the heat associated with the thermal mass is effectively recuperated. Any “lost energy” is provided as heat at the hot end before entering the desorbing cell, and the heat transfer fluid is cooled prior to entering the adsorbing cell. A goal is to design, build, and operate a rapidly cycled, multi-cell adsorber that will achieve 80 to 90% thermal recuperation efficiency.

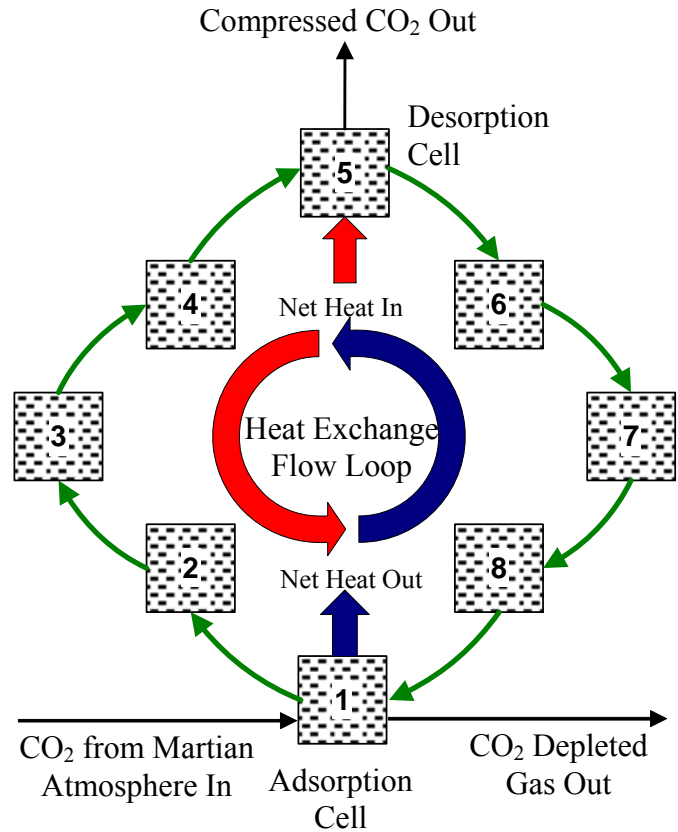


**Figure 3.10.** Schematic of an eight-cell CO<sub>2</sub> sorption pump, with heat recuperation via a heat exchange flow loop.

The adsorbers discussed in Section 3.2.1 were defined as “single-channel” devices because they contained only one adsorbent-filled layer. To increase the CO<sub>2</sub> throughput of the thermochemical compressor while maintaining rapid cycling capability, multiple adsorbent-filled channels effectively coupled with heat-transfer surfaces are needed. Figure 3.11 depicts, in cross-section, one possible design scheme for a multichannel adsorber. The figure shows two adsorbent mesochannels, each adjacent to one heat-exchange fluid microchannel. There is also a gas-flow microchannel placed between the two adsorbent layers. Adsorbate species are transported by diffusive mass transport to or from the adsorbent layers through porous contactors, which preclude the adsorbent from entering the gas-flow channel. During adsorption, for example, a gas stream containing adsorbate species is pumped through the gas-flow channel (normal to the plane of the figure) and adsorbate species diffuse (substantially in the plane of the figure) to the adsorption sites. This flow scheme is “flow-by” instead of the “flow-through” approach which was used for the single-channel adsorbers described above. In the Mars application, particular attention will be paid to pressure drop when feeding gas to the device from the Martian atmosphere. This flow-by mesochannel adsorber system is designed to minimize pressure drop while still providing rapid adsorbate mass transfer. With reference to Figure 3.11, note that a flow-through device can be readily created by removing the gas-flow channel and the porous contactors.

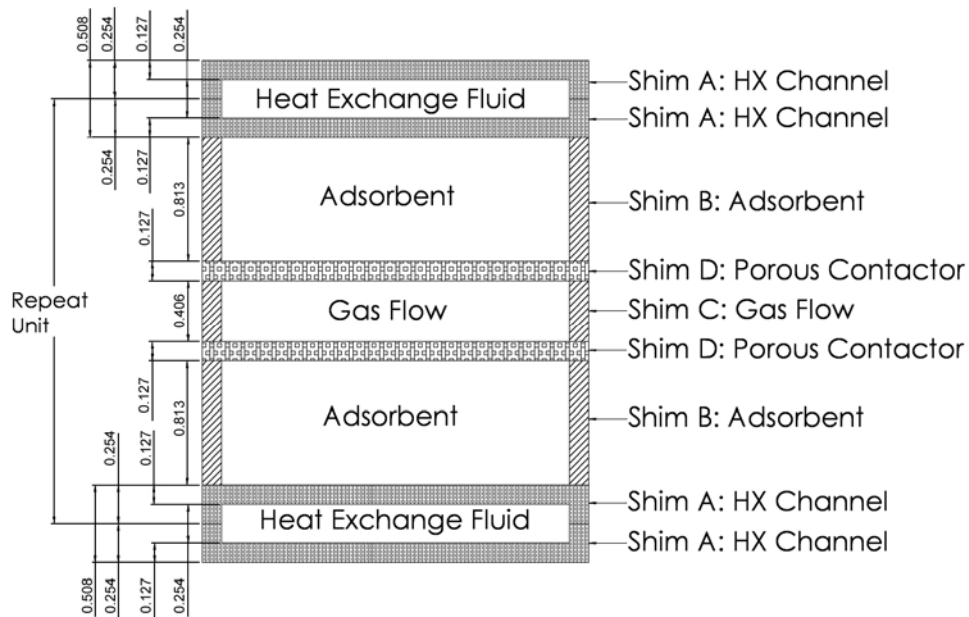


**Figure 3.11.** An arrangement of four unique shim types defines heat-exchange fluid, gas flow, and adsorbent channels within a single repeat unit of a flow-by adsorber (sample dimensions are in millimeters). A flow-through adsorber arrangement is obtained by removing shims C and D.

The channels of Figure 3.11 are defined by a specific arrangement of four unique laminates, or shims: a pair of shims (A) establishes a heat-exchange microchannel; each Shim B creates an adsorbent mesochannel; Shim C provides the gas-flow channel; and each Shim D is a porous contactor allowing diffusive mass transport between the adsorbent and gas-flow channels. Seven shims, two each of A, B, and D and one of C, create a repeat unit. Figure 3.12 shows plan views of the four shim designs for an eight-cell flow-by adsorber of octagonal symmetry; some details of the heat-exchange and porous contactor shims (A and D) are not completely represented in the figure. The two triangular cutouts within each of the trapezoidal octants of the shims form the heat-exchange fluid header and footer for the cell. Machine-ready shim drawings created in preparation to fabricate a laboratory-scale test device (i.e., one-eighth scale of the Mars direct sample-return mission) are proprietary but can be provided to NASA upon request.

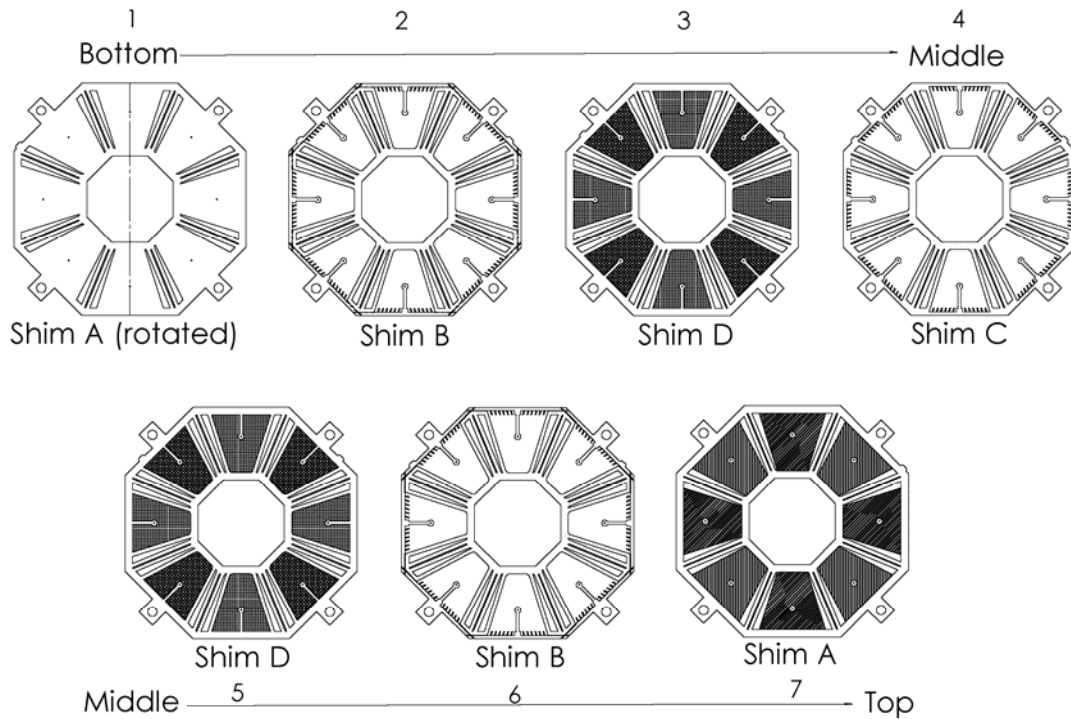


**Figure 3.12.** Plan view of shims in a repeat unit demonstrating the octagonal symmetry of an eight-cell adsorber.

The processing capacity of a device is increased by stacking more repeat units to increase the number of adsorbent channels with no penalty in heat and mass-transport efficiency. Figure 3.13 shows the stacking arrangement for an eight-cell adsorber consisting of twelve repeat units. Perhaps more obvious with reference to Figure 3.11, one extra heat-exchange channel is needed at each end of the stack to provide heat exchange for every adsorption channel. Thick end plates, shown in Figure 3.13, provide structural stability in the diffusion bonding process and are used to create external header and footer connections for the heat-exchange fluid. After bonding and some machining, the structure of Figure 3.13 is converted to the eight-cell adsorber shown in Figure 3.14. Removing a significant fraction of the material from the end plates after bonding reduces the device mass and the heating and cooling duty associated with that mass during thermal cycles. The latter is especially important if the end plate material is thermally conductive and has a large heat capacity. To further minimize the “thermal mass” of the adsorber and to maintain the ruggedness provided by bonded metal necessary for space travel, the project planned to fabricate and test an adsorber like Figure 3.14 in titanium. Titanium has roughly half the density and about half the volumetric heat capacity of stainless steel.

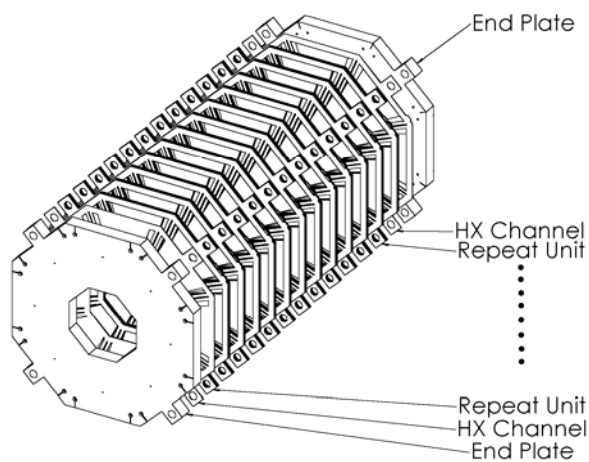


**Figure 3.13.** An exploded view of multiple repeat units, capping heat-exchange shims, and endplates arranged for bonding.

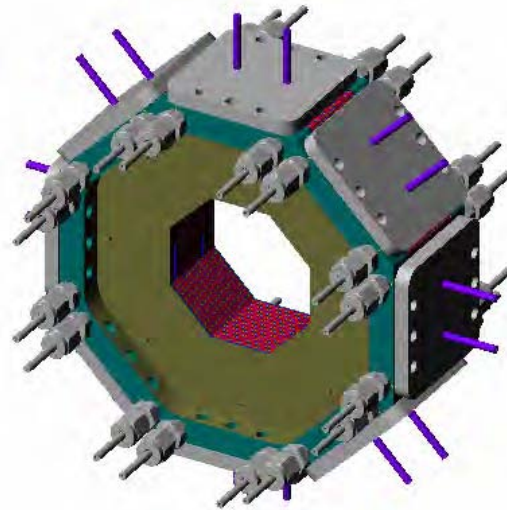


**Figure 3.14.** A completed adsorber with tube stubs for external adsorbate gas and heat-exchange fluid connections.

The eight-cell adsorber shown in Figure 3.14 is designed for a rapidly cycled TSA process with thermal recuperation using the mode of operation depicted in Figure 3.10 by proper linking and control of the heat-exchange fluid streams. The amount of heat that must be added to the desorber and removed from the adsorber from external sources is a function of the thermal recuperation efficiency and the heats of sorption. Since adsorption is typically exothermic and desorption is endothermic, energy must be removed or added from the adsorbent to affect the sorption cycle. These heats of sorption are the minimum thermodynamic energy cost to compress gas thermochemically in a heat-engine cycle.

Figure 3.14 is a model of the laboratory-scale CO<sub>2</sub> thermochemical compressor designed for the NASA ISPP project. The plates on each of the eight cells are the header/footer ports for the fluid stream containing the adsorbate gas. In the case of collecting and compressing CO<sub>2</sub> on Mars, Martian atmospheric gas is introduced into the cooled adsorption cell(s) through these ports. After isolating cells from the Martian atmosphere, the cells are heated, gas is desorbed from the adsorbent, and the CO<sub>2</sub> partial pressure within the gas phase of the sealed cells increases. When the temperature nears or is at the maximum desorption operating temperature for the system, the ports on the desorption cell(s) are opened to provide compressed CO<sub>2</sub> at a specified throughput and pressure to the microchannel reactors for propellant production.

A computational tool was created in a Microsoft<sup>®</sup> Excel<sup>®</sup> spreadsheet to aid in the design and sizing of multi-cell adsorbers operated in this manner. The tool is an equilibrium-based model developed to assess theoretical adsorbate (e.g., CO<sub>2</sub>) throughput rates, compression factors, and thermal energy requirements as a function of adsorbent type and mass, feed stream composition (binary assumed, only one species adsorbed), cycle frequency, and adsorption and desorption operating temperature limits. The model also accounts for the mass and volume of the sorption pump structure, which are dependent on design geometry factors and materials of construction

(e.g., titanium or stainless steel). Adsorption isotherms, which provide information on the specific capacity of adsorbate as a function of its partial pressure at a given temperature, are key elements of the model. Isotherm data for CO<sub>2</sub> adsorption on zeolite 13X obtained from vendor literature were fit to Langmuir-Freundlich isotherm. The Langmuir-Freundlich model for adsorbent loading capacity is given by

$$x = \frac{aP^b}{(1 + cP^b)} \quad (3.1)$$

Where  $a$ ,  $b$ , and  $c$  are fit coefficients, and  $P$  is the partial pressure of the adsorbed species in the gas phase. The adsorbent loading,  $x$ , is given as the mass of sorbed species per 100 masses of adsorbent (e.g., kg CO<sub>2</sub>/100 kg zeolite 13X). The Langmuir-Freundlich coefficients obtained by fitting adsorption isotherm data for CO<sub>2</sub> on zeolite 13X are shown in Table 3.1 for temperatures ranging from -50 to 200°C.

**Table 3.1.** Langmuir-Freundlich Isotherm Fit Parameters for CO<sub>2</sub> Adsorption on Zeolite 13X for CO<sub>2</sub> Partial Pressures in kPa

Temp.	200 °C	100 °C	80 °C	25 °C	20 °C	0 °C	-25 °C	-50 °C
$a$ coef	0.026514	1.2626	2.3434	8.8621	9.8497	14.728	23.239	35.857
$b$ coef	1.1898	0.73171	0.62611	0.45702	0.4487	0.38383	0.33145	0.28735
$c$ coef	0.0019142	0.060019	0.093506	0.28352	0.31282	0.42256	0.61988	0.90112

Using the spreadsheet computational model, it was determined that 12 repeat units (Figure 3.11) were needed in the proposed laboratory test unit shown in Figures 3.13 and 3.14 to produce ~0.1 kg-CO<sub>2</sub>/hr using commercially available zeolite 13X with minimum adsorption and maximum desorption operating temperatures of 0 and 100°C and a two-minute cycle time. The CO<sub>2</sub> production rate is one-eighth that required for a Mars robotic sample-return mission. Further, the target CO<sub>2</sub> compression ratio of 10x (100 kPa CO<sub>2</sub> product:10 kPa CO<sub>2</sub> feed) for the laboratory system is only ~one-eighth that needed to compress CO<sub>2</sub> on the Martian atmosphere at 0.8 kPa to the 100 kPa proposed for CH<sub>4</sub> propellant production in microchannel reactors.

Two main strategies are considered to increase the CO<sub>2</sub> compression ratio. All else being constant, expanding the temperature difference between adsorption and desorption will typically increase the compression ratio. This is demonstrated in Figure 3.15, where the performance of model adsorption units operating between two temperature ranges (0 and 100°C; and -50 and 100°C) and scaled to produce ~0.81 kg-CO<sub>2</sub>/hr for the Mars direct sample-return mission are compared. The figure shows the specific productivity, defined as mass CO<sub>2</sub> throughput per minute per unit hardware mass, as a function of compression ratio. The hardware mass consists of the bonded metal adsorption unit including integral heat-exchange channels, all header and end plates, and the mass of zeolite 13X filling the adsorbent channels. For comparison, the desorption pressure (and thus the compression ratio) was varied and the corresponding CO<sub>2</sub> throughput rate was determined. Figure 3.15 shows that an adsorber operating over a larger temperature range (-50 to 100°C) could compress CO<sub>2</sub> by a factor of 125 in a single stage, whereas this is not possible using a 0 to 100°C operating window.

The benefit of using titanium instead of stainless steel in the compressor structure is also shown in Figure 3.15. The amount of adsorbent required is independent of the adsorber structure material for a given design and an adsorption/desorption operating temperature range. Therefore, differences in specific productivity at a given  $T_{ads}$  and  $T_{des}$  reflect differences in the structure mass for the titanium and stainless steel units. The specific productivity is superior in the titanium devices because the density of stainless steel is  $\sim 1.8$  times greater than titanium and the hardware mass is dominated by the metal structure.

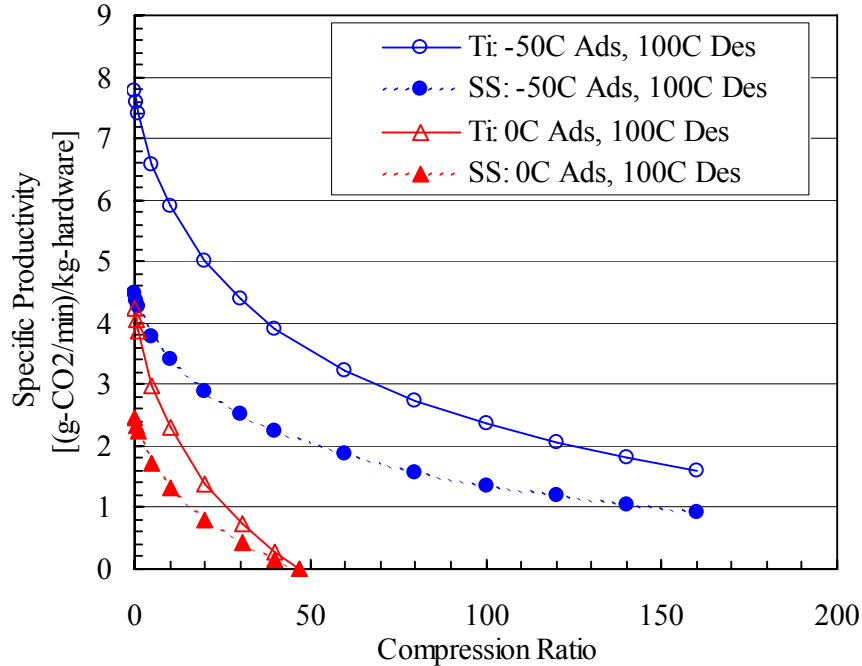


**Figure 3.15.** The specific productivity of titanium and stainless steel adsorbers as a function of compression ratio ( $P_{CO_2 Des} / P_{CO_2 Ads}$ ) for two adsorption/desorption operating temperature ranges. Assumptions: 95%  $CO_2$  feed at 0.8-kPa (6-torr) partial pressure; zeolite-13X adsorbent; 90% sorbent capacity utilization efficiency.

Operating multiple sorption thermochemical compressor stages in series with each stage being a multi-cell adsorber like the one shown Figure 3.14, is another means to increase the compression ratio for a fixed temperature range. Model results indicate, as expected, that operating a large number of stages in series reduces the overall amount of adsorbent needed to produce a compressed adsorbate stream at a specified rate and compression ratio. Practical considerations such as hardware complexity and mass limit the number of beneficial stages to small finite numbers. Currently, a two-stage mesochannel adsorption thermochemical compressor system appears optimized to produce  $CO_2$  for the Mars robotic sample-return mission.

Figure 3.16 shows the calculated specific productivity of a two-stage compressor designed to produce 0.81-kg  $CO_2/hr$  for ISPP during a Mars robotic sample-return mission using adsorption and desorption temperatures of -50 and 100 °C, respectively. The specific productivity is assessed as a function of the inter-stage  $CO_2$  partial pressure, the  $CO_2$  concentration delivered from the stage 1 desorption cell to the stage 2 adsorption cell. In the stage-1 analysis, the

adsorption unit is scaled to compress the required amount of CO<sub>2</sub> from 0.8 kPa (6 mm Hg) to the inter-stage pressure. Likewise, the stage 2 unit is designed to compress CO<sub>2</sub> from the inter-stage pressure to the target delivery pressure 100 kPa (750 mm Hg). As the inter-stage pressure increases, the specific productivity of stage-1 adsorbers decreases while the specific productivity of stage-2 units increases. The combined (net) specific productivity of a two-stage system is optimized at an intermediate inter-stage pressure corresponding to the intersection of the stage-1 and stage-2 operating curves. The optimum inter-stage pressure is near 12.8 kPa (96 mm Hg) and the specific productivity of the system is ~1.84-g CO<sub>2</sub>/min/kg hardware (half the value of each individual stage). The optimum (i.e., minimum total hardware mass) results when each stage is the same size. For a smaller operating temperature range (0 to 100 °C), a similar analysis indicates that the optimum inter-stage pressure is 10.8 kPa (81 mm Hg) and the specific productivity of the system is ~0.75-g CO<sub>2</sub>/min/kg hardware.

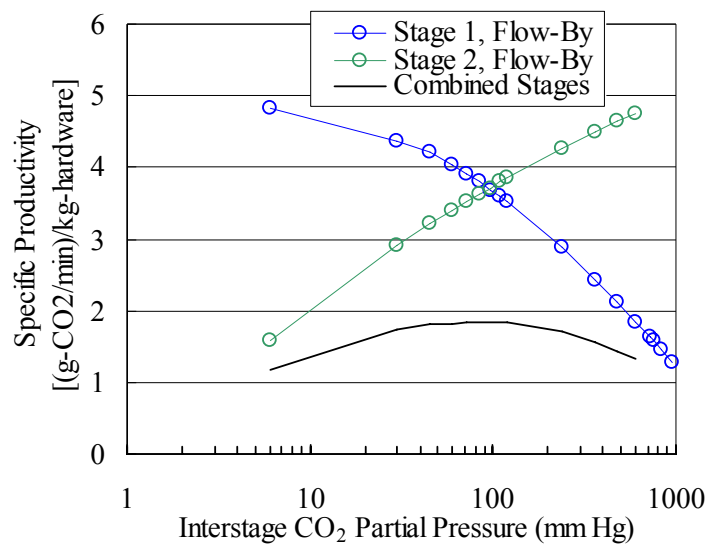


**Figure 3.16.** Operational characteristics of a two-stage rapidly cycled mesochannel adsorption system operating between -50 °C and 100 °C and designed to produce 0.81-kg CO<sub>2</sub>/hr for ISPP during a Mars robotic sample-return mission. Assumptions: titanium structure; zeolite-13X adsorbent; 95% CO<sub>2</sub> feed at 0.8-kPa (6-mm Hg) partial pressure to stage 1; delivery of CO<sub>2</sub> at 100 kPa (750 mm Hg) from stage 2; 90% sorbent capacity utilization efficiency; 2-min cycle time.

In the case of a 0 and 100 °C operating range, two stages are necessary to achieve a specified 125x CO<sub>2</sub> compression. With the -50 to 100 °C range, it is possible to compress fully in a single stage (e.g., see the stage 2 curve of Figure 3.16 at a 6-mm Hg inter-stage pressure). However, the specific productivity of single stage compression (~1.58-g CO<sub>2</sub>/min/kg hardware) is lower than the two-stage system (~1.84-g CO<sub>2</sub>/min/kg hardware) operated with the same temperature limits. A similar analysis using 0 and 200 °C temperature limits indicates that a single stage is more productive than any combination of two stages. Multiple stages are not always advantageous.

Table 3.2 summarizes the specific productivity and masses of titanium structure, adsorbent, and total compressor hardware (structure + adsorbent) of single -and two-stage systems operated over the three temperature ranges and using other operating conditions discussed above for the Mars direct sample-return mission. Note that a bigger temperature range is not always advantageous. The specific productivity of a two-stage system operating at -50 to 100 °C is greater than the best system operating between 0 to 200 °C. This is a result of greater change in the adsorbent loading capacity with temperature at low temperatures (e.g., <0 °C) than at high temperatures (e.g., >100 °C).

**Table 3.2.** Summary of calculated titanium mesochannel CO<sub>2</sub> adsorber characteristics to produce compressed CO<sub>2</sub> for a Mars direct sample-return mission.

<b>Operation Mode</b>	<b>Specific Productivity (g CO<sub>2</sub>/min/kg hardware)</b>	<b>Total Hardware Mass (kg)</b>	<b>Structure Mass (kg)</b>	<b>Adsorbent Mass (kg)</b>
2 Stages; 0 to 100 °C	0.75	18.3	16.9	1.4
1 Stage; -50 to 100 °C	1.58	8.59	7.94	0.65
2 Stages; -50 to 100 °C	1.84	7.35	6.86	0.49
1 Stage; 0 to 200 °C	1.76	7.72	7.14	0.58
2 Stages; 0 to 200 °C	1.70	8.01	7.47	0.54

Reductions in structure mass and corresponding increases in specific productivity may be attained with future design improvements. Performance enhancement might also be achieved with shorter cycle times or alternative operating scenarios (compared to that shown in Figure 3.10) that could boost CO<sub>2</sub> throughput per unit adsorbent mass. One relatively simple improvement might be to use a flow-by device in stage 1, where pressure drop during gas feed from the Martian atmosphere to the adsorption cell is an issue, and use a flow-through device in stage 2 (which is fed with gas compressed in stage 1). The results shown in Figures 3.15 and 3.16 and Table 3.2 all assumed a flow-by architecture – mass is reduced in a flow-through device because the gas flow channel and porous contactor shims (Figures 3.11 and 3.12) are not required. Mass savings of >25% are possible when using a flow-through microchannel adsorber.

## 4.0 Reactor Subsystem

To produce O<sub>2</sub> and CH<sub>4</sub> at the 3.8 mass ratio required for efficient propulsion-system operation, a system that combines the Sabatier and RWGS reactions was selected. In the case of the Sabatier reactor, CO<sub>2</sub> is combined with H<sub>2</sub> to form CH<sub>4</sub> and H<sub>2</sub>O in the exothermic ( $\Delta H_r = -165$  kJ/mol) and self-sustaining reaction. In the case of the RWGS reaction, CO<sub>2</sub> is combined with H<sub>2</sub> to produce H<sub>2</sub>O and CO in an endothermic, non-equilibrium catalytic reaction ( $\Delta H_r = +37.2$  kJ/mole).

As with all the subsystems in the ISPP, minimizing the size and weight of the reactors is essential. Maximizing the activity of catalyst and obtaining high CO<sub>2</sub> conversion can help accomplish this. High CO<sub>2</sub> conversion is only possible by controlling the temperature. Since the SR is exothermic, and the RWGS is endothermic, under adiabatic conditions, as the reaction progresses, the SR reaction temperature rises and the RWGS reaction temperature falls. In both cases, thermodynamic equilibrium conversion is reduced. Using microchannel architecture, the temperature of these reactions can be controlled to improve conversion and reduce the resultant reactor sizing.

### 4.1 Experimental Approach

The purpose of the reactor development task is to develop a compact reaction system, incorporating microchannel catalytic reactors and heat exchanges for the RWGS and Sabatier process reactions. The approach taken in this development includes catalyst development, reactor design and fabrication, and reactor testing.

The first stage in the development of a catalytic reactor is the development of a catalyst material. As part of an agreement between Battelle Memorial Institute (BMI) and NASA, the catalysts developed by BMI would remain proprietary to Battelle. Catalyst composition would not be provided to the reactor development task or to NASA. Instead, a set of criteria was provided to the BMI catalyst development team as shown in Table 4.1. They were to develop catalysts that met the criteria provided. Testing was performed using a powdered catalyst first and then the most promising materials were tested on an engineer form of catalyst in a single channel reactor. The BMI catalyst development task then provided catalyst data results and enough engineered catalyst to fill the reactors.

**Table 4.1.** Catalyst Target Performance Criteria Provided to the BMI Catalyst Development Team

RWGS Catalyst Target Criteria	Sabatier Catalyst Target Criteria
35–45% conversion	>85% conversion
95% selectivity to CO	>95% selectivity to CH <sub>4</sub>
Residence time $\leq 25$ ms	Residence times $\leq 100$ ms

The data provided for the single channel reactors were then used to assist in the design of a multichannel reactor. Based on the residence time, for a given conversion and selectivity, the reactor size could be determined. By using the thermodynamics, the amount of heat rejection or

addition can be determined and designed for. Finally, with the operating temperature and pressure, the materials of construction and thickness could be determined.

All the reactors developed under this project were designed based on sheet architecture. Headers, microchannels, and heating passages were fabricated from thin metal shims using photochemical machining. The shims were then diffusion bonded to create a single monolith. The device was completed using conventional machining to remove excess material and to expose slots for inserting the catalyst. After the catalyst was loaded into the reactor, the reactor was sealed and the feed and product tubing welded between the reactor and heat exchangers.

Once the reactor was fabricated, testing was performed over a range of temperatures, stoichiometric ratios ( $H_2/CO_2$ ), and contact times<sup>1</sup>. The dependent and independent variables are shown in Table 4.2 below. Operating the reactors at sub-ambient pressure was not possible. To simulate the effect of lower partial pressures of hydrogen, carbon dioxide, various ratios of  $N_2$  to reactive gas were evaluated. Following initial testing, alternative approaches were used in an attempt to improve the reactor performance. For the RWGS reactor, a second stage was added and water was condensed between the two stages. For the Sabatier reactor, the temperature down the length of the reactor was adjusted. For the combined system, a variety of temperature distribution and flow combinations were investigated.

**Table 4.2.** Variables Investigated in Catalyst Testing

Dependent Variables	Independent Variables
Reactor Temperature (inlet or outlet) Contact Time $H_2:CO_2$ Ratio $N_2$ :Reactive Gases Ratio	System Pressure Feed & Product Gas Composition (GC: $H_2$ , $CO$ , $CO_2$ , $N_2$ , $O_2$ , $CH_4$ ) Weigh of Water Generated Uncontrolled Temperatures (Within the reactor & between reactor and heat exchangers)

Based on the results of the testing, models were developed to fit the conversion and selectivity results obtained. These models provide an understanding of the data and can provide a means of interpolating between data points. They can also be used to in an overall process size and weight optimization routine.

A generic layout of the equipment design for all three reactor systems is shown in Figure 4.1. Hydrogen, carbon dioxide and nitrogen are fed through MKS mass flow controllers to a microchannel recuperative heat exchanger. This ~90% effective heat exchanger uses heat from the product gases to preheat the reactants to near reacting temperature. The gases then react with catalysts within the reactor. In the case of exothermic reactions, the heat of reaction is removed by flowing nitrogen or air through interleaved microchannels. Cartridge heaters were used to supply the initial heat and maintain the reaction temperature. Product gases then pass back through the recuperative heat exchanger and into a condenser operated at  $\sim 4^\circ C$  to remove and collect the water generated. To further remove the water before going into the gas chromatograph, a PermaPure<sup>®</sup> gas diffusion drier is used. The gases were then analyzed with a

<sup>1</sup> Contact Time = Empty Reactor Volume/Reactant Flow at STP

dual column Agilent MicroGC with Poraplot U and Molesieve column using a thermal conductivity detector.

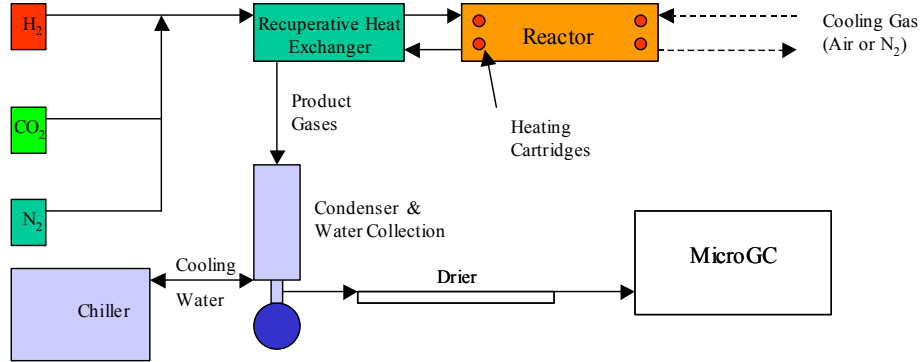


**Figure 4.1.** Generic Equipment Layout for RWGS & SR Reactor Testing

The models used to fit the experimental data obtained were developed based on a plug flow reactor operating at steady-state:

$$V = F_{CO_2}^0 \int_0^X \frac{dX}{-r_{CO_2}} \quad (4.1)$$

where

- V = the reactor volume
- $F_{CO_2}^0$  = the initial molar flow rate
- X = the conversion
- $r_{CO_2}$  = the reaction rate.

Pressure is assumed constant and the temperature is assumed to be either constant or of a known profile down the length of the reactor. For the work done here the reaction rate is assumed to be a reversible reaction based on the Langmuir-Hinshelwood kinetics of the following form:

$$r_{CO_2} = \frac{k \left( P_{CO_2} P_{H_2} - \frac{P_{H_2O} P_{CH_4 \text{ or } CO}}{K_{eq}} \right)}{(1 + k_1 P_{CO_2} + k_2 P_{H_2} + k_3 P_{CO})^n} \quad (4.2)$$

where

- k = the Arrhenius rate constant of the form  $Ae^{-E_a/RT}$  ( $E_a$  being the activation energy)
- $K_{eq}$  = the temperature dependent equilibrium constant
- $P_x$  = the partial pressures of reactants and products
- $k_{1,2,3,\dots}$  = constants associated with adsorption on the surface of the catalyst.

By minimizing the difference between experimental data and the model for a set of experimental data, the adsorption constants, activation energy ( $E_a$ ) and Arrhenius factor can be calculated. To account for both conversion and selectivity of a given catalyst system, the reaction rate of both the SR and RWGS were modeled with reaction rate expressions and then selectivity was calculated as the ratio of the conversion of methane to carbon monoxide.

Three reactors were studied in the course of this work: the RWGS, Sabatier, and a combined RWGS/Sabatier reactor. Each of these reactors will be discussed in the sections below.

## 4.2 RWGS Reactor Study

The BMI catalyst team developed a catalyst for RWGS and provided initial single channel data with the engineered form as shown in Figure 4.2. During this work, the experimental configuration for their single channel testing could not be adequately sealed. Thus, the BMI experimentalist believed that significant flow bypass occurred in the data presented and that conversion could be much higher with a multichannel device that is properly sealed. During the design of the reactor, the conversions for these data were escalated slightly to account for possible leaking.

The RWGS reactor was designed to 1) provide a simple means of heat to the reactants and 2) provide a modular design with easy scale-up and/or turn-down. The RWGS reactor was designed based on single channel tests to be one half scale for the Direct Robotic Return Mission Scenario. This equates to a 100 g/hr water production. The design of the reactor shims is shown in Figure 4.3. There are four reactors within a single reactor monolith. Thirty of each of these shims plus a top and bottom plate were diffusion bonded together making it a 2.54 cm thick monolith weighing approximately 500 grams. Each of the four reactors can be operated individually to affect turn-down, or additional reactors can be added to scale-up the process.

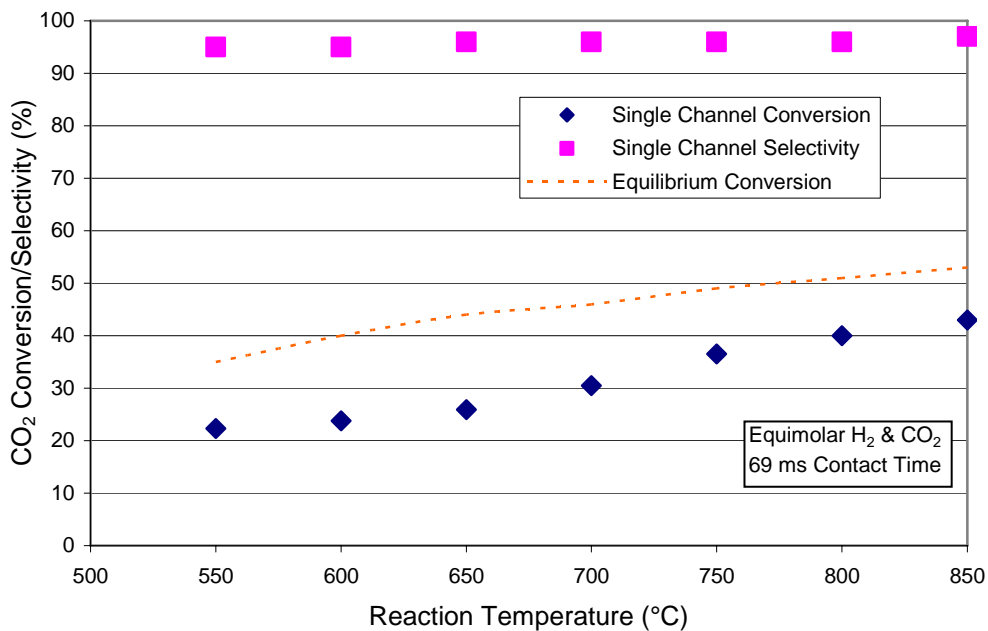


**Figure 4.2.** Single channel testing of the RWGS engineered catalyst at 35 ms residence time and stoichiometric conditions.

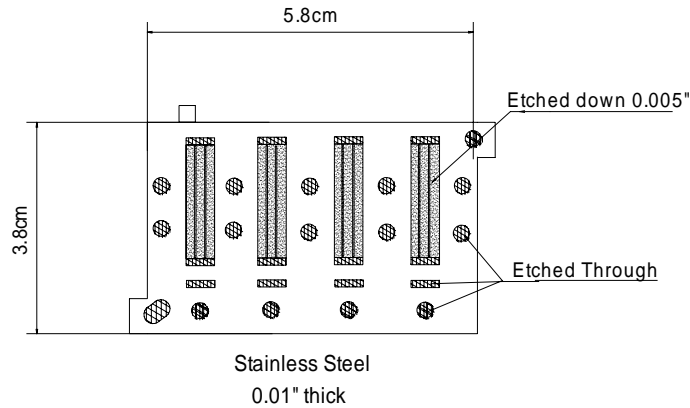


**Figure 4.3.** One of the three shims used to fabricate the RWGS reactor. In this shim, the cross-hatched areas are etched completely through and the shaded areas are etched halfway through the metal. In the second shim (the spacer shim) the cross-hatched and shaded areas are etched completely through the metal. The spacer shim is placed on top of the flow distributor shim to create the necessary volume for the catalyst. The mirror image of the pictured shim is then placed over the top of the other two shims to create a single open microchannel. A series of shims are diffusion bonded together to form a monolith.

There are fourteen 1/8" diameter rod heaters that were placed along the top and sides of the reactor channels. These rods pass all the way through the reactor and can be heated up to 800°C. The reactant gases enter through the lower slots. These slots allow the gases to be heated from ~600°C out of the recuperator to 750°C before they enter the reactor section. The catalyst sits in a section 2 cm long and 0.5 cm wide. Gases will come up through the bottom of the reactor and into a rectangular header and are distributed to the catalyst. Gases will then exit through the bottom of the reactor and enter the recuperator. One recuperative heat exchanger will be used for each of the four sets of reaction channels. Heat is conducted from the heater cartridges through the stainless steel and along the fins between the catalyst channels. Since each of these sets of microchannels is symmetric, only one of them was tested during these operations. A photograph of the completed unit is shown in Figure 4.4.



**Figure 4.4.** Photograph of the completed RWGS reactor. This unit was designed to be half scale for the direct robotic return mission.

The reaction temperature was measured with a thermocouple based on the product gas-temperature outlet. The temperature of the gases passing through the heating channel within the reactor block were also measured and found to be within 10°C of the product gases. No temperature measurements were made in the microchannels themselves. For the sake of simplicity, the reaction was operated near atmospheric pressure. The operating pressure of the reactor ranged from 130 to 180 kPa.

Figure 4.5 illustrates CO<sub>2</sub> conversion as a function of temperature and contact time for the multichannel RWGS reactor. Equilibrium conversion and selectivity are also shown. As would be expected, the conversion increases with temperature and decreases with contact time. It should be noted that the conversions for the multichannel reactor are higher than similar conditions with the single channel reactor. This is probably due to the bypass experienced in the single channel unit.

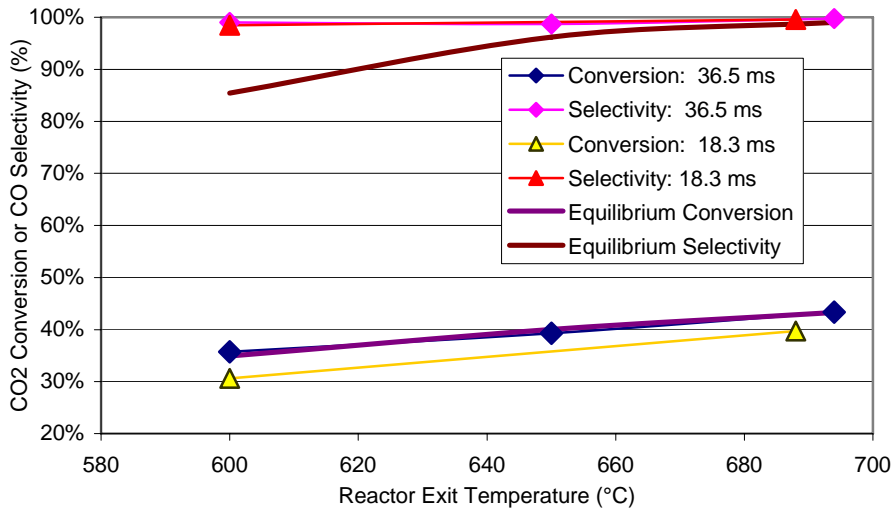


**Figure 4.5.** RWGS reaction CO<sub>2</sub> conversion and CO selectivity at H<sub>2</sub>/CO<sub>2</sub> ratio= 1 and contact times of 18.3 ms and 36.5 ms.

The reactor operation also meets the target performance criteria shown in Table 4.1. At the design condition of 36-ms contact time, the reactor outlet reached equilibrium conditions over the range of temperatures studied here. By doubling the flow rate (to 18-ms contact time), the overall reactor is large enough to support the entire sample-return mission, but there is a slight decrease in conversion.

Due to thermodynamic equilibrium, the conversions are constrained to fairly low levels. Figure 4.6 illustrates that increasing the concentration of hydrogen results in increasing the conversion of CO<sub>2</sub> beyond that attainable at a 1:1 ratio of H<sub>2</sub> and CO<sub>2</sub>. However, at higher H<sub>2</sub>:CO<sub>2</sub> ratios, more total gas must be purified and compressed downstream of the reactors to recycle the added hydrogen used during the reaction step. Once the sensitivity of the hydrogen recovery and recycle step with flow rate is better quantified, the H<sub>2</sub>/CO<sub>2</sub> ratio can be defined to minimize the overall process size.

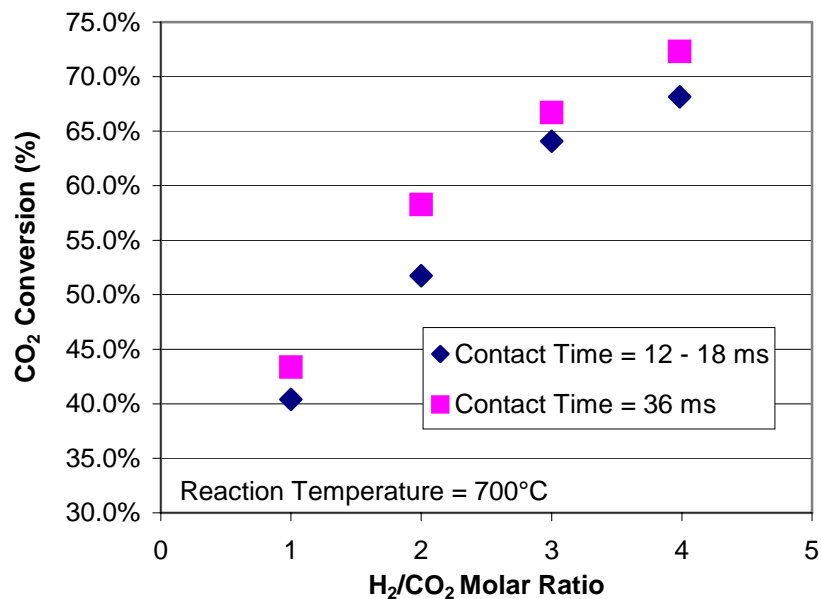


**Figure 4.6.** RWGS reaction CO<sub>2</sub> conversion varying H<sub>2</sub>/CO<sub>2</sub> ratio and contact times at a reactor outlet temperature of 700°C.

If the purification system increases at a faster rate than the reactor system when hydrogen flow rates are increased, another approach may be necessary to increase the conversion beyond equilibrium. One approach that was tested successfully is to use two stages of RWGS reactions with a water-separation step between. By removing the water after the first stage of the reaction, the equilibrium conversion of CO<sub>2</sub> can be shifted further towards CO. For the experiment performed, the product from one set of reaction channels was cooled to ~8°C and the water collected. These gases were then reheated to the original reaction temperature and sent into a second set of reaction channels. To minimize heat requirements, a recuperative heat exchanger was used for both sets of reactions. The results of this approach as compared to predictions are shown in Figure 4.7. The figure shows an increase of approximately 15% in overall conversion by removing the water and reprocessing the reactor products. Furthermore, the conversion obtained is very similar to that predicted by thermodynamic equilibrium.

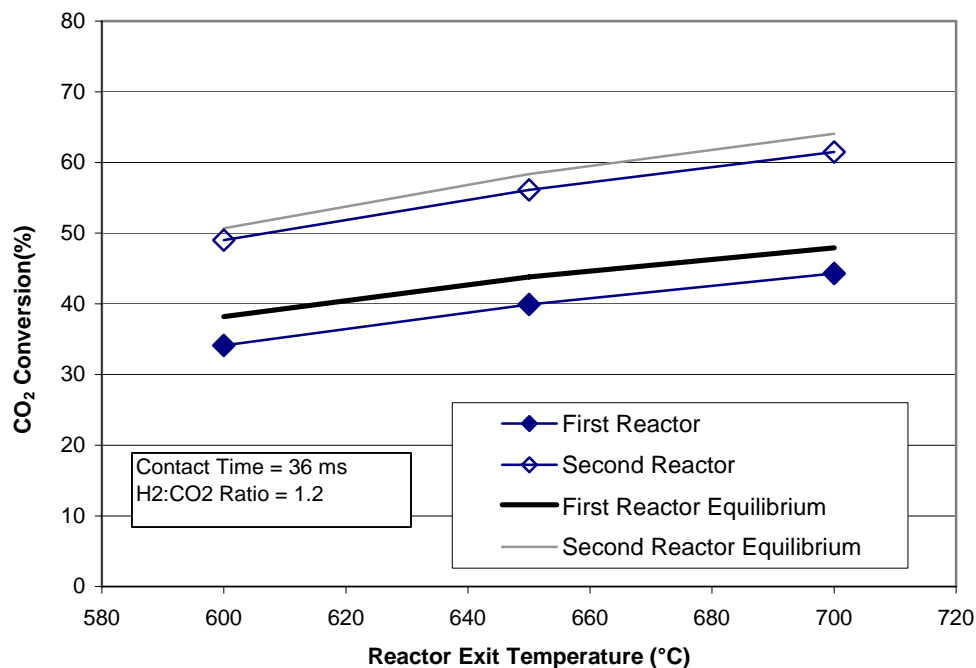


**Figure 4.7.** Conversion and selectivity for two RWGS reactors in series removing the water between to increase conversion. Both reactors are at the same temperature. Experimental results are compared to thermodynamic equilibrium.

### 4.3 Sabatier Reactor Study

The BMI catalyst team developed a catalyst for SR based on the specification for high conversion and selectivity and a reasonably short contact time. Initial single channel data with the engineered form of the catalyst is provided in Figure 4.9. Three catalyst compositions were tested with an engineered form of the catalyst. Based on the results provided, none of the catalyst compositions met the original conversion criteria in Table 4.1. However, the highest conversions were possible with the catalyst generically labeled “C2” and this catalyst was selected for further study in the multichannel reactor. Testing as to the stability and longevity were not addressed and became difficulties in future testing.

As can be seen from the equilibrium data in Figure 4.8, this reaction reaches high conversions at reduced temperatures. However, the kinetics of the reaction become very slow at these lower temperatures, resulting in increased contact time. The net result is a large reactor. At higher temperatures, conversion decreases and CO begins to form as a byproduct. In an effort to improve conversions, the Sabatier reactants could be preheated to between 450 and 500°C prior to the reactor using a microchannel heat exchanger. At these temperatures, fast kinetics will result in the majority of the conversion occurring in a short residence time. As the gases react, they could then be cooled using the counter-current flow of coolant where the final product will exit with nearly complete conversion found at these lower temperatures. Because the Sabatier reaction is exothermic, both heat of reaction and sensible heat must be removed down the length of the reactor to create this profile.

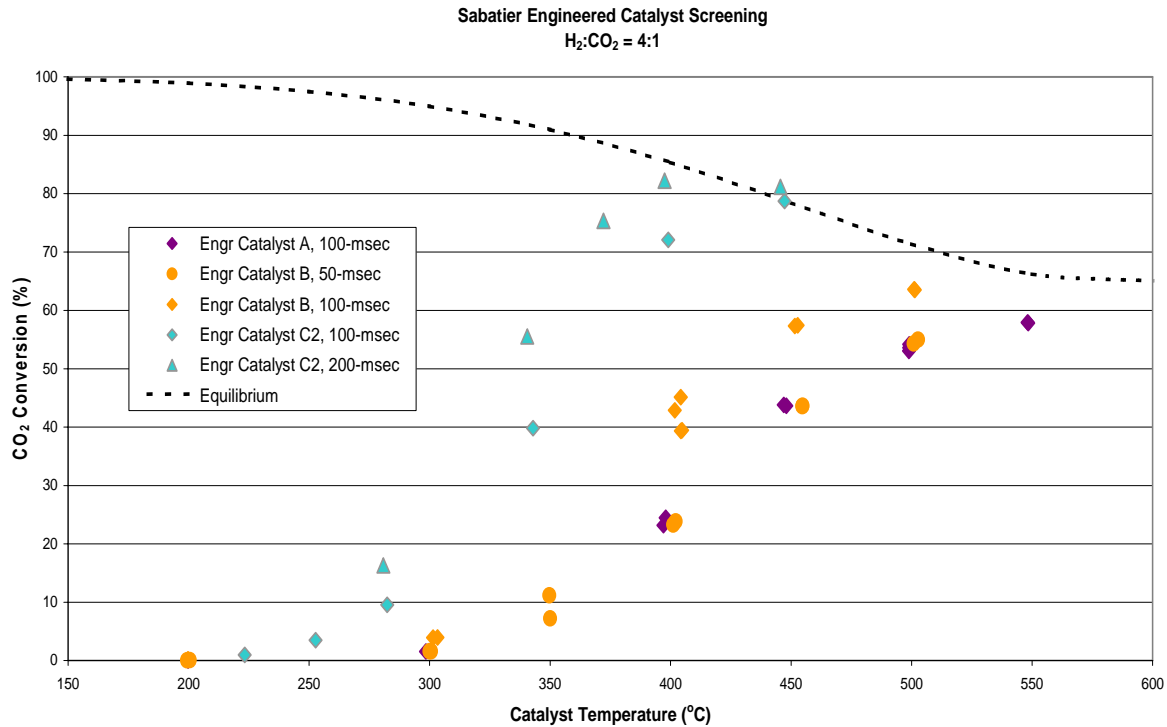


**Figure 4.8.** Results of the engineered Sabatier Reaction catalyst in a single channel reactor.

During the design, another approach was developed that would combine the RWGS and SR into a single system. Since the RWGS reaction is endothermic and the SR is exothermic, the energy from one system could be transferred to the other. Interleaving the catalyst materials and operating in a counter-current flow mode would cool the SR catalyst as it moved down the reactor by adding heat to the endothermic RWGS reaction. The RWGS reaction gases in turn would be heated as they moved down the channel by the exothermic SR. In both cases reaction conversion would be improved. Additionally this approach would minimize the cooling required for the SR and the heating required for the RWGS, reducing the total energy consumption. The ability to operate with SR only, RWGS only, or both reactions run simultaneously was incorporated into the design.

The single channel results and equilibrium data were used to develop a design for the Sabatier reactor. Because of the longer contact time as compared to the RWGS, the SR reactor was designed for 1/8<sup>th</sup> of the scale required for the Robotic Sample-Return Mission Scenario. This equates to 12 g/hr CH<sub>4</sub> and 24 g/hr H<sub>2</sub>O.

The SR was designed as a combined reactor/heat exchanger. To create the temperature profile needed, conduction down the length of the reactor must be minimized. This was done by producing a long, thin reactor design with temperature control on each end. The temperature profile would then be created based on the temperature set at each end. To heat the inlet and outlet, 2 cartridge heaters can be inserted into each end. In the case that cooling is required, cold gas can be passed down the microchannels that are interleaved with the reaction channels. One of three shims used to produce this design is shown in Figure 4.9. To minimize the number of

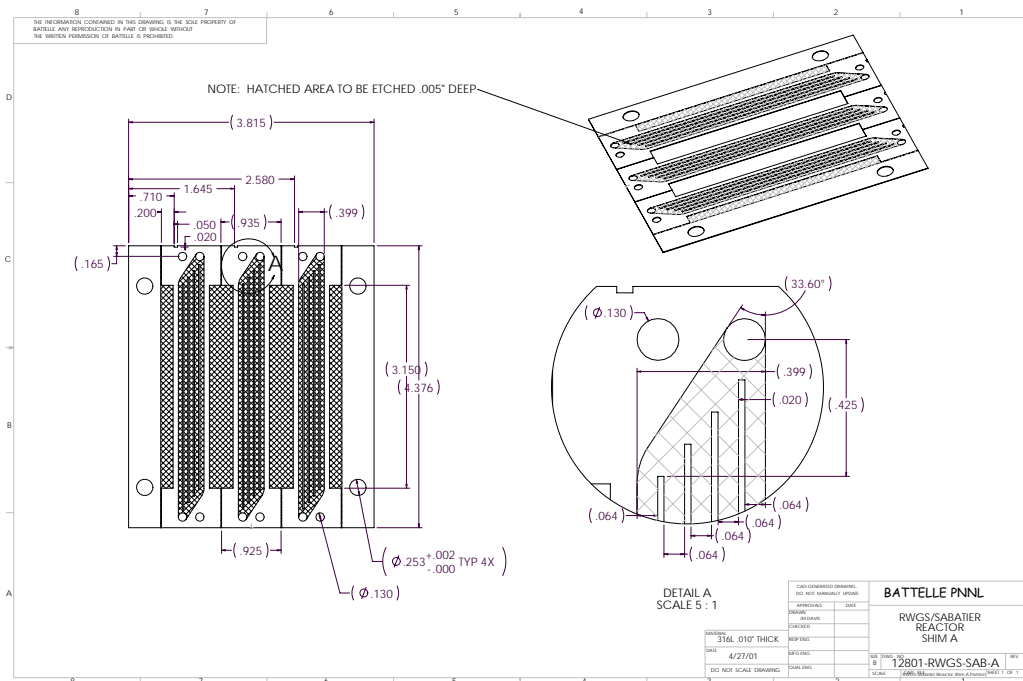


**Figure 4.9.** Flow Distributor Shim from the Sabatier Reactor. The cross-hatched areas are etched part way through the metal. A second shim (the spacer shim) with the cross-hatched area etched completely through the metal is placed on top of the flow distributor shim to create the necessary volume for the catalyst. The mirror image of the pictured shim is then placed over the top of the other two shims to create a single open microchannel. Sets of these shims are diffusion bonded to create a single monolith.

diffusion bonding steps required, three units were etched into a single shim design. After diffusion bonding, the three reactors were cut apart and machined separately. The overall dimensions of this one-eighth-scale reactor are 11 x 2.3 x 3.7 cm and it weighs approximately 160 g. A photograph of a completed reactor is shown in Figure 4.10. Seven reaction microchannels each were used, interleaved with eight cooling (or RWGS) microchannels. Each microchannel was created with a top and bottom plate that contained the flow distributors and a spacer shim to provide for the catalyst volume.

To initially heat the reactor, electric rod heaters were placed on either end of the reactor. Once the reaction was initiated, these rod heaters could be turned off as the exothermic reaction maintains the reactor temperature. To control the temperature, coolant flow and temperature is adjusted. Similar to the RWGS reactor, before entering the microchannels, the feed gases passed through a recuperative heat exchanger. The recuperative heat exchanger heats the feed streams with the product streams.

The reaction temperature was measured with K-type thermocouples at the product gas entrance, the exit, and axially down the length of the reactor. The experiment was run near atmospheric pressure with a pressure range from 115 to 150 kPa.

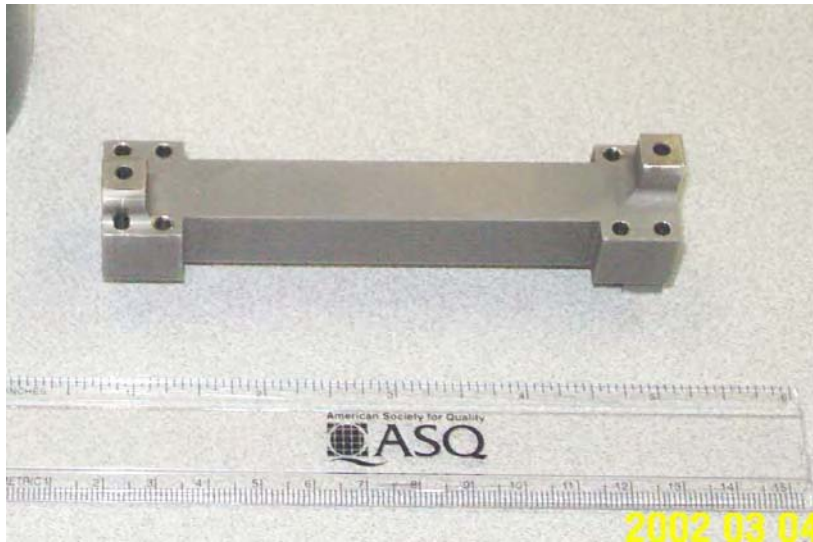


**Figure 4.10.** Photograph of the completed Sabatier reactor.

The SR reactor was evaluated over a range of temperatures and contact times at a constant  $H_2$  to  $CO_2$  ratio of 4 (stoichiometric). Due to the exothermicity of this reaction, in some cases, it was difficult to maintain the reactor isothermal. In general, the first axial temperature was 20 to 30°C higher than the subsequent temperatures down the length of the reactor. This problem was exacerbated at lower contact times. The initial experimental results are shown in Figure 4.11. For comparison, equilibrium conversions possible for 1) an isothermal reactor operating at 400°C and 2) a theoretical adiabatic reactor with an initial temperature of 400°C are also plotted. At a contact time of ~ 400 ms, the  $CO_2$  conversion is within experimental error of the equilibrium conversion of 84.9%. As expected, the conversion decreases at lower contact times. To achieve the methane production for 1/8<sup>th</sup> scale of the sample-return mission with this reactor, a contact time of approximately 100 ms is required. This would result in slightly more than 70% conversion in the reactor. These values are less than the target performance criteria specified in Table 4.1. By controlling the temperature of the reactor rather than allowing it to operate adiabatically, the  $CO_2$  conversion increased from a possible 66% to over 80%.

Over the course of several days of experimentation, there was a steady decline in the catalyst activity (Figure 4.12). Several approaches were taken to improve the catalyst activity. If the reduction in activity were associated with the catalyst becoming oxidized, reduction would have improved the conversion. If it were coking, the oxidation and re-reduction of the catalyst would have improved the performance. Based on the results these approaches did not recover catalyst activity, indicating possibly catalyst sintering and the reason for the decline.

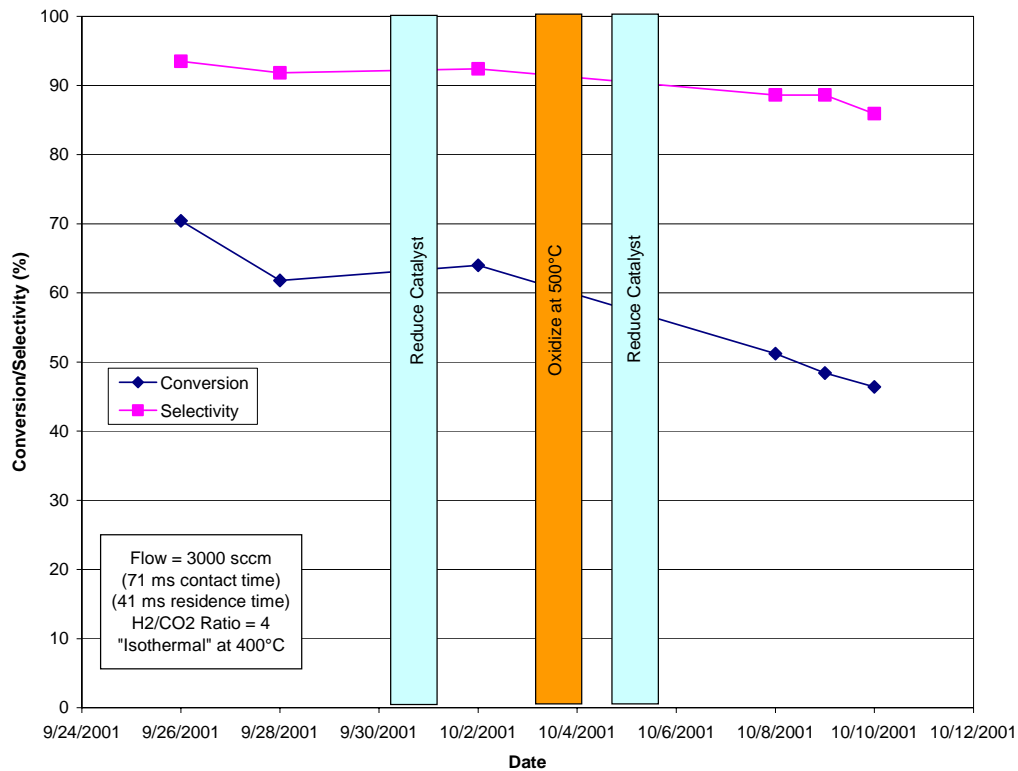


**Figure 4.11.** Conversion and selectivity of the SR as compared to thermodynamic calculations.

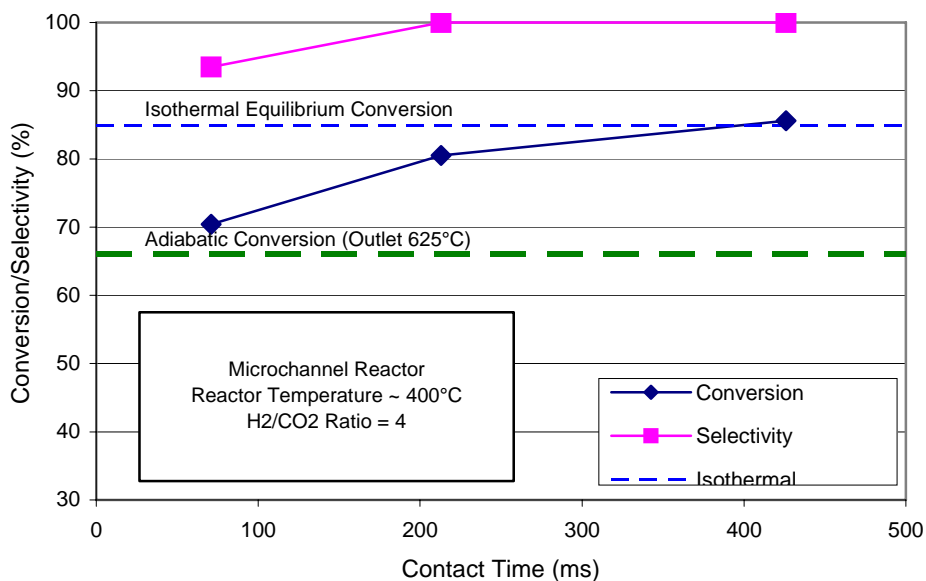


**Figure 4.12.** Deactivation of the SR catalyst over time.

This decline in activity made it difficult to compare later experiments with earlier data. Furthermore, with the decline in activity it was difficult to see the positive effects of creating a temperature profile down the length of the reactor. With a deactivated catalyst, it was not possible to achieve equilibrium conditions at the entrance temperature, thus reducing the temperature to achieve higher conversions only resulted in slower kinetics and reduced conversion.

#### **4.4 Combined RWGS/SR System**

As discussed in the section above, a 1/8<sup>th</sup> scale reactor was developed to test both the SR alone and the combined RWGS and SR. In the case of a combined reactor, 7 channels of the SR reactor were filled with SR catalyst and the interleaved 8 channels were filled with the RWGS catalyst. Gases were installed to allow gases to flow counter-current and preheating of both gases were performed with recuperative heat exchangers. The reactor/recuperative heat exchanger configuration is shown in Figure 4.13. Because the SR flow rates are lower than the RWGS to meet the NASA ratio requirements, there is more sensible heat associated with the RWGS than the SR. The RWGS products were then used to preheat both the RWGS and SR feed.

Before the combined reactors were run, each individual reaction was performed to better understand the conditions of operation. These second set of tests also studied the effect of partial pressure of reactants on conversion. Due to the equipment size and energy costs for compression of the CO<sub>2</sub>, lower pressures should be considered. Due to equipment constraints, the system was not operated at less than atmospheric pressure. Instead, nitrogen was added to the system as a diluant. Results were then compared to a process with the same throughput rate.

The partial pressure experimental results for the RWGS are shown in Table 4.3. Reaction kinetic models generally indicate the reaction rate is proportional to the partial pressure of the reactants. Thus, one would expect that the reaction rate and thus the conversion would be lower at lower partial pressures. However, the results indicate little reduction in conversion with a 5-fold decrease in reactant partial pressure. Such a result would allow a decrease in pressure to the RWGS reactor without significant effect to the conversion. In addition, the lower partial pressure resulted in higher selectivities to CO, which would reduce the load on the separations equipment downstream of the reactors.

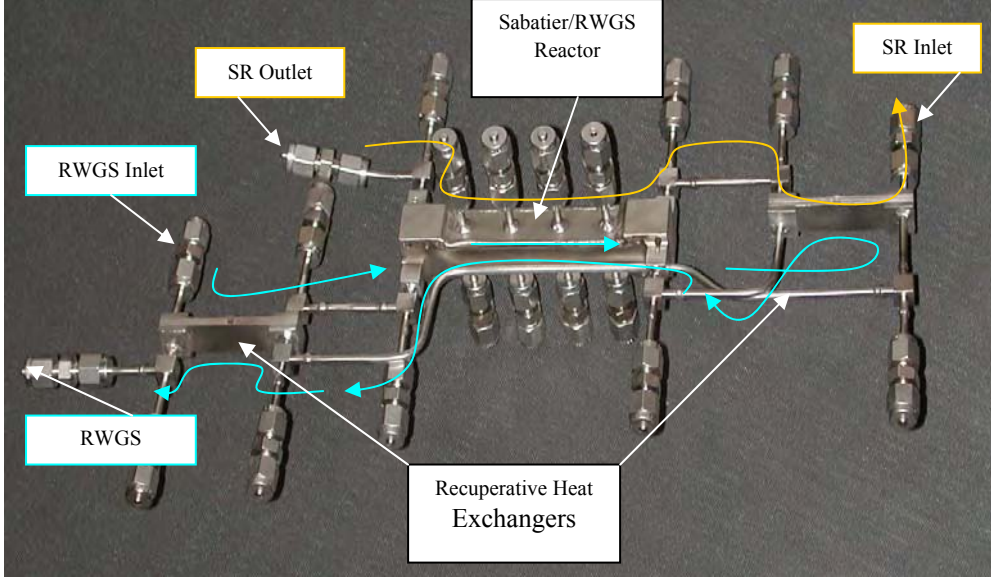


**Figure 4.13.** The combined RWGS/SR reactor with its associated recuperative heat exchangers. Both the reactor and the heat exchangers operate in the U-configuration (gases exit on the same side as they enter).

**Table 4.3.** Effect of Reactant Partial Pressure on the RWGS Reaction

Reaction Temperature (°C)	CO <sub>2</sub> Partial Pressure (atm)	CO <sub>2</sub> Conversion (%)
410	0.5	16%
510	0.5	27%
440	0.1	18%
490	0.1	21%

The data presented for the RWGS reaction both here and in the previous section was used to develop a kinetic model. Because the composition of the catalyst is not known, available literature on particular catalysts could not be used. Initial approach was to use a simple exponential model and vary the exponents for the best fit between model and experimental data. The model that best fit of the experimental data is:

$$r_{CO_2} = \frac{k \left( P_{CO_2} P_{H_2} - \frac{P_{H_2O} P_{CO}}{K_{eq}} \right)}{(1 + k_2 P_{H_2} + k_3 P_{CO})} \quad (4.3)$$

The activation energy was 20 kcal/mol and the adsorption coefficients for H<sub>2</sub> and CO were allowed to vary exponentially with temperature and were approximately 100 and 10000 at 500°C and decreasing to 1 and 100 at 700°C, respectively. This model suggests that H<sub>2</sub> and CO adsorb significantly on the surface of the catalyst at lower temperatures, hindering the adsorption and reaction of the CO<sub>2</sub>. At higher temperatures the effect is decreased.

A comparison between model and experiment was performed for the RWGS data taken over the range of 400-550°C, a H<sub>2</sub>:CO<sub>2</sub> ratio between 1 and 4, a contact time from 72 to 362, and diluent to reactant gas ratio between 0 and 9. The results are shown in Figure 4.14. Significant excursions from the experimental data occur primarily at the higher conversions that correspond to H<sub>2</sub>:CO<sub>2</sub> ratios of 4.

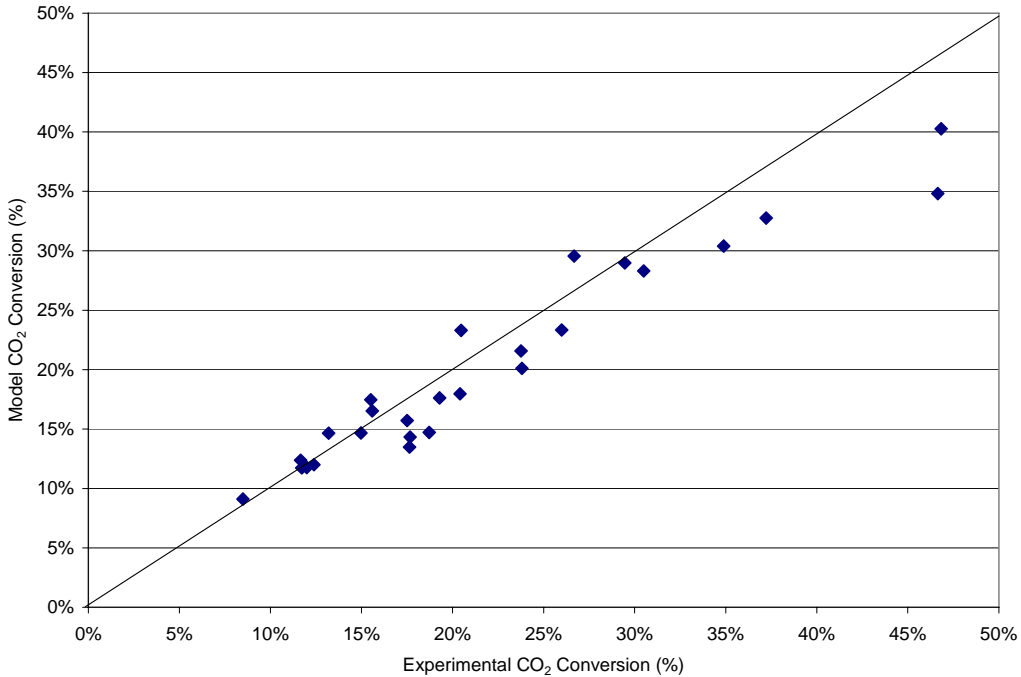


**Figure 4.14.** RWGS experimental data compared to the model for the 8 channel reactor data.

Using the combined reactor and nitrogen flowing through the RWGS channels, the SR was also studied at lower partial pressures. The results of this comparison are shown in Table 4.4. As can be seen from the results shown, both the conversion and the selectivity decrease at the lower reactant gas partial pressure. Thus, for this particular reaction, there would be less benefit in reducing the pressure of the inlet gases than in the case of the RWGS reaction.

**Table 4.4.** Effect of Reactant Gas Partial Pressure on the Sabatier Reaction<sup>a</sup>

P <sub>CO<sub>2</sub></sub> (atm)	CO <sub>2</sub> Conversion (%)	CH <sub>4</sub> Selectivity (%)
0.23	69%	91%
0.063	41%	71%

a. Tests performed at H<sub>2</sub>:CO<sub>2</sub> = 4:1, ~450°C, and CO<sub>2</sub> flow of 123 sccm.

Similar to the RWGS, the data from a wide range of temperatures, H<sub>2</sub>:CO<sub>2</sub> ratios, and contact times were used to develop a model for the Sabatier reactor. Once again, because the composition of the catalyst was not known, available literature on particular catalysts could not be used. The best fit of the experimental data is seen as follows:

$$r_{CO_2} = \frac{k \left( \frac{\sqrt{P_{CO_2}} P_{H_2} - P_{H_2O} P_{CH_4}}{\sqrt{P_{CO_2}} P_{H_2}^3 K_{eq}} \right)}{\left( 1 + \sqrt{k_2 P_{H_2}} + k_3 P_{CO_2} \right)} \quad (4.4)$$

where  $k_2$  is 10,000 and  $k_3$  is 100 and the activation energy is 11 kcal/mol. This model indicates that hydrogen dissociates on the surface of the catalyst and hydrogen and carbon dioxide are adsorbed on the surface. The experimental results as compared to the model are shown in Figure 4.15. As can be seen in the graph, there is some scatter in the experimental data, but the model fits the changes in partial pressure, contact time and temperature reasonably well.

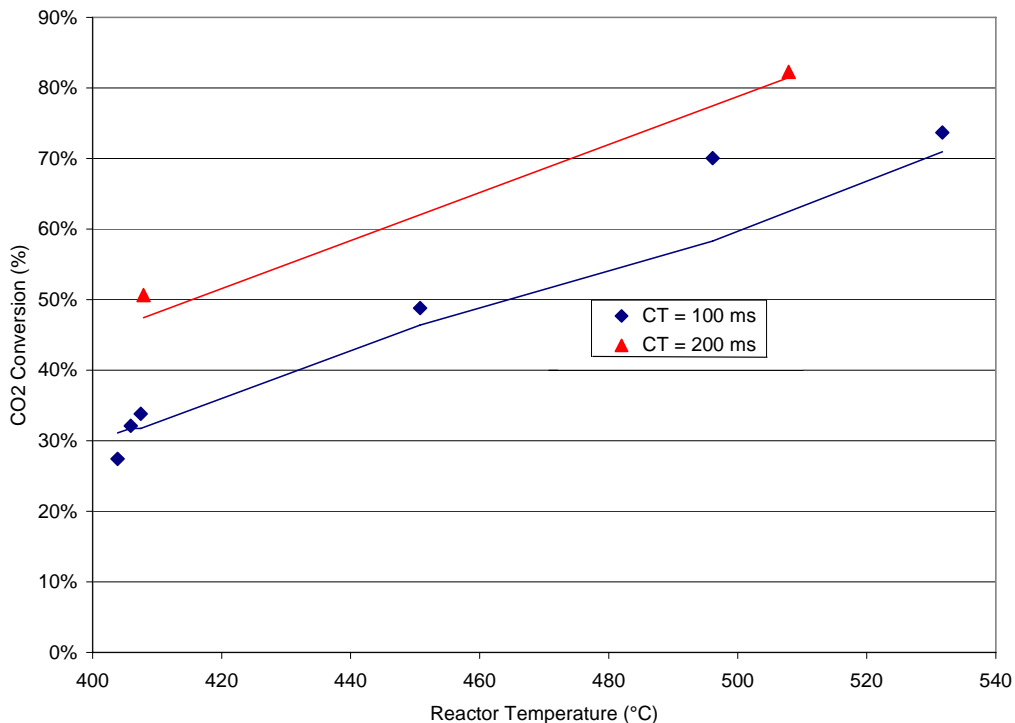


**Figure 4.15.** Comparison of the SR experimental data versus the model including reactant adsorption for  $H_2O:CO_2 = 6$ .

With both the catalysts in a single reactor, both reactions were operated simultaneously. A temperature profile was created along the reactor length to provide high temperatures for the inlet to the SR and the outlet to the RWGS. By adjusting the flow rate of both the reactions, the heat of reaction could more or less be balanced and the fraction of  $CH_4$  and  $H_2O$  could be balanced at the proper ratio. The results of this testing is shown in Table 4.5. In the table conversion and selectivity are shown for each reaction. Additionally, the production rate of water and methane are compared to the 1/8<sup>th</sup> scale Direct Robotic Return Mission Scenario. Runs 1-4 are run in a differential temperature mode of roughly the same magnitude while Runs 5 and 6 are individual reactions run isothermally for comparison. From the data one can see that with an increase in  $H_2:CO_2$  ratio and contact time, both the RWGS and SR reaction conversions increase. The selectivity of these reactions towards  $CH_4$  increases with an increase of these same parameters.

In contrast, the fraction of the required production rate decreases with increased H<sub>2</sub>:CO<sub>2</sub> ratio and contact time. Thus there must be an optimization between obtaining high production and obtaining high conversion.

The isothermal case and differential case can be compared for the RWGS and SR by comparing Runs 2 and 5 and Runs 3 and 6, respectively. The differential case results in a decrease in both conversion and production rate as compared to the isothermal case. This result is not surprising for the endothermic RWGS reactor, where higher temperatures will result in higher conversions and selectivities. For the SR case, the result is less expected. It indicates that conversion is not being reached early within the reactor and allowing the equilibrium conversion to increase as the temperature decreases further down the reactor. This is probably due to the catalyst deactivation that occurred. Further testing will be needed with non-deactivated catalyst to determine if the differential temperature approach can be beneficial.

**Table 4.5.** Combined RWGS/SR Reactor Results Summary

Experimental Conditions	Run 1	Run 2	Run 3	Run 4	Run 5	Run 6
T1 (°C)	381	378	378	378	556	532
T2 (°C)	515	564	553	551	556	532
RWGS H <sub>2</sub> :CO <sub>2</sub>	1	1	2	1	1	N/A
RWGS Contact Time (ms)	72	72	96	144	72	N/A
RWGS Conversion (%)	18%	23%	35%	26%	29%	N/A
RWGS CO Selectivity (%)	84%	87%	74%	84%	90%	N/A
RWGS Production Rate (%)	47%	62%	40%	34%	82%	N/A
SR H <sub>2</sub> :CO <sub>2</sub>	6	4	6	6	N/A	6
SR Contact Time (ms)	200	100	100	198	N/A	100
SR Conversion (%)	76%	52%	63%	78%	N/A	74%
SR CO Selectivity (%)	95%	85%	89%	94%	N/A	81%
SR Production Rate (%)	37%	62%	57%	37%	N/A	63%
N/A = Not applicable						

## 4.5 Data Evaluation

Using the models developed for the RWGS and SR, the impact of the differential temperature reactor and the reactor throughput can be better understood without the deactivation of the SR catalyst and without the heat losses of the experiment. By using the differential temperature reactor, the RWGS and SR reactions can be coupled together thermally and minimize the amount of heat required to the RWGS by using the heat generated by the SR reactor. A plot of the heat generated by the SR as compared to the heat required for the RWGS is shown in Figure 4.16 as a function of methane specific productivity. As can be seen from the figure, for a range of reactor throughputs and the required water/methane product ratio of 3.8, the amount of heat required within the reactor by the RWGS is less than the amount produced by the SR system. This would indicate that with minimal heat losses the reactions could be operated with little or no heat input. This would significantly reduce the energy requirements on the overall system.

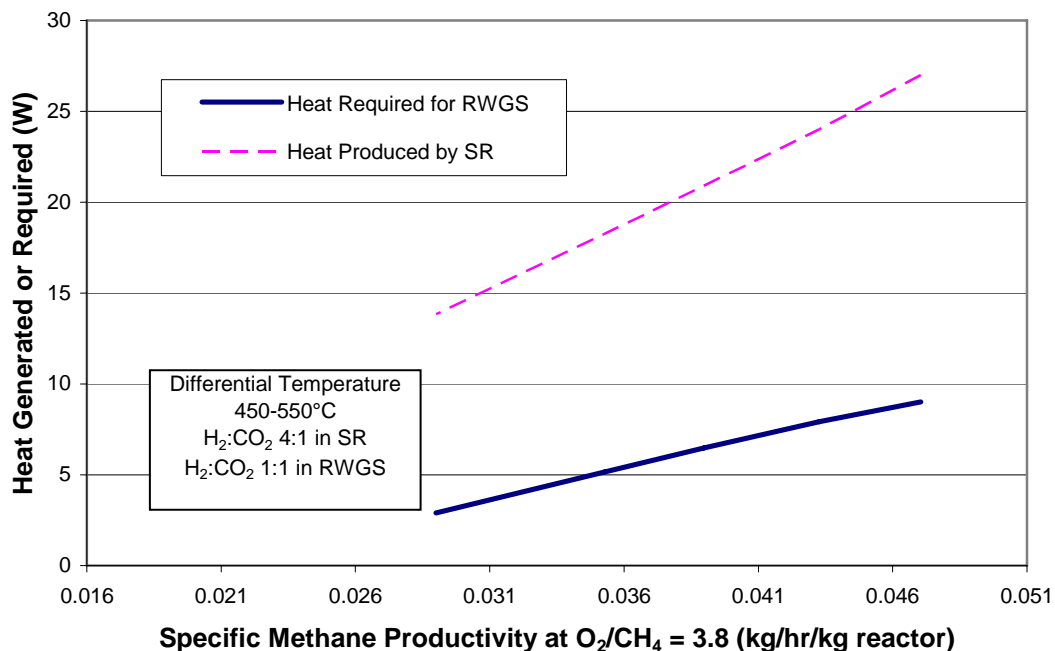


**Figure 4.16.** Heat generated by the SR and heat required by the RWGS are compared as a function of specific methane productivity at the required methane to water ratio.

Unlike the experimental data in the previous section, it should be possible to operate in a differential mode with a higher conversion than under isothermal conditions. If the reactor is operated over the range of 450 to 550°C, the Sabatier reaction model is optimized for highest conversion as shown in Figure 4.17. This conversion is higher than is possible at any single isothermal condition. Increased temperature results in reaction equilibrium limitations while lower temperature result in kinetic limitations.

The model shows that the temperature differential also results in a higher RWGS conversion than could be obtained under isothermal conditions at the average reaction temperature. Furthermore, using the differential temperature approach allows heat sharing between the two reactions and increases the conversion of the SR.

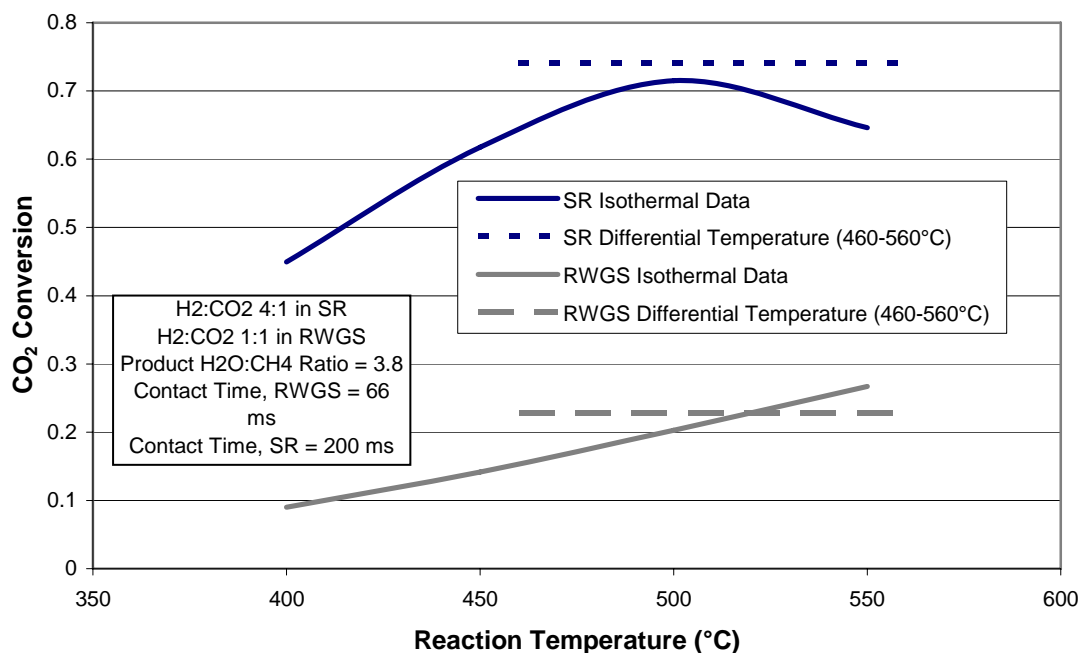


**Figure 4.17.** CO<sub>2</sub> conversion for both the RWGS and the SR reactions as a function temperature for the isothermal and differential temperature approaches.

The reaction system could be optimized alone to improve conversion and selectivity in terms of temperature, throughput rate, and H<sub>2</sub> to CO<sub>2</sub> ratio. However, to minimize overall mass of the entire production plant, these parameters should be optimized to account for the size of the CO<sub>2</sub> collection and product separations systems as well. In the case of the RWGS and SR reactions, by increasing the throughput rate per unit volume of reactor, the size of the reactor needed decreases. However, the conversions for the two reactions decrease as well. This results in a lower concentration of product gases (CH<sub>4</sub>, CO, and H<sub>2</sub>O) in the final product making them more difficult to extract from the large amounts of reactant gases (H<sub>2</sub> and CO<sub>2</sub>). Figure 4.18 compares the mass of the reactor based on a scaled mass of the prototype to the fraction of product gases. Based on the results shown, if high gas throughputs are attempted to make the reactor mass decrease the concentration of product gases quickly decreases. In contrast, as the gas throughput decreases sufficiently, eventually equilibrium is reached in the reactors and additional reactor size does not further increase the concentration of products in the reactor effluent.

A similar issue exists with the H<sub>2</sub>:CO<sub>2</sub> ratio. At higher H<sub>2</sub>:CO<sub>2</sub> ratios, both the RWGS and the SR reaction increase in conversion, however, more total H<sub>2</sub> passes through the reactors unreacted. Thus, the total product gas concentration also decreases resulting again in a larger separation system.

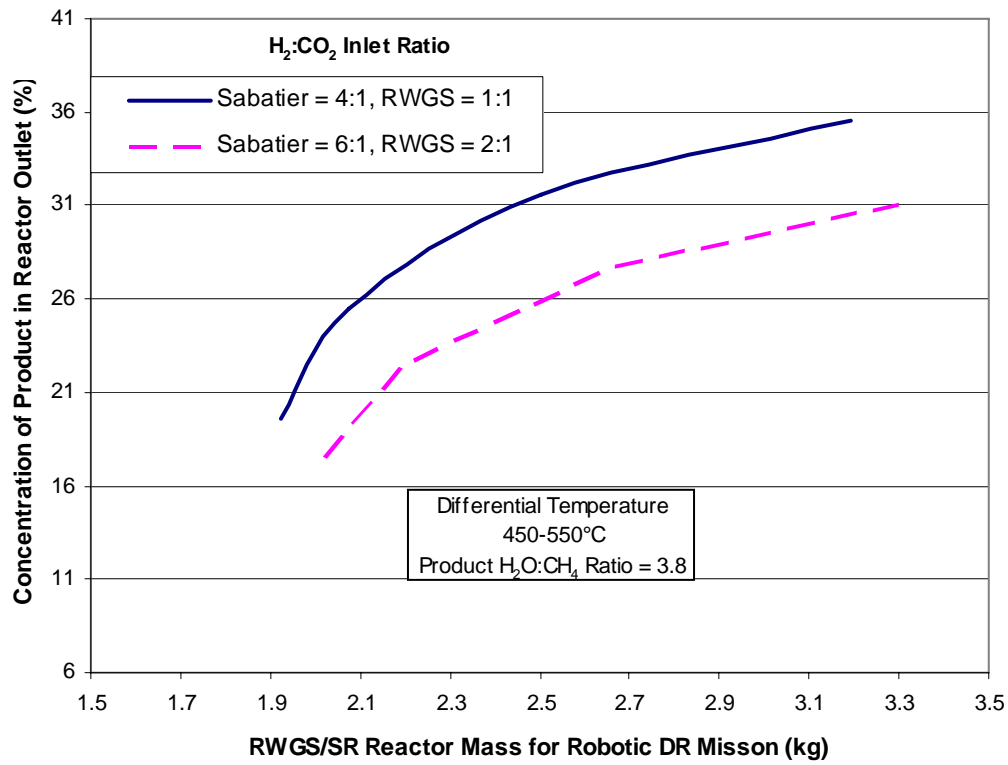


**Figure 4.18.** Concentration of product in the reactor outlet as a function of reactor mass. By increasing the reactor throughput rate, the mass of the RWGS and SR reactors can be decreased. This results in a decrease in the concentration of the product gases in the reactor output.

## 5.0 Phase Separation and Partial Condensation

Chemical separations and product purification are critical functions in an overall ISPP plant. Not only does cryogenic storage have very high purity requirements, but recovery and recycle of reactants and byproducts are crucial for high product yield, which is important for minimizing the consumable mass brought from Earth. In this effort, initial development of microchannel phase separation and partial condensation was pursued for recovering water from the effluents of the Sabatier and RWGS reactors.

The generic microchannel concept invented for gas-liquid processing is illustrated in Figure 5.1. The basic geometry has layers for gas flow and liquid flow. Porous structures, referred to as wicks or pore throats, are used to segregate the gas and liquid phases by capillary and surface forces. In addition, structures can be added to the gas flow channels that serve to capture liquid entrained in the gas flow. Heat exchange channels can be added as shown in Figure 5.1 to provide indirect heat transfer, if needed. When the thickness of the wick and the channels are less than a millimeter, capillary and hydrodynamic forces dominate over gravity forces, making this a desirable technology for space and reduced gravity environments. A wide range of physical and chemical processes can be supported with this geometry, including phase separation, condensation, gas absorption and desorption, distillation, and catalytic separations. PNNL has successfully patented multiple aspects of the technology (TeGrotenhuis, 2003, 2005a, 2005b).

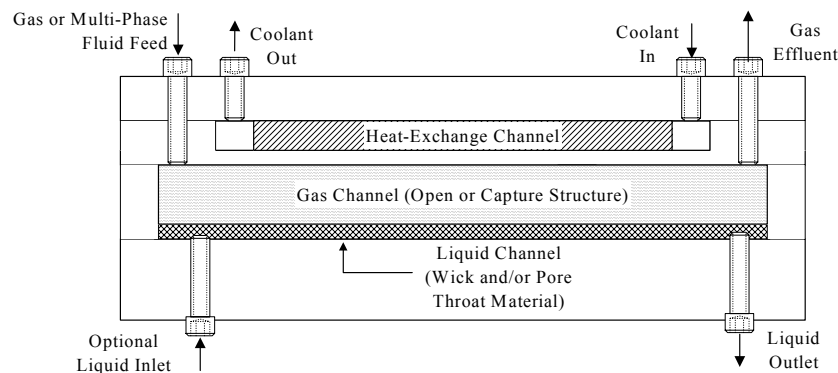


**Figure 5.1.** Wicking single microchannel separator shown in co-current flow.

Work on this technology began with proof-of-concept experiments using a single channel device to separate mixtures of gases and liquids. Liquid water was combined with air in a mixing T, and fed to the phase separator as shown in Figure 5.2. Within the device the gas channel was on top as shown in Figure 5.1 with no capture structure. The gas channel dimensions were 1.4 cm wide by 7.3 cm long and varying depths. The liquid channel was composed of a pore throat made of sintered stainless steel overlying a stainless steel screen and had dimensions of 2 cm wide by 8 cm long and varying depths. In some tests, an absorbent wick material, such as filter paper or cloth was added on top of the pore throat. The liquid phase was siphoned from the liquid flow channel by extending the outlet tube on the bottom to provide a suction head as shown in Figure 5.2. The length of tube was varied to determine the influence of suction pressure on performance, while not exceeding the breakthrough pressure where gas would displace liquid from the pore

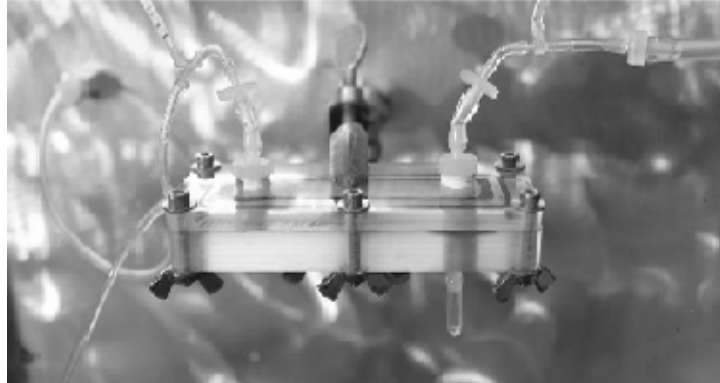


**Figure 5.2.** Single channel proof-of-concept phase separator.

throat and exit with the liquid. Phase separation performance was evaluated by collecting water from the gas and liquid-effluent streams and performing a mass balance.

Experiments were conducted by varying the gas and liquid flow rates of the feed stream as well as the liquid suction pressure. The permeability of the pore throat, which is given by Darcy's law and the hydrodynamic flow behavior of the system were found to limit the throughput of the device. As can be seen in Figure 5.3, 100% of the liquid is recovered at high ratios of the gas and liquid superficial Reynolds numbers, which correspond to lower liquid flows at a given gas flow. As the liquid flow increases at a given gas flow rate, eventually liquid breaks through to the gas outlet and complete phase separation is compromised. The liquid breakthrough point was found to be sensitive to channel geometry, the liquid suction pressure, and the flow behavior observed in the channel. When the device was operating effectively, water accumulates along the sides of the channel where it has time to sorb into the porous structure as seen in Figure 5.4. Eventually, water accumulation reaches the gas outlet and liquid breakthrough occurs. In other cases, the annular flow behavior is lost and the gas flow begins to entrain liquid.

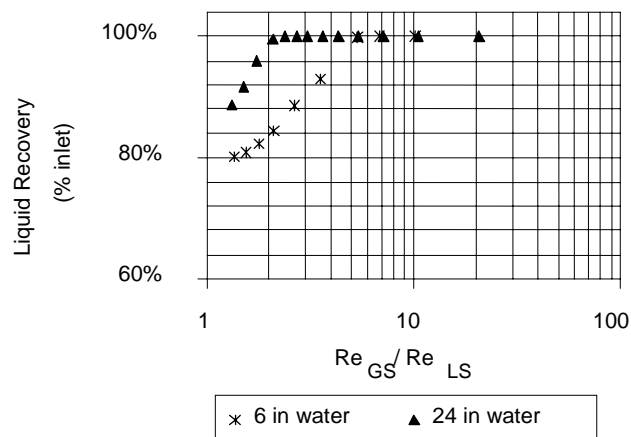


**Figure 5.3.** Percent of feed liquid recovered from the liquid outlet for water as a function of gas-to-liquid Reynolds number ratio ( $Re_{GS}/Re_{LS}$ ) for varying pressure differences across the pore throat.

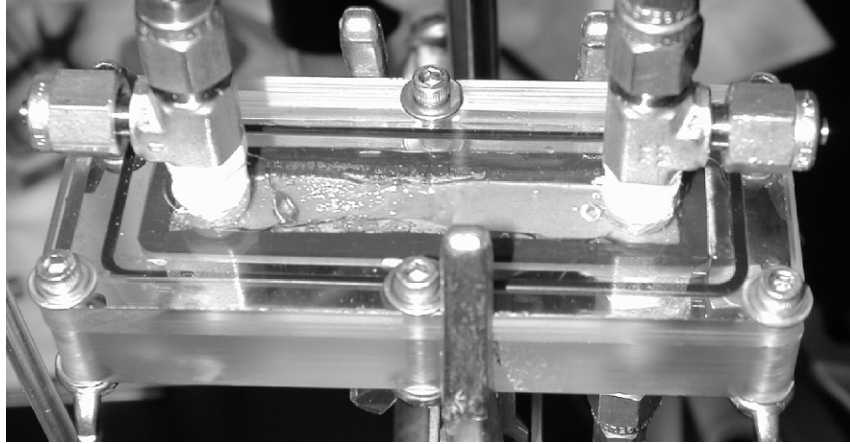


**Figure 5.4.** Single channel device running with flow from left to right at flow rates of 40 mL/min of water and 1 SLPM of air. The pressure difference across the pore throat is 12 inches of water. No breakthrough is observed.

The transition from complete to partial separation was correlated with the transition from annular to slug flow for zero-gravity pipe flow (Jayawarden et al. 1997; TeGrotenhuis and Stenkamp 2001). Figure 5.3 also illustrates that water recovery depends on the liquid suction pressure due to the flow capacity of the pore throat which follows Darcy's law. The greater the pressure differences across the pore throat, the greater the liquid throughput at the incipient liquid breakthrough into the gas exit.

This capillary driven separation technology has also been demonstrated in zero gravity on NASA's KC-135 initially using the single channel device in Figure 5.2 (TeGrotenhuis and Stenkamp 2005c). Although this work was performed for NASA for a separate project, it indicates that this device can also operate in an ISPP system at the reduced gravity found on Mars.

The single channel device was subsequently modified to add a heat exchange channel to demonstrate partial condensation and phase separation of water vapor from air. In these tests, water vapor was condensed and the condensate simultaneously removed from the air in the same device. The concept was then extended to an air-cooled partial condenser-phase separator shown in Figure 5.5, which was also successfully operated on the KC-135. There are two sets of five parallel gas flow channels that are 0.25 mm deep, 4.3 mm wide, and 14.5 cm long with a phase separator structure located between as shown in Figure 5.5. The heat exchange side of the gas flow channels is formed by heat exchange elements. Cooling is provided by air flow through two heat exchange elements located adjacent to the gas flow channels. These aluminum heat exchangers have 142 slots that are 0.61 mm wide, 2.5 mm tall and 3.05 cm long. The slots are separated by 0.25 mm wide webs that serve as heat exchange fins to enhance cooling. Power density and specific power of the heat exchanger elements are shown in Figure 5.6 as a function of the water content of the feed. The energy density was found to range between 2 and 12 W/cm<sup>3</sup> while the specific energy reached values of 1200 to 8000 W/k (TeGrotenhuis and Stenkamp 2005c).



**Figure 5.5.** Close-up of one end of the air-cooled partial condenser-phase separator that was demonstrated in zero gravity on NASA's KC-135.

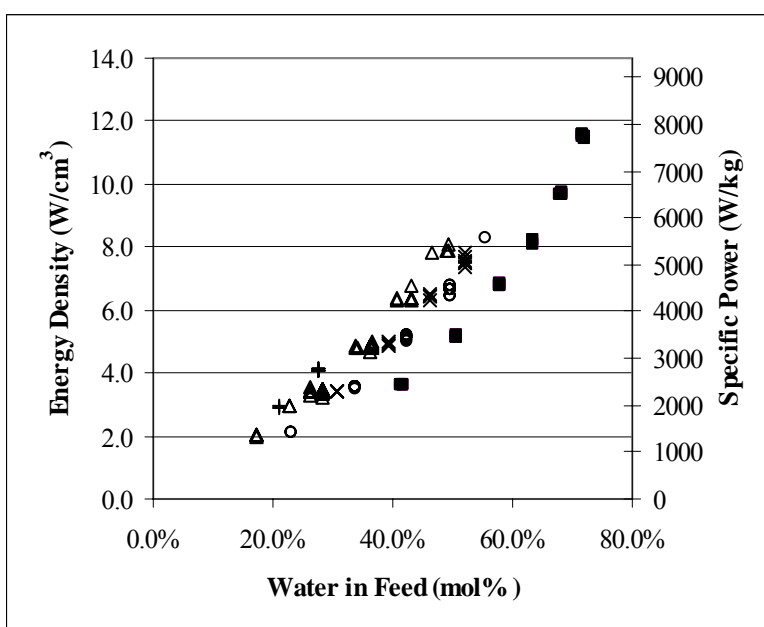


**Figure 5.6.** Thermal energy density and specific power versus percent water in the feed at condensing stream air flows of 11 SLPM (+), 10 SLPM (◇), 9 SLPM (Δ), 8 SLPM (x), 7 SLPM (○) and 5 SLPM (■).

Scaling-up this technology is accomplished by numbering up arrays of channels to achieve the required capacity. When heat exchange is required, the gas-liquid processing channels are interleaved with heat exchange to maintain the high surface area to volume ratio required for high effectiveness. Scale-up of the phase separator was performed for the application of removing water from the cathode effluent stream of a 5 kW polymer electrolyte membrane (PEM) fuel cell that was being developed for a proposed NASA space plane. The specifications for water separator required removing 40 ml/min of liquid water from the cathode effluent, processing 2.7 to 54.3 SLPM of humidified oxygen at pressures from 45 to 75 psia and temperatures up to 80°C without exceeding 5 psi pressure drop, and operating effectively in zero gravity up to 3 g. The device shown in Figure 5.7 containing three gas flow channels was designed, built, and tested in



**Figure 5.7.** Multichannel phase separator device built to remove water from the cathode effluent of a 5 kW PEM fuel cell.

normal gravity in three orientations and in zero gravity aboard the KC-135 (TeGrotenhuis and Stenkamp 2005c). Complete separation was achieved in zero gravity with 120 mL/min of water in 20 SCFM of air flow and also with 43 mL/min of water in 95 SCFM of air, thereby exceeding the design requirements for the device.

The capability to process gases and liquids in microchannels to accomplish phase separation, heat transfer, and mass transfer is a significant capability for broadening the processes that can be performed in space systems, not only for ISRU but also for power, life support, EVA, and thermal management systems. The description here has focused on phase separation and condensation, but the technology is also under development for mass transfer applications, including gas absorption and desorption for absorption cycle cooling systems as well as for distillation and catalytic distillation.

## 6.0 System Modeling

A system model of the microchannel ISPP plant is needed to generate performance requirements for the individual unit operations. A tool that includes design models for individual components of sufficient fidelity to predict sizes and weights can also facilitate optimization of the overall system for size and weight as well as performance. In addition, a tool for comparing possible flow sheets and technologies will enable selection of the best plant to accomplish the mission. A description of the modeling approach is provided in the next section followed by examples of parametric studies and a comparison of the microchannel ISPP plant to baseline information provided by JSC [private comm].

### 6.1 System Modeling Approach

A framework for an ISPP system model was developed using Microsoft Excel. At the top layer, a user interface is provided as a flow sheet with blocks of cells assigned to each unit operation as shown in Figure 6.1. As an example, the RWGS and Sabatier reactors along with their recuperative heat exchangers are shown in Figure 6.1, as well as an absorption cycle CO<sub>2</sub> compressor. For each unit operations, parameters are input into cells that are denoted by red

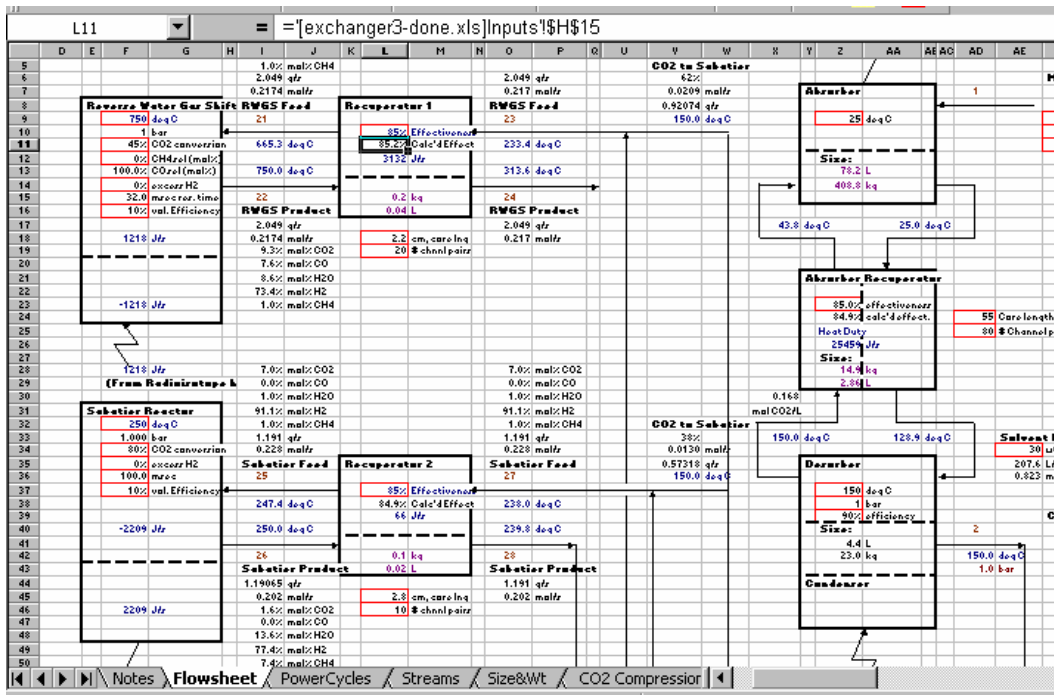


**Figure 6.1.** Example section of the flow sheet page of the microchannel ISPP system modeling tool.

borders. Entering values into these cells automatically updates the calculations for the entire spreadsheet. Calculated parameters and performance metrics are displayed along with the temperature, pressure, flow rate, and composition of each stream. Temperatures, heat duties, and heat transfer metrics are displayed in blue. The cells containing flow sheet parameters are

assigned names and can be set within macros in order to perform parametric and trade studies as well as for implementing optimization algorithms. Dropdown menus are used to toggle between different system configurations and technology options. For example, both low temperature and high water electrolysis options were implemented in the “microISPP” plant model. A dropdown menu was used to select which technology to use in the system and the system model ‘plugged in’ the appropriate unit operation model by adjusting the input and output streams accordingly. A similar capability was provided for toggling between mission scenarios, i.e. sample return versus human scale and direct return versus orbital rendezvous. The available options could easily be expanded to include other scenarios such as propellant and life-support oxygen production versus propellant production only. This would simply require adjusting the production requirements for the two products, methane and oxygen.

Separate spreadsheets are developed for each section or class of technologies within the system model. Within these spreadsheets, the detailed calculations for each unit operation model are performed including heat and mass balance calculations and size and weight estimates. A table containing coefficients for thermodynamic properties correlations is included along with macro functions to facilitate heat transfer calculations. Where design models are available for hardware components, principally heat exchangers, links are embedded to the design models in order to access more accurate size and weight estimates. As the technologies mature, additional data are acquired, and more design models become available for more hardware components, the tool can be readily updated to maintain consistency and the system re-optimized for size and weight.

The system modeling framework and initial flow sheets were developed under a PNNL Laboratory Directed Research and Development project (LDRD). The objective of that effort was to assess the viability of using radioisotopes to power a Martian ISPP plant, so a number of thermodynamic power and heat pump cycles were included along with a radiator for heat rejection. The tool that was developed in the LDRD effort was used as the starting point for system modeling in this effort, with scenarios being implemented for direct sample return, orbital sample return, a human scale mission, and also for the PNNL breadboard development effort.

The initial focus of the system modeling effort was in the upstream technologies with modules implemented for an absorption cycle CO<sub>2</sub> compressor, the Sabatier and RWGS reactors, high and low temperature water electrolysis, and associated heat exchangers. Water condensing heat exchangers were also derived based on design calculations. Membrane separation calculations were used as placeholders to complete overall material balances for the system, and future efforts will need to implement actual prospective technologies for accomplishing the recycle, recovery and purification functions. Furthermore, cryogenic coolers and mechanical components, such as pumps, blowers, and compressors were not included.

The generic approach for estimating sizes and weights when detailed design models are not available for microchannel hardware components is to estimate a residence time required for a given process. Residence time is the standard performance metric for heat and mass transfer limited operations, including reactors, heat exchangers, and separators. The volume and weight of the hardware are subsequently estimated by multiplying by a total volume to working volume factor and a material density factor, respectively. These factors are derived from historical knowledge of microchannel prototypes, and the results are first order estimates for hardware size and weight.

Energy is another important consideration for operating plants in remote, resource limited environments such as on Mars. To the extent that is practicable, the microchannel ISPP plant is thermally integrated with high effectiveness heat exchangers to minimize heat and power requirements of the overall system. Energy requirements for the “microISPP” plant are broken down between heat and electrical power requirements. By differentiating, the opportunity for integrating this plant with other potential heat sources such as power generation systems can be assessed. The predominant electrical demand is associated with water electrolysis, although cryocooler demands are not included. When CO<sub>2</sub> compression is heat-actuated, such as is possible with absorption cycle, adsorption cycle, and solidification options, the other significant power demands are for compressing the recycle streams.

## 6.2 System Parametric Studies

As mentioned above, the initial development of a system modeling tool occurred within a PNNL LDRD project, which looked at the potential for using radioisotopes to provide the requisite energy for a Mars ISPP plant. A schematic of the proposed process is shown in Figure 6.2. Descriptions of parametric studies for this system are included here to illustrate the potential for system optimization and technology comparisons.

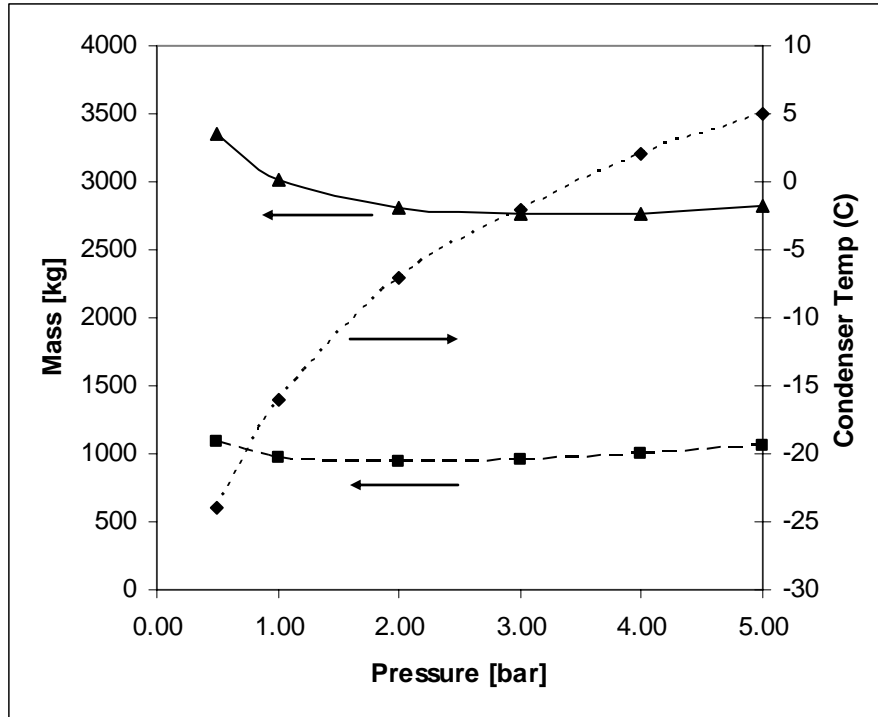
The schematic in Figure 6.2 represents a thermally driven process with all of the consumed electricity being generated with heat engines. The flow sheet illustrates some important aspects of a heat-driven ISPP plant. High efficiency is achieved through extensive recuperation and energy cascading from hot unit operations (catalytic reactors) to cold operations (separation and CO<sub>2</sub> acquisition), thereby minimizing the thermal and electrical demands. An important part of any chemical plant is the overall heat balance. Whereas heat rejection in terrestrial plants is usually straightforward, the limited capacity for convective cooling in the sparse Martian environment implies radiating heat to the cold sink of space will be required to maintain an overall heat balance in the plant. A heat pump is included in the system in Figure 6.2 to allow the operating temperature of the radiator to be increased above the lowest temperature of the system, thereby enabling trade-off between radiator size and operating temperature.

Figure 6.2 is but one possible flow sheet for the ISPP system. In this study, a liquid absorption cycle is used to compress the carbon dioxide, and Sabatier and RWGS are used for CO<sub>2</sub> conversion. Water electrolysis is accomplished with an energy efficient but immature high temperature electrolysis technology. Product separation and purification is performed with membranes and a cryo distillation system, although the distillation unit and cryocoolers (not shown) are not included in the size and weight calculations.

Both Brayton and Rankine cycles were included as options for the power cycles, and reverse Brayton and Vapor Compression cycles were represented as heat pump cycles. Two power cycles were included. One power cycle utilized the desorber as the low temperature heat sink for energy efficiency. A second cycle using a radiator to reject heat was sized to provide the balance of the electricity demand of the system.

The system represented in Figure 6.2 is only one of many potential flow sheets and technology suites that can be deployed in the ISPP plant. In addition, many assumptions were made in calculating the performance of each subsystem, heat and material balances, and size and weight





**Figure 6.3.** Effect of operating pressure on the mass of the ISPP plant (■), the ISPP plant plus power and cooling cycles (▲), and the condenser operating temperature to achieve 98% water recovery from the reverse water gas shift reactor effluent (◆).

Figure 6.3 shows how system size and performance can be sensitive to operating parameters. A similar analysis can be performed comparing different flow sheets and technology options within a flow sheet. An example of this is illustrated in Figure 6.4 for the absorption cycle CO<sub>2</sub> compressor. As described above, the absorption cycle utilizes an absorbent molecule like diethanolamine (DEA) within a solvent to absorb CO<sub>2</sub> at low pressure and temperature. With the Martian ambient pressure of only 6 Torr, the volatility of the solvent must be extremely low and water is not suitable. An alternative solvent, polyethylene glycol (PEG) is suitable but has a high viscosity resulting in a very low diffusivity of around  $6 \times 10^{-7}$  cm<sup>2</sup>/s. The low diffusivity translates into large residence times to affect the necessary mass transfer in the absorber. Sizing a microchannel absorber with 100 micron channels results in a CO<sub>2</sub> compressor that is expected to be about half of the total “microISPP” plant, and the absorber component is about 85% of the compressor as seen on the left side of Figure 6.4. Efforts to identify an alternative suitable solvent with a diffusivity that is 5X higher could have a dramatic impact on the size of the compressor and the overall system. By identifying which subsystems, components, and even physical properties are making the dominant contributions to the overall size of the plant, efforts can be targeted where they will have the greatest impact.

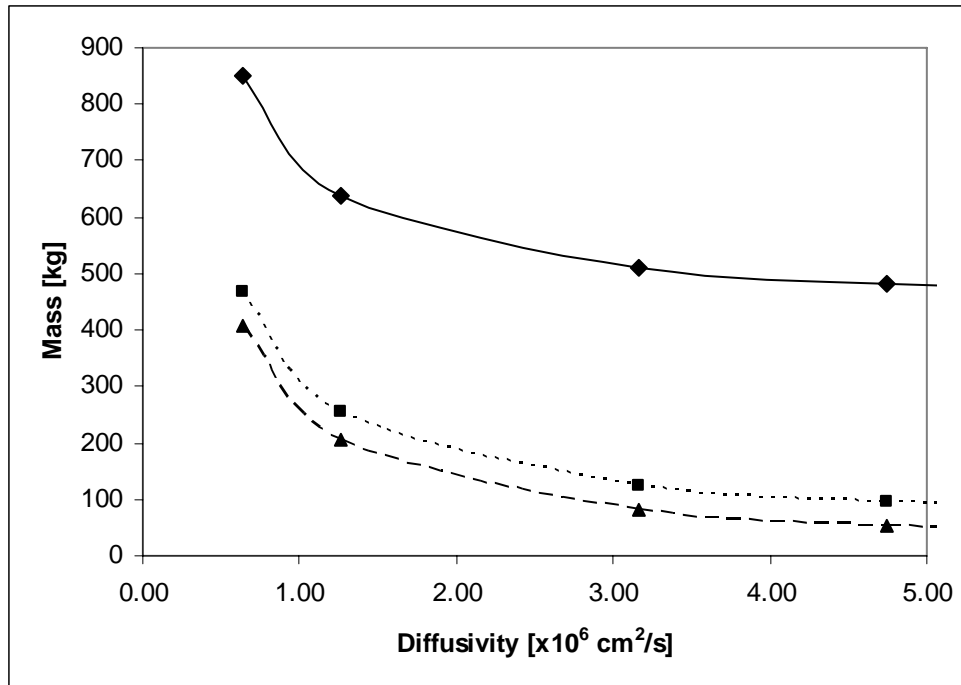


**Figure 6.4.** Effect of CO<sub>2</sub> diffusivity in the solvent on the mass of the ISPP plant (◆), the mass of the overall absorption cycle CO<sub>2</sub> compressor (■), and the mass of absorber component only (▲).

### 6.3 Comparison of the “MicroISPP” Plant to Mission Baselines

Comparisons of alternative flow sheets and technologies will depend on the mission scenario selected. Several studies of mission scenarios have been performed looking at different concepts, production durations, and propellant demands, as well as different propellants and production strategies (diurnal versus continuous). Here, three potential scenarios have been used that represent propellant production using CO<sub>2</sub> collected from the atmosphere and H<sub>2</sub> brought from Earth. The first two represent sample-return missions, one supplying propellant for direct return from the Mars surface and the second for orbital rendezvous. The third mission scenario is a human-scale mission that would provide propellant for the return home.

In all three cases, baseline size, weight, and power requirements have been prepared for systems comprised of an adsorption bed CO<sub>2</sub> compressor, a zirconia cell and RWGS reactor for CO<sub>2</sub> conversion, and an electrolysis cell [private comm.]. In each case, methane and oxygen are produced at a mass ratio of 3.8. The sample-return missions assume 400 days of 8 hours/day operation to produce 930 kg and 1500 kg of propellant for orbital rendezvous and direct return, respectively. The human scale assumes 300 days of 24 hours/day of operation to produce 14,200 kg of propellant.

A comparison of the entire ISPP plant is not currently viable because of inadequate knowledge for down stream separations and storage unit operations. Therefore, the comparison here is constrained to the CO<sub>2</sub> compression and chemical conversion processes. For the ISPP plant, heat exchangers are included in the size and weight, albeit they are not significant contributors.

An absorption cycle is used for the CO<sub>2</sub> compressor which operates with DEA in PEG between 25°C in the absorber and 150°C in the desorber to produce CO<sub>2</sub> at 1 bar pressure. A 90% effective recuperator is included for energy efficiency and the devices are sized using 100 micron channels assuming 3:1 total volume to working volume ratio and an average device density of 7.8 kg/L. The Sabatier reactor is operated at 250°C assuming 98% conversion of CO<sub>2</sub> with stoichiometric H<sub>2</sub> at 100 milliseconds residence time and with an 85% effective recuperator for heat exchange between the feed and recycle streams. The RWGS reactor is operated at 750°C and is assumed to achieve 45% CO<sub>2</sub> conversion with 100% selectivity to CO at 32 milliseconds residence time and also has an 85% effective recuperator.

The demand on the water electrolysis process is considerably higher in the “microISPP” plant than in the baseline flow sheet, because the zirconia cell, which doesn’t produce water as a byproduct, is replaced with a RWGS reactor that does produce a mole of water for every mole of CO<sub>2</sub> converted. To simplify the comparison, the water electrolysis unit is assumed to scale linearly with the water electrolysis power demand, and the electrolysis unit in the micro ISPP is scaled from the baseline.

Figures 6.5 through 6.7 provide comparisons for the human scale mission of the mass, volume, and energy consumption breakdowns for the baseline versus “microISPP” plant. It is apparent that the chemical reactors are incidental in both the mass and volume breakdown. The CO<sub>2</sub> compressor dominates the mass of both systems and although the microchannel absorber is shown as lighter than the baseline adsorption bed, the uncertainty associated with this emerging technology makes the two systems virtually indistinguishable. The mass breakdown in Figure 6.5 does make the point that improvements in CO<sub>2</sub> compressor technology, such as identifying a lower viscosity, low volatility solvent or adopting the rapid thermal swing adsorption approach could have a dramatic impact on the weight of the overall Mars ISPP plant.

In considering the volume breakdown shown in Figure 6.6, the “microISPP” absorber is dramatically smaller as is expected with microchannel technologies. However, the reduction in volume is somewhat diluted by the increased size of the electrolysis unit for converting the extra water produced by the RWGS reactor. Again this analysis provides a preliminary Pareto analysis and conclusions require validation and are subject to change as the downstream processes are included in the system modeling.

Similar conclusions are drawn from the energy consumption breakdowns shown in Figure 5.7. The absorption cycle compressor is potentially more energy efficient because of the ability to effectively recuperate heat. In addition, eliminating the Zirconia cell saves additional power, but the savings are more than offset by the increased power demand for water electrolysis. The “microISPP” plant still shows the potential for power savings, but only if the thermal energy demand can be provided by some heat source other than electricity.

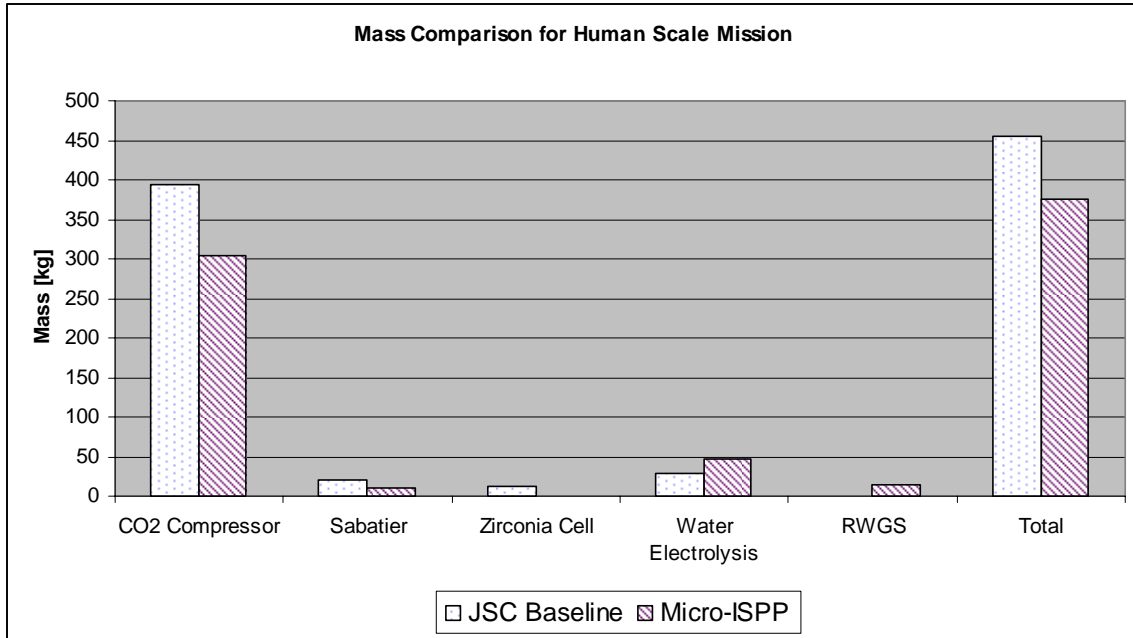


**Figure 6.5.** Comparison of component masses for the CO<sub>2</sub> compression and chemical conversion processes including associated heat exchangers between the “microISPP” plant and the baseline human scale mission to Mars.

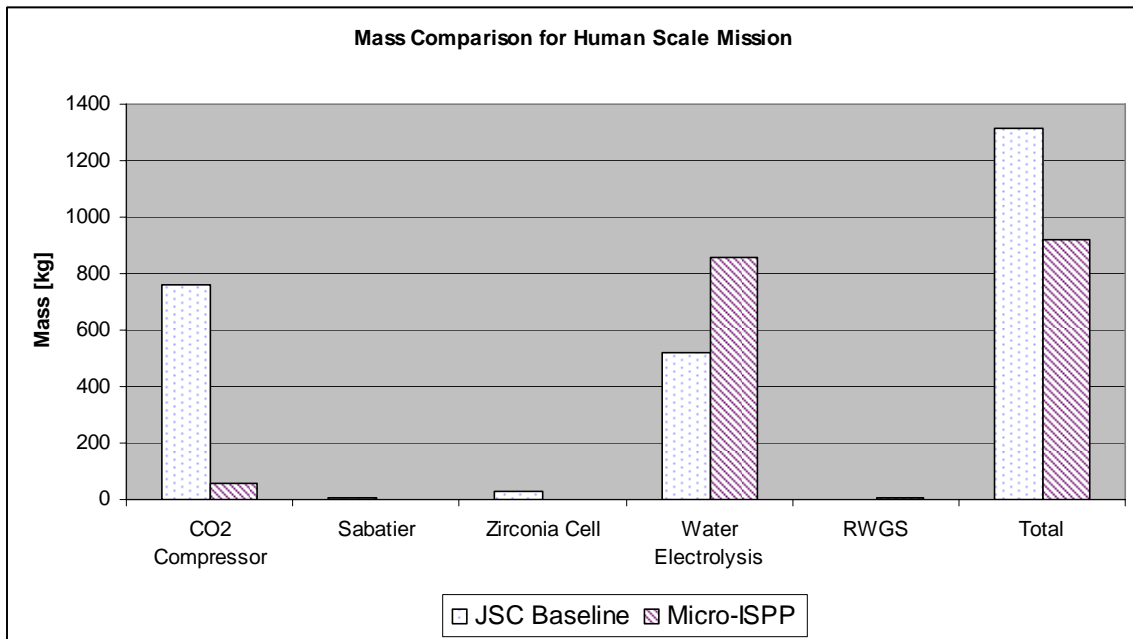


**Figure 6.6.** Comparison of component volumes for the CO<sub>2</sub> compression and chemical conversion processes including associated heat exchangers between the “microISPP” plant and the baseline human scale mission to Mars.

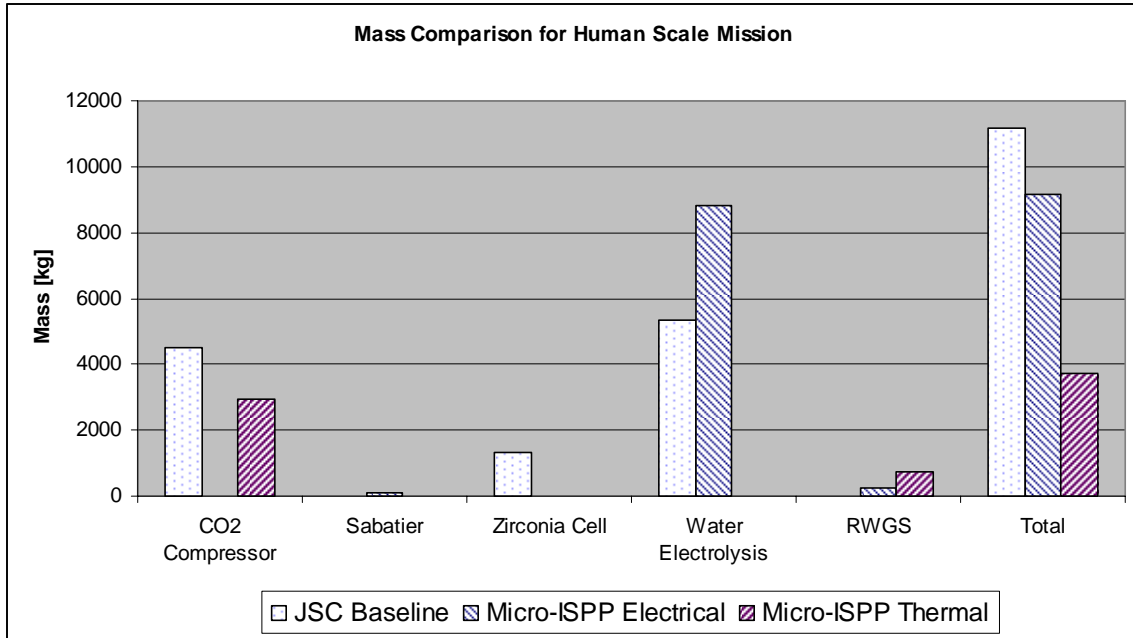


**Figure 6.7.** Comparison of electrical and thermal demands for the CO<sub>2</sub> compression and chemical conversion processes including associated heat exchangers between the “microISPP” plant and the baseline human scale mission to Mars.

Similar conclusions are drawn when comparing the “microISPP” plant to the baselines for the sample-return missions. One major difference, however, is the CO<sub>2</sub> compressor, which is much smaller in the baseline cases. This may be due to only operating 8 hr/day, such as by taking advantage of the diurnal cycle. No benefit is assumed with the absorption cycle compressor, which scales linearly with production capacity.

The conclusions of this section only reflect a preliminary assessment of the “microISPP” plant. There are certainly opportunities to realized substantial improvements in size and weight by continuing to apply process intensification principles for enhanced heat and mass transfer with microchannels. For example, rapid thermal swing adsorption is an excellent opportunity for both size and weight reduction and also for improved energy efficiency

## 7.0 Conclusions

Experimental and modeling work was performed to better understand the possible role of microchannel CO<sub>2</sub> absorbers and adsorbers and microchannel reactors in an ISPP system. Development work was also performed on microchannel condensers and phase separators. Most of this work was done on other NASA projects, but is included to show the utility of microchannels for a wide range of unit operations. The following conclusions were obtained from this work:

### CO<sub>2</sub> Absorption:

- Microchannel absorbers were developed using microwick and membranes as contactors. Testing was performed using a water/DEA and PEG/DEA solution to absorb CO<sub>2</sub> from a nitrogen stream. CO<sub>2</sub> absorption was studied as a function of temperature, absorbent concentration and liquid and gas flow rates. The CO<sub>2</sub> removal from the gas stream and the concentration of CO<sub>2</sub> in the liquid stream were measured to determine absorber performance.
- Tests performed with Teflon as the membrane contactor and using a microwick gas absorber. Microwicks have the advantage of improved ability to recover from flooding when compared breakthrough on a membrane. As expected, the thinner wicking materials and flow channels below the membrane result in higher mass transfer rates. These mass transfer rates are higher than measured in a conventional column.
- Increasing the gas flow rate and the DEA concentration results in increased CO<sub>2</sub> flux. Greater flux could also be expected by increasing the liquid flow rate, but this would lead to larger pressure drops and increased risk of liquid breakthrough in the contactor membrane.
- Adsorption was selected over absorption for system scale-up due to its improved robustness, the sorbent lifetime and recovery, device mass, and system efficiency.

### CO<sub>2</sub> Adsorption:

- Using a microchannel-based temperature swing adsorption system can significantly reduce the mass and energy needs for CO<sub>2</sub> collection and compression. The high heat and mass transfer result in a smaller device making a rapid temperature swing more feasible.
- Single channel testing performed with Zeolite 13X demonstrated the rapid temperature swing adsorption concept. A complete temperature cycle between 12 and 77 C is possible in two minutes with better than 90% of theoretical adsorption efficiency.
- A CO<sub>2</sub> adsorption system based on microchannel architecture was designed for a full-scale sample-return mission. The system uses eight multichannel cells and gases pass through the adsorbent either in a flow-by or a flow-through mode. By sequentially cycling each cell every two minutes, a semicontinuous flow of CO<sub>2</sub> is possible. Reduced heating and cooling requirements are possible by recuperating heat from the desorbing cells to heat subsequent cells.

## **RWGS Reaction**

- The RWGS catalyst prepared by BMI is robust over a wide range of conditions and showed no deactivation during testing.
- By operating the RWGS reaction at 700°C, conversions of greater than the targeted 45% can be achieved at 36 ms contact time. At these temperatures and throughput rates, the 30 channel/4 reactor RWGS monolith developed in this work would be capable of half-scale throughput for the robotic direct return mission.
- Due to equilibrium constraints, higher conversions could not be obtained in a single reactor and stoichiometric conditions. However, by adding a second reactor in series with water removal between the two reactors, the maximum conversion was increased to 60%. Similar increases in conversion were also possible by increasing the H<sub>2</sub>:CO<sub>2</sub> feed ratio.
- Coupling of the SR and RWGS allowed the reactions to operate without heat addition. However, RWGS conversion decreased to < 30% due to the lower operating temperatures required for the SR.
- Lower partial pressures of reactants did not significantly decrease the conversion of the RWGS.
- A model was developed that fit the experimental data reasonably well over the range of H<sub>2</sub>:CO<sub>2</sub> ratios, temperatures, pressures, and contact times investigated here.

## **Sabatier Reaction**

- The SR catalyst prepared by BMI deactivated over time making it difficult to demonstrate improved conversions with a differential temperature reactor. Results suggest that the catalyst may be sintering and losing surface area over time.
- The SR reactor was design for an 1/8<sup>th</sup> scale throughput rate for the robotic direct return mission. By operating the SR reactor at 400°C, conversions of between 70 and 80% could be achieved on a new catalyst for these throughput rates.
- Lower partial pressures of reactants decreased both conversion and selectivity of the SR.
- A model was developed that fit the experimental data reasonably well over the range of H<sub>2</sub>:CO<sub>2</sub> ratios, temperatures, pressures, and contact times investigated here.

## **Separations**

- Microchannel phase separation is a demonstrated compact technology for space applications, including successful operation in zero gravity.
- Design principles for scaling up microchannel phase separators have been successfully developed and applied, as evidenced by meeting design specs for a fuel cell system prototype.
- The capability to integrate microchannel heat exchange with phase separators provides a viable approach for partial condensation as a water recovery method in ISPP applications.
- Gas-liquid processing in microchannels is broadly applicable to chemical and thermal space systems, including power systems, life support, EVA, and ISPP.

### **System Modeling**

- A system model framework has been developed for a “microISPP” plant with modules included for an absorption cycle CO<sub>2</sub> compressor, reactors, and heat exchangers.
- Initial size and weight studies indicate that with current state-of-the art, the CO<sub>2</sub> compressor and the water electrolysis units are large relative to reactors and heat exchangers.
- Parametric studies of operating conditions and comparison of technology alternatives in a system context are needed to arrive at an ISPP system optimized for size and weight.
- Concepts for downstream chemical separations and product purification are immature and will be very important for achieving high product yield.

## 8.0 References

- Bird, RB, WE Stewart, and EN Lightfoot. 1960. *Transport Phenomena*, John Wiley & Sons, New York.
- Brooks, KP, SD Rassat, RS Wegeng, VS Stenkamp, WE TeGrotenhuis, and DD Caldwell. 2002. "Component Development for a Microchannel *In Situ* Propellant Production System." *AICHE 2002 Spring National Meeting*, Topical Conference: IMRET6 - 6<sup>th</sup> International Conference on Microreaction Technology, New Orleans, March 2002.
- Connolly, JF and RM Zubrin. 1996. "Pulling Propellants Out of Thin Air: Demonstration of an End-to-End Mars In-Situ Propellant Production Unit." In *Engineering, Construction, and Operations in Space V: Proceedings of the Fifth International Conference on Space*, pp. 706-716.
- Green, ST, DM Deffenbaugh, and MA Miller. 1999. "A Comparison of Five ISPP Systems for a Mars Sample Return Mission," AIAA 99-2410, in *35<sup>th</sup> AIAA/ASME/SAE/ASEE Joint Propulsion Conference*, Los Angeles, 1999.
- Jayawardena, S., V. Balakotaiah, V. and L.C. Witte. 1997. "Flow Pattern Transition Maps for Microgravity Two-Phase Flows", *AICHE J.*, 43(6), 1637-1640.
- Kaplan, DI. 1996. "Mars Sample Return using In-Situ Propellant Production." In *Proceedings of the International Conference on Engineering, Construction, and Operations in Space*, Vol. 2, pp 717-723.
- Kaplan, D. (ed.) 1988. *Environment of Mars*. NASA Technical Memorandum 100470. October 1988.
- Karlman P, K Johnson, D Rapp, and J Wu. 1999. "Development Unit Configuration and Current Status of the MIP/MAAC Experiment." LPI Contribution No. 963. *In Situ Resource Utilization (ISRU III) Technical Interchange Meeting*, Feb 11-12, 1999, LMA Waterton Facility, Denver, CO.
- Kohl, AL and RB Nielsen. 1985. *Gas Purification*, 4<sup>th</sup> Ed., Gulf Publishing Company, Houston, Texas.
- Rassat, SD, DP Mendoza, DW Matson, and DD Caldwell. 2001. "Microscale Adsorption for Energy and Chemical Systems." In *Laboratory Directed Research and Development Annual Report, Fiscal Year 2000*. PNNL-13501. Pacific Northwest National Laboratory, Richland, Washington, April 2001.
- Rassat, SD, VS Stenkamp, and WE TeGrotenhuis. 2002. "Microwick Gas Absorber." In *Laboratory Directed Research and Development Annual Report, Fiscal Year 2001*, Pacific Northwest National Laboratory, Richland, Washington, April 2002.

- Reddig, M and A MacKnight. 1997. "Investigation of Mars In-Situ Propellant Production." SAE Paper 972496. In 27<sup>th</sup> *International Conference on Environmental Systems*, Lake Tahoe, NV.
- Sanders, GB. 2000. "ISRU: An Overview of NASA's Current Development Activities and Long-Term Goals." 38<sup>th</sup> *Aerospace Sciences Meetings & Exhibit*, AIAA 2000-1062, Reno, NV.
- Sanders, GB, TA Peters, RS Wegeng, WE TeGrotenhuis, SD Rassat, KP Brooks, and V Stenkamp. 2001. "Report on Development of Micro Chemical/Thermal Systems for Mars ISRU-Based Missions." AIAA 2001-0939. *American Institute of Aeronautics and Astronautics*.
- Simon T, R Baird, J Trevathan, and D Clark. 2002. "An Advanced In-Situ Resource Utilization (ISRU) Production Plant Design for Robotic and Human Mars Missions." In *Proceedings of the 53rd Int. Astronautical Congr., The World Space Congress—2002*, IAA-02-IAA.13.3.01, Houston, TX.
- Sridhar, KR, JE Finn, and MH Kliss. 2000. "In-Situ Resource Utilization Technologies for Mars Life Support Systems." *Adv. Space Res.*, **25** (2), pp. 249-255.
- Sridhar, KR, CS Iacomini, and JE Finn. 2004. "Combined H<sub>2</sub>O/CO<sub>2</sub> Solid Oxide Electrolysis for Mars In Situ Resource Utilization." *Journal of Propulsion and Power*, **20** (3), May-June.
- TeGrotenhuis, WE, RS Wegeng, DP Vanderwiel, GA Whyatt, VV Viswanathan, KP Schielke, GB Sanders, and TA Peters. 2000. "Microreactor System Design for NASA In Situ Propellant Production Plant on Mars." Presented at the 4<sup>th</sup> *International Conference in Microreactor Technology*, AIChE Spring National Meeting, Atlanta, March.
- TeGrotenhuis, WE and VS Stenkamp. 2001. "Normal Gravity Testing of a Microchannel Phase Separator for In Situ Resource Utilization." NASA/CR—2001-210955, June 2001.
- TeGrotenhuis, WE, RS Wegeng, GA Whyatt, VS Stenkamp, and A Gauglitz. 2003. *Microsystem Capillary Separations*. U.S. Patent 6,666,909. December, 2003.
- TeGrotenhuis, WE, SD Rassat, and VS Stenkamp. 2005a. *Methods of Contacting Substances and Microsystem Contactors*. U.S. Patent 6,869,462. March 2005.
- TeGrotenhuis, WE and VS Stenkamp. 2005b. *Improved Conditions for Fluid Separations in Microchannels, Capillary-Driven Fluid Separations, and Laminated Devices Capable of Separating Fluids*. U.S. Patent 6,875,247. April 2005.
- TeGrotenhuis, WE and VS Stenkamp. 2005c. Gas-Liquid Processing in Microchannels. In *Microreactor Technology and Process Intensification*, eds. Y. Wang and J.D. Holladay. ACS Symposium Series 914, ACS, Washington, DC.
- Wegeng, RS, SD Rassat, VS Stenkamp, WE TeGrotenhuis, DW Matson, MK Drost, and VV Viswanathan. 2003. *Method and Apparatus for Thermal Swing Adsorption and Thermally-Enhanced Pressure Swing Adsorption*. US Patent No. 6,630,012 B2. Oct. 7, 2003.

Wegeng, RS, SD Rassat, WE TeGrotenhuis, K Drost, and VV Viswanathan. 2004. *Method and Apparatus for Thermal Swing Adsorption and Thermally-Enhanced Pressure Swing Adsorption*. US Patent No. 6,746,515 B2. June 8, 2004.

Zubrin, RM. 1996. *The Case for Mars*. Touchstone Publishers, New York, NY.

Zubrin, R, B Frankie, and T Kito. 1997. "Mars In-Situ Resource Utilization Based on the Reverse Water Gas Shift: Experiments and Mission Applications." AIAA 97-2767, *American Institute of Aeronautics and Astronautics*.

# Distribution

## OFFSITE

Mary Thomas (2)  
NASA Lyndon B Johnson Space Center  
Mail Code BH2, Project Procurement Office  
2101 NASA Parkway  
Houston, TX 77058

## ONSITE

### **Pacific Northwest National Laboratory**

KP Brooks	K6-24
LD Kannberg (3)	K9-09
SD Rassat	K6-28
WE TeGrotenhius	K6-28
Information Release Office (2)	P8-55